COPPE
Instituto Alberto Luiz Coimbra de Pós-Graduação e Pesquisa de Engenharia
UFRJ

DRILL-STRING MODEL FOR COUPLED LATERAL-TORSIONAL VIBRATIONS WITH STOCHASTIC NON-PROPORTIONAL DAMPING

Lucas Passos Volpi

Dissertação de Mestrado apresentada ao Programa de Pós-graduação em Engenharia Mecânica, COPPE, da Universidade Federal do Rio de Janeiro, como parte dos requisitos necessários à obtenção do título de Mestre em Engenharia Mecânica.

Orientador: Thiago Gamboa Ritto

Rio de Janeiro
Julho de 2020

DRILL-STRING MODEL FOR COUPLED LATERAL-TORSIONAL VIBRATIONS WITH STOCHASTIC NON-PROPORTIONAL DAMPING

Lucas Passos Volpi

DISSERTAÇÃO SUBMETIDA AO CORPO DOCENTE DO INSTITUTO ALBERTO LUIZ COIMBRA DE PÓS-GRADUAÇÃO E PESQUISA DE ENGENHARIA DA UNIVERSIDADE FEDERAL DO RIO DE JANEIRO COMO PARTE DOS REQUISITOS NECESSÁRIOS PARA A OBTENÇÃO DO GRAU DE MESTRE EM CIÊNCIAS EM ENGENHARIA MECÂNICA.

Orientador: Prof. Thiago Gamboa Ritto

Aprovada por: Prof. Thiago Gamboa Ritto
Prof. Marcelo Amorim Savi
Prof. Domingos Alves Rade

RIO DE JANEIRO, RJ – BRASIL
JULHO DE 2020

Volpi, Lucas Passos

Drill-string Model for Coupled Lateral-Torsional Vibrations With Stochastic Non-Proportional Damping/Lucas Passos Volpi. – Rio de Janeiro: UFRJ/COPPE, 2020.

XIV, 87 p.: il.; 29, 7cm.

Orientador: Thiago Gamboa Ritto

Dissertação (mestrado) – UFRJ/COPPE/Programa de Engenharia Mecânica, 2020.

Referências Bibliográficas: p. 66 – 73.

1. drill-string. 2. nonlinear vibrations. 3. finite element method. I. Ritto, Thiago Gamboa. II. Universidade Federal do Rio de Janeiro, COPPE, Programa de Engenharia Mecânica. III. Título.

Acknowledgments

I dare say one of the most challenging parts of this dissertation was this part. To grasp the importance of how each person influenced and contributed with what lead me to this point, in few words seems an impossible task.

I would like to thank Diana, for being with me in every moment of this adventure, for being patient with the drill-string conversations and bringing me peace when I didn't know what to do. For the always-present love and care.

I thank my parents, José Roberto and Liliana for giving me support in every challenge that I came across, not only in this stage of life. I would like to thank my sister Luiza, for always landing a hand and, specifically, proofreading – what certainly seemed like out of the context random paragraphs.

I would like to thank Prof. Thiago Ritto for advising me during this period in both my master's and in the project at hand. For giving insights not only on the research itself, but also on how to get ideas from the plane of thoughts and express them in a concrete way.

I would like to thank Prof. Marcelo Savi and Prof. Domingos Rade for accepting to be part of this work and giving insights and always motivating me to achieve more.

I would also like to thank every colleague and friend in the laboratory of Acoustic and Vibrations for the support, specially Daniel, Edison (Fabián), Matheus, Raphael and Rodrigo for the daily conversations and the help with every type of subject: drill-string models, the finite element method, rotordynamics, everlasting coffee, nonlinear dynamics, debugging codes and so on.

I would like to thank all my family and friends who have been with me in all this time, encouraging me in every step. This text carries a bit of each and every one of you, as do I.

Finally, I would like to acknowledge the institutions CAPES, CNPq and Petrobras that made this work possible.

Resumo da Dissertação apresentada à COPPE/UFRJ como parte dos requisitos necessários para a obtenção do grau de Mestre em Ciências (M.Sc.)

MODELO DE COLUNA DE PERFURAÇÃO COM VIBRAÇÕES LATERAL-TORCIONAL ACOPLADAS COM AMORTECIMENTO ESTOCÁSTICO NÃO-PROPORCIONAL

Lucas Passos Volpi

Julho/2020

Orientador: Thiago Gamboa Ritto

Programa: Engenharia Mecânica

Nesta dissertação, a dinâmica de uma de perfuração é analisada. A coluna de perfuração é uma estrutura semelhante a um rotor que perfura formações até atingir o reservatório de petróleo. Esta estrutura é extremamente esbelta e está suscetível à diferentes fenômenos não-lineares. Inicialmente, um modelo é desenvolvido, onde o Método dos Elementos Finitos é utilizado para discretizar uma geometria contínua, levando a um sistema de equações diferenciais. As não-linearidades geométricas obtidas incluem o efeito estático de forças axiais do problema. Este modelo considera uma excentricidade contínua ao longo do seu eixo, não comumente aplicada em uma coluna de perfuração. Em adição, considera-se forças generalizadas no impacto, capazes de causar a torção da coluna. Em sequência, modelos de amortecimento proporcional distintos são apresentados para os graus de liberdade laterais. Nestes, três relações de amortecimento são exploradas. Depois, incertezas globais e não paramétricas são adicionadas aos modelos de amortecimento com a teoria de matrizes aleatórias. Assim, procura-se reconhecer as incertezas inerentes dos modelos, assim como atribuir uma não-proporcionalidade muitas vezes presente em modelos não-lineares com interações fluido-estrutura. Uma técnica de redução de ordem é aplicada e, em sequência, simulações numéricas são realizadas para se obter respostas no domínio do tempo. Com estes resultados, mapas contendo a dinâmica do modelo são criados. Por fim, o Método de Monte Carlo é usado nos modelos estocásticos para se gerar mapas contendo a probabilidade de ocorrência de fenômenos críticos.

Abstract of Dissertation presented to COPPE/UFRJ as a partial fulfillment of the requirements for the degree of Master of Science (M.Sc.)

DRILL-STRING MODEL FOR COUPLED LATERAL-TORSIONAL VIBRATIONS WITH STOCHASTIC NON-PROPORTIONAL DAMPING

Lucas Passos Volpi

July/2020

Advisor: Thiago Gamboa Ritto

Department: Mechanical Engineering

In this dissertation, drill-string dynamics are analyzed. The drill-string consists of a rotor-like structure that drills rock formations until the oil reservoir is reached. The structure in question is extremely slender and prone to different non-linear phenomena. A numerical model is developed, where the Finite Element Method is used to discretize a continuous drill-string geometry, which leads to a system of non-linear differential equations. Geometric nonlinearities includes the static effects of relevant axial forces of the problem. The model considers a continuous unbalance force approach not commonly used in the literature and lateral-torsional generalized impact forces. In the sequence, distinct damping models are presented for the drill-string lateral dynamics. Three damping ratio relations are explored, originating different proportional damping matrices. Later, uncertainties are introduced in the damping matrices with the random matrix theory, which adds global non-parametric uncertainties to the damping term. With this stochastic model, it is – to some extent – acknowledged that the complete nature of the dissipation forces in the process might be unknown and that a nonlinear dynamic with fluid-structure interaction may present non-proportional damping. A model order reduction technique is used, based on the most relevant modes, and numerical simulations are conducted in order to obtain the time-domain response in different drilling configurations. With these, maps detailing possible regimes are presented. The Monte Carlo Method is applied for numerical simulations of the stochastic models. Maps containing probabilities of events are then calculated. Finally, the impact of the proportional damping hypothesis is qualitatively evaluated..

Table of Contents

List of Figures **ix**

List of Tables **xii**

1 Introduction **1**

2 Literature Review **4**

2.1 Drill-string models 4

2.1.1 Drill-string torsional dynamics 4

2.1.2 Drill-string lateral dynamics 6

2.1.3 Coupled models 9

2.2 Damping models 11

3 Drill-string model **15**

3.1 Lateral-torsional dynamics model 15

3.2 Weak form and finite element formulation 21

3.3 Boundary conditions and external forces 24

3.4 Reduced order model 30

4 Damping models **31**

4.1 Deterministic damping models 31

4.2 Stochastic non-proportional damping model 34

5 Results **38**

5.1 Mesh convergence analysis 41

5.2 Complete and simplified models 43

5.3 Deterministic response 45

5.3.1 Phenomena identification 46

5.3.2 Damping models dynamics 48

5.3.3 Dynamic maps 51

5.4 Stochastic response 54

5.4.1 Dispersion analysis 54

5.4.2 Frequency domain analysis 57
5.4.3 Probability maps 61

6 Summary and concluding remarks **64**

Bibliography **66**

A Axial force **74**

B Shape functions **76**

C Damping models **78**
C.0.1 Viscously damped systems 78
C.0.2 Non-viscous damped systems 80

D Modal reduction **83**

E Lumped parameter model **86**

List of Figures

1.1 Drill-string sketch with some components. 2

3.1 Sketch of a beam where (a) is an arbitrary deflection and (b) kinematic behavior in a plane and (c) sketch of a spacial deformation of an arbitrary section. 16

3.2 A schematic of the drill-string where in (a) the geometric center (g.c.) and the distance between the g.c. and the actual gravity center is defined by the vector $\mathbf{e}(\mathbf{x}, t)$ and in (b) an upper view of a section of the drill-string. 20

3.3 A sketch of the drill-string with constant speed at the top Ω, the hook load f_h, the weight $f_w(x)$, the weight on bit W_{ob}, torque on bit T_{bit}, springs modeling stabilizers and pinned regions. 26

3.4 Torque on bit relation from the smooth bit-rock interaction model with a W_{ob} of 220 kN. 27

3.5 Example of the approximation of the function tanh{}. 29

3.6 A sketch of the upper view of a drill-string section where $\boldsymbol{b}$ is the distance between the gravity center and the contact point. $\boldsymbol{f}_z$ and $\boldsymbol{f}_y$ are contact forces in their respective directions. 29

4.1 Dimensionless curves proposed when compared with dimensionless experimental data provided in [16]. 34

5.1 A sketch of the eccentricity profile used. 38

5.2 Natural frequencies obtained through the model with different meshes. In (a) are depicted torsional frequencies for each mode and in (b) lateral frequencies. 42

5.3 43

5.4 Modal Assurance Criterion applied to different meshes. In this case, each mesh was compared with the one with more elements. 43

5.5 Numerical simulations for the complete and simplified models for $\Omega =$ 0.67 Hz (40 rpm) and $W_{ob} = 220$ kN. 44

5.6 Numerical simulations for the complete and simplified models for $\Omega =$ 1.67 Hz (80 rpm) and $W_{ob} = 100$ kN. 44
5.7 Numerical simulations for the complete and simplified models for $\Omega =$ 1.00 Hz (60 rpm) and $W_{ob} = 220$ kN. 45
5.8 Torsional speed at the bit for numerical simulations in different drilling configurations: Case 1 presents $\Omega = 1.33$ Hz (80 rpm) and $W_{ob} = 100$ kN with $\mathcal{S}_{100,1.33} > 0.008$; Case 2 presents $\Omega = 0.67$ Hz (40 rpm) and $W_{ob} = 220$ kN with $\mathcal{S}_{220,0.67} = 1.328$; Case 3 presents $\Omega = 1.75$ Hz (105 rpm) and $W_{ob} = 160$ kN with $\mathcal{S}_{160,1.75} = 0.634$ . . . 47
5.9 Lateral data for numerical simulations in different drilling configurations: Case 1 presents $\Omega = 1.33$ Hz (80 rpm) and $W_{ob} = 100$ kN; Case 2 presents $\Omega = 1.75$ Hz (105 rpm) and $W_{ob} = 160$ kN. In (a) the highest whirl frequency of greater amplitude and in (b) the radial displacement is presented. 47
5.10 Damping ratios inside the frequency threshold established. 48
5.11 Numerical simulations for the different damping models for $\Omega = 1.33$ Hz (80 rpm) and $W_{ob} = 100$ kN. In (a) the is the radial displacement of the geometric center in the middle of the last BHA section and in (b) the rotating speed at the bit. 49
5.12 Numerical simulations for the different damping models models for $\Omega = 0.67$ Hz (40 rpm) and $W_{ob} = 220$ kN. 49
5.13 Numerical simulations for the different damping models for $\Omega = 1$ Hz (60 rpm) and $W_{ob} = 220$ kN. In: (a) the torsional speed at the top; (b) the radial displacement and in (c) the frequency analysis of a backward whirl configuration. 51
5.14 Dynamic maps for the deterministic reduced order model with the first five hundred modes with the first damping model (Rayleigh proportional model). In (a), the torsional severity index and in (b) the whirl frequency. 53
5.15 Dynamic maps for the deterministic reduced order model with the first five hundred modes with the second damping model (adapted Rayleigh proportional model). In (a), the torsional severity index and in (b) the whirl frequency. 53
5.16 Dynamic maps for the deterministic reduced order model with the first five hundred modes with the third damping model (generalized Rayleigh proportional model). In (a), the torsional severity index and in (b) the whirl frequency. 54

5.17 Maximum relative errors in the damping ratio for each used mode for a $W_{ob} = 220$ kN and different dispersion parameters. In (a), the error is calculated using the first damping model; in (b) the second damping model and in (c) the third damping model. 56
5.18 Damping ratio calculated from the main diagonal of the random damping matrices with a $W_{ob} = 220$ kN. In (a), the error is calculated using the first damping model; in (b) the second damping model and in (c) the third damping model. 57
5.19 Frequency domain response for the first stochastic damping model with three different values for dispersion: (a) $\delta = 0.10$, (b) $\delta = 0.30$ and (c) $\delta = 0.50$. 59
5.20 Frequency domain response for the second stochastic damping model with three different values for dispersion: (a) $\delta = 0.10$, (b) $\delta = 0.30$ and (c) $\delta = 0.50$. 60
5.21 Frequency domain response for the second stochastic damping model with three different values for dispersion: (a) $\delta = 0.10$, (b) $\delta = 0.30$ and (c) $\delta = 0.50$. 61
5.22 Probability maps for the stochastic model with the first stochastic damping model (generalized Rayleigh proportional model). In (a), the torsional vibration probability and in (b) the backward whirl probability. 62
5.23 Probability maps for the stochastic model with the second damping model (adapted Rayleigh proportional model). In (a), the torsional severity index and in (b) the whirl frequency. 62
5.24 Probability maps for the stochastic model with the third damping model (generalized Rayleigh proportional model). In (a), the torsional severity index and in (b) the whirl frequency. 63

A.1 Sketch of the drill-string's sections. 74
A.2 Sample axial force distribution with $W_{ob} = 220$ kN. 75

D.1 Numerical simulations for the complete and reduced models for $\Omega = 1.33$ Hz (80 rpm) and $W_{ob} = 100$ kN. In the zoomed region defined from $t = [50, 60]$ s. 83
D.2 Numerical simulations for the complete and reduced models for $\Omega = 0.67$ Hz (40 rpm) and $W_{ob} = 220$ kN. In it, the complete model and with a modal reduction with the first 500 modes. 84
D.3 Numerical simulations for the complete and reduced models for $\Omega = 1$ Hz (60 rpm) and $W_{ob} = 220$ kN. In it, the complete model and with a modal reduction with the first 500 modes. 84

List of Tables

4.1 Table with damping coefficient provided in [16]. 32

5.1 Summary of drill-string properties. 40
5.2 Element distribution. 41

List of Symbols

$\boldsymbol{C}$	Damping matrix
b_1	Rayleigh proportional damping mass coefficient
b_2	Rayleigh proportional damping stiffness coefficient
$\boldsymbol{M}$	Generalized mass matrix
$\boldsymbol{q}$	Generalized coordinates
$\boldsymbol{\mathcal{G}}$	Viscoelastic damping matrix of kernel functions
τ	Kernel delay
σ_{kk}	Normal stresses in the k direction
τ_{kl}	Shear stresses in the kl plane
$\boldsymbol{\mathcal{S}}$	Stress tensor
$\boldsymbol{\sigma}$	Voigt notation stress vector
$\boldsymbol{u}$	Generalized continuous displacement vector
$\mathbb{E}$	Green-St. Venant strain tensor
ϵ_{kk}	Strain in the k direction
γ_{kl}	Shear strain in the kl direction
$\boldsymbol{\epsilon}$	Strain vector in Voigt notation
u_k	Displacement in the k direction
φ_k	Bending angular displacement around the k axis
ϕ	Angular displacement around de x axis
E	Young's Modulus
ν	Poisson's ratio
$\mathbf{I}$	Identity matrix
G	Shear Modulus
$\boldsymbol{\omega}$	Rotation speed vector
U	Potential energy
T	Kinetic energy
ω_k	Rotation speed in around the k axis
e	Eccentricity vector modulus
e_k	Eccentricity vector component in the k direction
A	Cross-section area
$\mathcal{H}$	Hamiltonian
$\delta\{\}$	Variational operator

ρ	Density
I_{xx}	Cross-section inertia
α_0	Unbalance phase angle
$\boldsymbol{N_{u_k}}$	Shape function for the $\boldsymbol{u_k}$ displacement
$\boldsymbol{q}^{(e)}$	Element generalized displacement vector
$\phi^{(e)}$	Vector with elemental rotation around the x axis
Ω	Rotation applied at the top
W_{ob}	Weight on bit
f_h	Hook load
$f_a(x)$	Axial force
a_n	Bit-rock interaction model constant (n =0,1,2 and 3)
$\boldsymbol{f_s}$	Stabilizers elastic force
$\boldsymbol{f}_{bw}$	Impact force with the borehole wall
$\boldsymbol{f}_{rb}$	Friction/rubbing force with the borehole wall
$\boldsymbol{T}_{bw}$	Lateral impact torque
β_n	Second damping model coefficient (n = 1 and 2)
c_n	Third damping model coefficient (n = 1,2,... k)
$\boldsymbol{D}$	Cholesky decomposition of the damping matrix
$\hat{\boldsymbol{G}}$	Random matrix germ
$\hat{\boldsymbol{C}}$	Generic random damping matrix
ω_{n_i}	i^{th} natural frequency
$\boldsymbol{\Phi}$	Matrix with eigenvectors
j	Complex unit ($\sqrt{-1}$)
h	Transfer function

Chapter 1

Introduction

The drilling operation is a key process in gas and oil industry. Long distances in different environments must be drilled in order to reach the oil reservoir for extraction. With the increase in exploration, new technologies are often developed. In a few decades, exploration reached new depths, such as deep well drilling and ultra deep well drilling. In the latter, drill-strings used can present kilometers of length.

On the one hand, there is a key stage in the oil industry. On the other hand, there is a complex, costly and time consuming process. In order to minimize costs and maximize efficiency, the drilling dynamics have been in the highlight of research for the last decades.

One of the main components of the drilling process is the drill-string. It is a slender structure, that can reach up to 9 km. The drill-string is divided in two main components, the drill-pipes and the Bottom Hole Assembly – or BHA. The former is composed of slender pipes and occupies most of the extension of the drill-string. The BHA, however, is considerably stiffer and is where the drill-bit and other equipment is located. At the top, there is a hoisting system and a rotatory table responsible for controlling the force applied at bottom – known as weight on bit – and for rotating the structure, respectively. During the drilling process, drilling fluid – or drilling mud – is used to remove the cuttings. In Fig. 1.1 a sketch of a drill-string can be seen, where the main regions considered in this work are presented.

The structure is susceptible to a set of vibrations, some even unavoidable. While some are harmless, others can lead to efficiency loss and, in extreme cases, can even jeopardize the operation. Those vibrations are commonly associated with the types of motion. Hence, they are usually divided in three distinct cases: axial, torsional and lateral – or transversal – vibrations.

Axial vibrations are a direct consequence of the interaction of the drill-bit and the rock formation. In extreme cases, there is a periodic impact between the bit and the rock formation, known as bit-bounce.

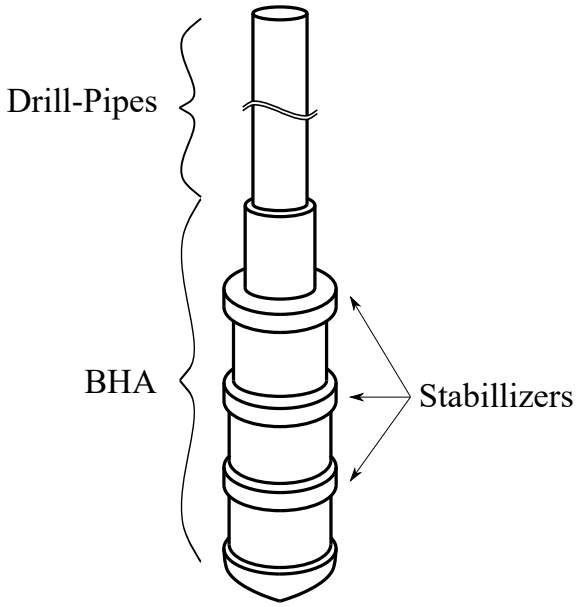

Figure 1.1: Drill-string sketch with some components.

Torsional vibrations are also often associated with the bit-rock interaction. In a critical scenario, it is known as stick-slip. This consists on the stagnation of the bit – the stick phase – followed by the torsion of the drill-string. After a while, the bit is released, causing it to accelerate – the slip phase. After reaching high rotating speeds, the bit decelerates until stagnation, which culminates in a periodic sticking-slipping motion.

Lateral vibrations are a direct consequence of the unbalance of the drill-string. In general, it can be divided in two categories: (i) forward whirl and (ii) backward whirl. The former is unavoidable and is defined by the translation of the drill-string in the same direction of the rotation applied. If this translation presents the same frequency as the rotation, it is called synchronous whirl and, otherwise, asynchronous whirl. The backward whirl, however, is the consequence of the contact between the drill-string and the borehole wall. With this contact, friction forces might induce a rolling motion, which leads to the translation of the drill-string in the opposite direction of the the rotation applied.

Although classified independently, each aforementioned phenomenon is thoroughly interconnected through a set of characteristics, such as axial loads, torsional speed, nonlinearities, impact and so on. Thus, despite the complexity, coupled behavior is often modeled in order to effectively characterize drill-string vibrations.

A set of goals is explored in this work. Formerly, the development of a model that can capture different complex nonlinear phenomena. In sequence, apply in a practical model distinct damping approaches evaluating it's impact in the dynamics. Finally, to add global uncertainties in the damping approaches. With the latter, it is expected to, in part, acknowledge that a linear proportional damping might not fully

reproduce the complexity of the dynamics, which involves fluid-structure interaction and geometric nonlinearities.

This work starts with a literature review of some studies regarding drill-string dynamics and damping. In sequence, the drill-string is modeled with the Finite Element Method, tanking into a account an intrinsic structural unbalance in the BHA and torques due to impact with the borehole wall. In the sequence, three different proportional damping models are presented for the drill-string lateral vibrations. Next, non-proportional stochastic damping models are provided by disturbing each of the proportional damping models. After the models are developed, the results obtained are explored. This section starts with a mesh convergence analysis, followed by a model simplification analysis. With the model successfully simplified, different regime identification procedure are explored and exemplified. With those, the regime of different drilling scenarios is analyzed and identified for each damping model. Finally, the stochastic models are similarly explored, identifying the probability of occurrence of each phenomenon previously identified.

Chapter 2

Literature Review

Throughout the second half of the twentieth century, a variety of modelling techniques was applied in drill-string vibrations. Those range from discrete lumped parameters to continuous models where each may contain different types of interactions with the surrounding environment. While lumped parameters thrives at simplicity — being computationally efficient and useful for the identification of phenomena — continuous models presents a wealth in detail that is often lost in simplified models. At first, studies regarding drill-string vibrations were mostly limited to axial and torsional vibrations. In time, it was observed that a bending motion was present and that some failure cases could not be explained solely by torsional and axial vibrations. Hence, there was a growing interest in the effects of lateral vibrations. As some of the theory of lateral vibrations is inherited from rotordynamics theory, the study of the latter is relevant to modelling lateral vibrations.

In this section, some relevant works in torsional vibrations will be briefly presented and, in sequence, some works in lateral vibrations. Often, one work will present coupling between torsional and lateral vibration and thus, a third section contains coupled models. Finally, some works regarding damping modelling are briefly presented.

2.1 Drill-string models

2.1.1 Drill-string torsional dynamics

Here, some works that are relevant for drill-string torsional dynamics are presented chronologically. Those may range from bit-rock interaction modelling, the stick-slip phenomenon itself and torsional vibration control. This section starts with overall research regarding drill-string torsional dynamics, followed by a brief literature review of bit-rock interaction and stick-slip models.

Halsey et al. [27] performed an analysis regarding drill-string torsional frequencies where an analytical model is compared to experimental data of a vertical drilling rig. It is shown that analytical values are in agreement with experimental data and a few other observations were stated, such as: in a range of lower frequencies, the drill-string behaves as a torsional pendulum and that boundary conditions can be modeled as fixed in the upper end and free at the bottom. In accordance, several works considered models with reduced degrees of freedom. In a similar fashion, Germay et al. [25] used a continuous formulation considering a time-delayed stick-slip approach without damping effects. With this model, the authors concluded that general behavior of the system from both lumped parameter and continuous models are alike, that is, the tendencies related to applied speed and weight on bit are comparable. However, continuous models provided detailed response, with stick-slip occurrence in a different spectrum of frequencies. Another analysis regarding a reduced size system was conducted by Kapitaniak et al. [35], where a lumped parameter model, a continuous model and an experimental model where compared. With both numerical models calibrated, the authors highlighted that even though the lumped parameter model could represent the dynamics, the continuous model presented higher accuracy. These studies gives relevant insights on the applicability of lumped parameter strategies in contrast with an finite element method approach, as well as in model order reduction techniques.

Another relevant aspect, is the presence of uncertainties in the process. Ritto and Sampaio [65] considered uncertainties in the top speed applied. With it, the authors proposed efficiency coefficients to evaluate the effectiveness of the input power when considering both the rock cutting and the advance of the drill-string. Finally, it is observed that drill-string length, top speed and friction can directly affect the efficiency and that uncertainties in top speed may lead to different dynamics in some configurations. Uncertainties present in the problem are often associated with unpredictable components, such as rock formation.

Naturally, the bit-rock interaction models represent a primordial aspect in torsional vibrations as the stick-slip phenomenon is directly connected with this nonlinear interaction. In 1985 Karnopp [36] introduced a model for general stick-slip friction. In it, the authors considered a discontinuous generalized force that can be divided in two stages, one during the stick and the other during the slip. They defined a small range of velocities where the stick forces would actuate and, outside this gap, slip forces would be present. According to the authors, this approach allowed a simple and computationally efficient analysis of the stick-slip motion. This model, although initially applied to general types of dynamical systems, was later on explored in the analysis of drill-string vibrations.

In 1991, Lin and Wang [44] developed a continuous model for the dry-friction of

the stick-slip, according to an exponential law. Through simulations, the authors analyzed the impact of parameters in the overall dynamics and, at last, summed up the effects of drill-string length, rotating speed and damping effects on torsional vibrations. Another continuous model was provided by Tucker and Wang [75]. It considers the weakening of the torque on bit with the increase in speed. With this model, the authors conduct several operational procedures to minimize severe torsional vibrations. In contrast, Detournay and Defourny [19] developed a discontinuous bit-rock interaction model based on the cutting forces and on the depth-of-cut, where the model was successfully tested with experimental data. In 2004, Richard et al. [58] gave continuation to the work developed in Detournay and Defourny [19], adding an axial coupling term and a time-delay relation, where the bit-rock interaction would depend on past instants. While both approaches are broadly used, the presence of discontinuities adds to the complexity of the system. Hence, a continuous bit-rock interaction model that can successfully predict the nonlinear phenomenon is often used.

As the bit-rock presents highly complex interaction and, added to the unpredictable nature of the rock formation, this interaction is considered a source of uncertainties. Ritto et al. [60] modeled the drill-string with torsional-axial dynamics in order to optimize the rate of penetration during the drilling process. One of the key aspects in this work was the inclusion of uncertainties related to the bit-rock interaction. Nogueira [56] proposed a stochastic model for torsional vibrations, where friction at the bottom and damping ratio were considered as random variables. Ritto [62] applied a Bayesian approach to identify the parameters for the bit-rock interface, where an additive white noise was considered, as in a measuring equipment. In 2017, Lobo et al. [47] studied transition of rock surfaces through different transition function. Afterwards, a stochastic model was developed, which took in account different times and magnitudes in each transition.

Based on experimental data, Ritto et al. [63] proposed a three-stage bit-rock interaction model. The first two stages are linearly dependent in the rotational speed at the bit and the last a cubic polynomial. With it, a stability analysis was conducted, where it was noticed that higher weight on bits and lower applied rotations would lead to an increase in severity. This interaction model successfully characterize overall stick-slip occurrence, where it increases in higher weight on bits and decreases when high rotations are applied.

2.1.2 Drill-string lateral dynamics

Initially, drill-string failure was assumed to be associated mainly with torsional and axial vibrations. However, as stated by Allen [4] in 1987, vibrations in the BHA

could not be solely described through the study of axial and torsional vibrations. As those models became unable to explain BHA failure, lateral vibrations models joined the spotlight of drill-string studies. These dynamics are often modeled as a slender rotor-like structure and hence, most of these models intersect with rotor models. In here, some relevant works in rotordynamics are presented as they are often fundamental in the comprehension of drill-string lateral dynamics.

A relevant study in the area started in 1972, with the finite element method in rotordynamics. Ruhl and Booker [68] considered the dynamic limited to a plane and hence, no gyroscopic effects were analyzed. In this paper, synchronous whirl was successfully observed and it was concluded that finite element method can be considered practical and accurate for rotor vibration purposes. In a continuation to this study, Nelson and McVaugh [54] applied the finite element method to an eccentric rotor. Not only it considered movement in the space, it added inertia and gyroscopic moments disregarding any torsion effect. A few years later, in 1980, Nelson [53] continued the previous analysis accounting shear components by introducing the Timoshenko Beam theory to the former model. Later in that year, Zorzi and Nelson [89] generalized the model in order to compute axial torques and torsion buckling. This last methodology is convenient to model continuous rotor-like structures under axial torques, such as the drill-string. Even though these analyses were mainly linear, similar modelling approaches were extrapolated to drill-strings [37–39, 66, 67]. In 1987, Burgess et al. [10] a finite element model was developed to predict BHA failure, as the author observed that BHA failure might be related to the impact between the BHA and the borehole wall. Through nonlinear static modal analyses, assisted by field data, the authors concluded that, for shallow wells, lateral models can achieve fast and reliable results in predicting failure. In a similar fashion, in 1992, Spanos and Payne [72] applied the finite element method to discretize the lateral geometry of the BHA. Experimental data was used to aid in the damping model and, in sequence, several sensibility analyses were conducted regarding damping, added fluid mass, weight on bit and stabilizer boundary conditions. This presented a versatile methodology in for modelling drill-string dynamics.

In contrast to models achieved with the finite element method, several works with a lumped parameter approach have been used. Stroud and Lines [74] conducted numerical and experimental simulations in identification of backward whirl in horizontal drill-strings. In this Jeffcot-like rotor model, the authors were able to successfully qualitatively reproduce the experimental data. Kapitaniak et al. [34] conducted a study in the identification of forward and backward whirls in lateral vibrations. The lumped parameter model proposed was calibrated with experimental data. In sequence, different configurations of mass and angular speed were analyzed in a set of initial conditions and, finally, probabilities of occurrence of each

phenomenon was conducted, highlighting that different whirls may coexist. A year later, Kapitaniak et al. [33] stated that not only both forward and backward whirl were found to coexist but also chaotic-like behavior was observed experimentally for the first time. In addition, reduced order models were compared with continuous models. In one particular case, Neubauer et al. [55] used the shooting method to calibrate the initial conditions of a lumped parameter in order to optimize the system's integration, where a finite element model was used as comparison criteria. With this, a lumped parameter model could be used to obtain an equivalent analysis. In this case, however, permanent contact was considered in an inclined borehole wall. While this may be feasible in an inclined borehole, vertical drilling will often present a discontinuous impact, which increases the complexity of the calibration process.

As conducted by Jansen [31], Christoforou and Yigit [14] proposed a lumped parameter model for lateral vibrations where the nonlinear nature of the problem was analyzed. The authors used the virtual work method to achieve the equations of motion with inclusion of a Hertizian's contact during impact, friction during contact and gyroscopic moments. Later on, both backward whirl and impact regimen were observed. In the former case, the authors concluded that the dynamic presented an attractor. This represented a development in the nonlinear nature of drill-string lateral vibrations.

Aside from modelling the drill-string, the fluid-structure coupling became a key point in lateral dynamics. In 1970, Fritz [23] modeled and studied the effect of annular fluids in long rotor-like machinery. In this work, it was assumed an encased vibrating rotor surrounded by an incompressible fluid, observing that the hydrodynamic mass can reduce the rotor critical speed. Later on, the fluid interaction model developed in this paper was used in several drill-string models [5, 38, 41, 46]. Similar effects were observed in 1991 by Jansen [31], where an added fluid mass and fluid drag where considered in a drill-string model for lateral vibrations. In this case, lateral dynamics were modeled as a Jeffcot rotor, where several analysis were conducted. In this work, the damping of the dynamics was restricted to the fluid interaction, where a nonlinear damping model was considered. In 2009, Ritto et al. [66] modeled a linear coupling between fluid and structure in drill-string dynamics. The system of equations was then discretized with the finite element method followed by modal and dynamics analyses, where it was stated that the fluid flow inside the drill-string may cause instabilities. It also led to higher lateral vibrations in upper sections of the drill-string, while the effects on torsional and axial vibrations are not as accentuated.

2.1.3 Coupled models

While there is expressive research related to uncoupled drill-string vibrations, the study of coupled dynamics is often a relevant as the complexity of the system might lead to non-trivial configurations. Thus, in this section, some models for coupled dynamics are explored. Even though drill-string axial vibrations are not explored in this work, some works shown here may present either lateral-axial, torsional-axial or fully-coupled models.

In 1960, Finnie and Bailey [22] conducted experimental research regarding both axial and torsional vibrations. In this pioneer work, the authors highlighted that a relevant, however unexplained, interaction between axial and torsional dynamics was registered. A year later, Bogdanoff and Goldberg [9] assumed that the drill-strings were susceptible to uncertainties in both axial and torsional directions. For that, it was assumed constant generalized forces with random fluctuations which are correlated for both torsional and axial vibrations. It is interesting to notice that random torques were modeled in order to consider torques due to the contact of the drill-string with the borehole wall in the whole extension. In other words, the effects of lateral vibrations in the torsional direction were considered as random variables. A few years later, in 1968, Deily et al. [17] presented a study of downhole measurement data concerning axial loads, torques, bending moments, axial, angular and radial accelerations, and pressure inside and outside the drill-string. Although the analysis focused on the effects of axial vibrations, the authors highlighted bending — or lateral — vibrations with the same direction and frequency of the rotation of the drill-string, a phenomenon formerly identified as forward whirl in rotordynamics. At this point, it was acknowledged that the drill-string failure was connected not only to axial and torsional dynamics, but also to lateral dynamics. Later on 1989, Shyu [70] presented a thesis with detailed information regarding lateral and axial vibrations. In it, the dynamics were modeled through a lumped parameter approach and the effects of axial loads and torques were analyzed. In the same work, lateral and axial dynamics were linearly coupled and a set of cases was studied regarding lateral dynamics. Finally, it was concluded that forward whirl can be a source of abrasive damage to the BHA, while backward whirl causes high speeds and high bending cycles. This explained in details how lateral vibrations could be associated with drill-string failure.

In 1998, Yigit [86] coupled both lateral and torsional dynamics. The coupling used in this model regarded how each dynamic affected one another. In other words, lateral vibrations would impact torsional and torsional vibrations would impact lateral. Regarding lateral vibrations, this coupling was done through the assumption that the BHA was rigid to torsion and hence, the rotation at the bit would be

the same as in the BHA. Another effect would be that the lateral stiffness would be susceptible to torsion. In sequence, the torques generated by lateral interaction would affect directly in the torque. Finally, the authors modeled the impact by the conservation of momentum. This is, when a threshold was surpassed, the integration process would be interrupted and new initial conditions would be recalculated restarting the whole process. At the end, it was concluded that the coupling between dynamics affects expressively the system's behavior. In 2000, Yigit [87] stated that this complex coupled dynamics might lead to unwanted consequences in lateral vibrations when controlling torsional vibrations. In accordance, Christoforou and Yigit [15] highlighted that the interdependence between dynamics adds to the complexity of successfully controlling a drill-string with torsional and lateral vibrations. Also exploring this type of coupling, Volpi et al. [80], interpreted the models response with different degrees of coupling. It was observed that the dynamics were not only connected, but that lateral dynamics could disrupt severe torsional vibrations. In addition, small changes in torsional dynamics could lead to severe changes in lateral phenomena.

In 2002, Leine and Van Campen [41] conducted an analytical study of the interaction between torsional and lateral vibrations were explored. Through a simple lumped parameter model, the authors analyzed different equilibrium and periodic configurations for both lateral and torsional vibrations. In sequence, a combination of both was explored. With these models, different type of regimen were observed: from regions of stick-slip to regions of backward whirl.

In 2003, [48] proposed a lateral-torsional lumped parameter model where the bending angle was taken into account, and then it was compared to experimental data. Numerical simulations provided a qualitative chaotic-like behavior, with impact dynamics sensible to initial conditions. When comparing with the experimental data, the authors concluded that the model suffices in describing local BHA behavior.

In 2005, Khulief and Al-Naser [37] discretized a fully coupled continuous model with the finite element method. Considering nonlinearities due to coupling and the stiffening effect of axial loads, the authors conducted modal and dynamics study with full and reduced order models with intention to provide further tools in drill-string analysis. Two years later, Khulief et al. [39] used the finite element method to discretize the drill-string and gave sequence to previous works. Although the model account's for a coupled dynamics, the study focused in stick-slip oscillations. The authors proposition was to include a reliable model to understand the complex dynamics, acknowledging that further development was necessary to account lateral and axial dynamics.

In 2009, Ritto et al. [67] developed a fully-coupled non-linear model approxi-

mated by the finite element method. In it, impact, fluid and bit-rock interactions were taken in account. In sequence, the authors modeled the effects of uncertainties in the bit-rock interaction, with the application of the non-parametric probabilistic approach Soize [71]. Finally, it is stated that the nonlinear model presents sensibility to uncertainties and both torsional and axial responses are highly dependent on said uncertainties. The importance of uncertainties was previously observed in different instances. For example, in 2003, Christoforou and Yigit [15] considered that a next step in successfully controlling a drill-string would be considering the presence of uncertainties.

Another source relevant dissipative term is borehole wall friction. Liao et al. [42] developed a multiple degree of freedom lumped parameter model with coupled lateral-torsional dynamics. In it, the authors conducted a sensibility analysis in the friction coefficient, where, depending on the coefficient, the system may operate in a safe configuration. Later, in 2020, In Volpi et al. [81], lateral-torsional vibrations were explored with uncertainties in the borehole wall friction parameter. In this analysis, a lumped parameter model was used in different drilling configurations. For each, the regimen was identified and classified. In sequence, a stochastic model with random friction was used to obtain the probability of occurrence of each phenomenon. As seen before, the system's regime is highly dependent on the friction coefficient, as small friction coefficients led to a sliding motion and, in extreme cases, even impact.

The unbalance is also a major source of lateral vibrations and its configurations can affect the response. In 2017, Vijayan et al. [79] examined the borehole interaction in a lateral-axial coupled model. In this study, stabilizers were treated as eccentric masses, instead of bearings – which is often adopted. The analysis was conducted observing the frequency domain, where a series of frequency jumps associated with the backward whirl were observed, which are directly connected with the intensity of the eccentricity and phase angle between possible unbalances. This conclusion is in accordance with the work from 1992, from Spanos and Payne [72], where the author registered that the nature of unbalance could greatly influence the model's response.

2.2 Damping models

In a system as complex as the drill-string, the presence of damping should not be overlooked. It can be originated by an intrinsic structural damping or by a fluid interaction. However, few information concerning the constitutive nature of the damping is provided. Hence, in this section a set of damping strategies and properties are mentioned.

Considering a viscously damped system, a general equation of motion can be expressed by:

$$\boldsymbol{M}\ddot{\boldsymbol{q}} + \boldsymbol{C}\dot{\boldsymbol{q}} + \boldsymbol{K}\boldsymbol{q} = \boldsymbol{f}, \tag{2.1}$$

where matrix $\boldsymbol{M}$, $\boldsymbol{C}$ and $\boldsymbol{K}$ are the mass, damping and stiffness matrices, respectively. When modelling viscous damping, a proportional damping approach is common. Given that the nature of the damping might not be straight forward, a proportional damping provides a practical solution for many systems. Maybe the most used is the 'Rayleigh damping':

$$\boldsymbol{C} = b_1\boldsymbol{M} + b_2\boldsymbol{K}, \tag{2.2}$$

where, in this case, $\boldsymbol{C} \in \mathbb{R}_{m\times m}$, $\boldsymbol{M} \in \mathbb{R}_{m\times m}$ and $\boldsymbol{K} \in \mathbb{R}_{m\times m}$. $b_1 \in \mathbb{R}^+$ and $b_2 \in \mathbb{R}^+$ are model constants. This model expresses the overall damping as a linear combination of both mass and stiffness matrices, preserving the classical normal modes of the undamped system. In 1964, [43] provided a set of necessary and sufficient conditions needed in order to obtain damped linear systems with those classical normal modes. In it, the authors concluded that it is necessary to have configuration where $(\boldsymbol{M})^{-1}\boldsymbol{C}$ and $(\boldsymbol{M})^{-1}\boldsymbol{K}$ must commute in order to obtain said configuration. A generalization of the proportional damping was developed in [12], where it could be modeled by a polynomial relation of the mass and stiffness matrix:

$$\boldsymbol{C} = \boldsymbol{M}^{-\mathbf{1}}\sum_{j=0}^{N-1} a_j(\boldsymbol{M}^{-\mathbf{1}}\boldsymbol{K})^j, \tag{2.3}$$

In [1], extensive work regarding different types of proportional damping is detailed. At first, the author focus on the modelling of viscous damping. In the sequence a generalization of the previous conditions for existence of classical modes are developed. With this method, there is great flexibility in modelling a proportional damping when the damping ratios are known, i.e.: $\xi = \xi(\omega_n)$, where ξ is the damping ratio and ω_n a natural frequency. Briefly, it is stated that:

$$\boldsymbol{C} = \boldsymbol{M}^{-1}f_1(\boldsymbol{M}^{-1}\boldsymbol{K}, \boldsymbol{K}^{-1}\boldsymbol{M}) + \boldsymbol{K}^{-1}f_2(\boldsymbol{M}^{-1}\boldsymbol{K}, \boldsymbol{K}^{-1}\boldsymbol{M}), \tag{2.4}$$

where f_1 and f_2 are arbitrary functions. For the proportional damping, f_1 and f_2 are both constants. This method, while not as straight forward as the Rayleigh damping, it extremely flexible, being able to model different curves as long as the relation between damping ratio and natural frequencies are known. The author highlights that a generalized function can be written in the form of Taylor Series. Hence, this method is a convenient form of the generalized proportional damping shown in Eq. 2.3. Further examples are provided in Appendix C.

In this same work, non-viscous damping is also explored. This type of damping depends on the past history of the dynamics. Hence, the system of equations can be expressed as:

$$\boldsymbol{M}\ddot{\boldsymbol{q}} + \int_{-\infty}^{\infty} \boldsymbol{\mathcal{G}}(t-\tau)\dot{\boldsymbol{q}}(\tau)d\Delta\tau + \boldsymbol{K}\boldsymbol{q} = \boldsymbol{f}. \tag{2.5}$$

In the previous equations, the damping can be seen as Kernel functions. It is shown that, when said restrictions are met, it can be diagonalized.

However, damping in structures are seldom proportional. The assumption of proportionality is a consequence of a damping matrix that is diagonally dominant in the modal coordinates. Several modelling strategies were developed throughout the years in order to identify and quantify non-proportional damping.

In 1989, Ibrahimbegovic and Wilson [30] provided an algorithm for non-proportional damping. In it, off diagonal terms in modal base are considered as external forces. In sequence, the authors provided an integration method for this type of problem. In 1990, Bellos and Inman [6] developed an approximated methodology for frequency domain analysis for non-proportionally damped system. The main hypothesis is that off-diagonal terms can be estimated through known transfer functions of a proportionally damped reference. In 2012 Canor et al. [11] explored an uncoupling technique for stochastic process. It considers off-diagonal terms in small order and decouples a non-proportional damping assuming an asymptotic expansion of the modal transfer function. Later on, the authors apply the technique to large scale systems related to the civil engineering context. These approaches try to decouple the system of equation, which, in general, facilitates the analysis.

However, estimating both the complex modes and the non-proportional damping is highly complex procedure. In 1991, Minas and Inman [49] developed a methodology for estimating non-proportional damping from complex modal information. This is based on the estimation of unknown complex mode shapes from known ones, using the least squares method. In 2004, Adhikari [2] proposed an optimal complex mode and, in addition, an index for measuring non-proportionality. One of the purposes was to evaluate the impact of off diagonal terms in the damping matrix.

Also to understand the effects of non-proportional damping, in 2009 Denoël and Degée [18] explored the effects of slightly coupled modes. This coupling is a consequence of the non-proportionality and, in this work, was considered a coupling of small degree – which does not violate the hypothesis of diagonally dominant damping.

It has been noted that the relevance of damping in drill-string modelling is a key aspect in the dynamics. Wiercigroch [83] acknowledged the damping as a critical stabilizing term in torsional dynamics. The effects of damping in drill-string is also analyzed with a semi-analytical approach by Besselink et al. [8], where the inclusion

of axial dissipation in the BHA. In Jansen [31] acknowledged the damping in lateral dynamics to be restricted to the fluid drag. This approach leads to a nonlinear damping coefficient dependent on the cross-section total speed – which intrinsically couples lateral degrees of freedom. Damping due to fluid interaction is also explored by Ritto et al. [66], where an additional damping matrix is observed when a linear variation in pressure is considered in the present fluid. Khulief and Al-Sulaiman [38] considered the drilling fluid for lateral displacements, which led to another transversely coupled damping matrix. Ambrus et al. [5], for instance, assumed a similar fluid interaction model in a lumped parameter model, with the addition to a coupling term between torsional dynamics. While these approaches often leads to additional mass and stiffness matrices, the resulting damping is not necessarily proportional.

Chapter 3

Drill-string model

The modeling of drill-string dynamics is in constant development. Simple models range from lumped parameters to continuous models. Whereas this work explores a continuous formulation, several research that preceded this study focused in a lumped parameter approach. Those preliminary research were relevant to understand the drill-string's overall behavior. In [80], the effects of coupled dynamics were observed, in [81], the importance of the borehole-BHA interaction was made clear by a stochastic model. Other stochastic models were proposed and analyzed, where the effectiveness of regime identification tools were tested. In Appendix E, more details regarding the lumped parameter model and those prior works are presented. In this section, both the deterministic and stochastic models are developed for the analysis. In order to analyze this set of complex nonlinear dynamics, the finite element method (FEM) is used to discretize a continuous drill-string geometry. At first, a brief review of continuum mechanics is conducted and, in the sequence, the equations of motion are developed, starting with the kinematics of the problem, constitutive relations and energy equations. Finally, the Finite Element Method is applied to the weak-form equation obtained, which leads to a system of nonlinear differential equations.

3.1 Lateral-torsional dynamics model

In this section, the tools provided previously are applied to the specific case of lateral-torsional dynamics in the drill-string. This section is divided in two parts: in the first part, the system's kinematics, constitutive relations and energy equations are explored. In the second part, the extended Hamilton principle is applied to the equations developed and the system is discretized through the finite element method.

Kinematics

This work considers that, due to the length of drill-string, shear effects are negligible and that deformations are of small proportion. Hence, the kinematics for the drill-string can be modeled through the Rayleigh beam theory. Figure 3.1 presents a sketch of a beam under deflection in a plane and in space. From the cross-section behavior, it is possible to identify kinematic restriction for the cross-section deformation.

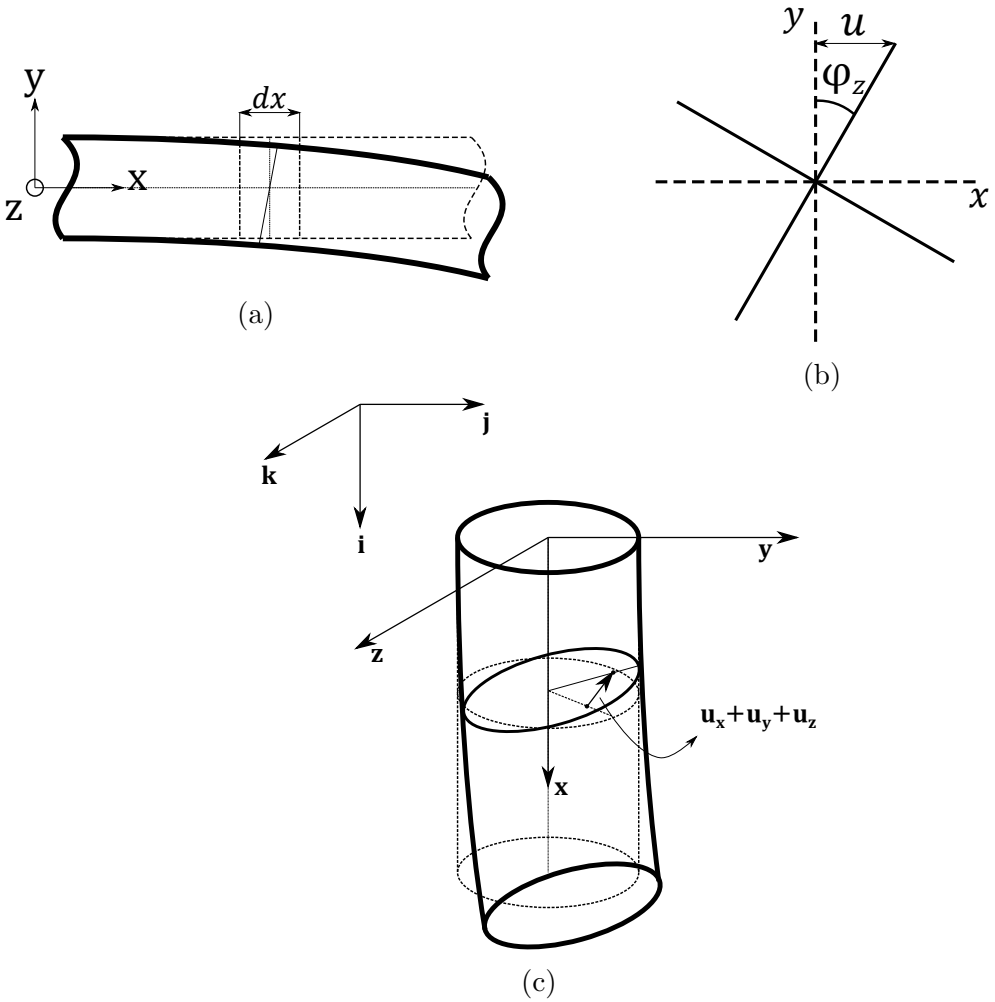

Figure 3.1: Sketch of a beam where (a) is an arbitrary deflection and (b) kinematic behavior in a plane and (c) sketch of a spacial deformation of an arbitrary section.

For small rotations, the angles are assumed to be:

$$\varphi_y = -\frac{\partial u_z}{\partial x} \quad \text{and} \quad \varphi_z = -\frac{\partial u_y}{\partial x}, \tag{3.1}$$

where φ_y and φ_z are the angle of rotation around their respective axis in the deformed configuration. As seen in Fig. **??** the total displacement along the cross-section can be represented as[**?**]:

$$u_x = z\varphi_y - y\varphi_z, \tag{3.2}$$

$$u_y = v + y(\cos\phi - 1) - z\sin\phi$$
$$u_z = w + z(\cos\phi - 1) + y\sin\phi, \tag{3.3}$$

where u_x is the cross-section displacement. v and w are deformations in the direction of y and z axis, respectively. u_x, u_y and u_z are the total displacements in each direction and ϕ the torsion angle. These relation can be achieved by rotating the overall deformations to a main frame of reference [61]. As this model does not account for axial dynamics, the deformation in the origin of the cross-section is zero ($u_x(x, y = 0, z = 0, t) = 0$). From this section onward, in order to simplify the notation the partial derivative is presented as: $\frac{\partial\{\}}{\partial x} = \{\}'$.

Constitutive relations

When an isotropic behavior is considered, the material's constitutive equation can be expressed by the generalized Hooke's law [61]:

$$\boldsymbol{\mathcal{S}} = \frac{E}{2(1+\nu)}\mathbb{E} + \frac{\nu E}{(1+\nu)(1-2\nu)}\mathrm{tr}(\mathbb{E})\mathbb{I}, \tag{3.4}$$

where E is the Young's modulus and ν the Poisson's ratio. In Voigt's notation, the constitutive relation becomes:

$$\begin{Bmatrix} \sigma_{xx} \\ \sigma_{yy} \\ \sigma_{zz} \\ \tau_{xy} \\ \tau_{xz} \\ \tau_{yz} \end{Bmatrix} = \frac{E(1-\nu)}{(1+\nu)(1-2\nu)} \begin{bmatrix} 1 & \frac{\nu}{1-\nu} & \frac{\nu}{1-\nu} & 0 & 0 & 0 \\ \frac{\nu}{1-\nu} & 1 & \frac{\nu}{1-\nu} & 0 & 0 & 0 \\ \frac{\nu}{1-\nu} & \frac{\nu}{1-\nu} & 1 & 0 & 0 & 0 \\ 0 & 0 & 0 & \frac{1-2\nu}{2(1-\nu)} & 0 & 0 \\ 0 & 0 & 0 & 0 & \frac{1-2\nu}{2(1-\nu)} & 0 \\ 0 & 0 & 0 & 0 & 0 & \frac{1-2\nu}{2(1-\nu)} \end{bmatrix} \begin{Bmatrix} \epsilon_{xx} \\ \epsilon_{yy} \\ \epsilon_{zz} \\ \gamma_{xy} \\ \gamma_{xz} \\ \gamma_{yz} \end{Bmatrix}. \tag{3.5}$$

Assuming $\sigma_{yy} = \sigma_{zz} = \tau_{yz} = 0$, the constitutive relation is greatly reduced to:

$$\begin{Bmatrix} \sigma_{xx} \\ \tau_{xy} \\ \tau_{xz} \end{Bmatrix} = \begin{bmatrix} E & 0 & 0 \\ 0 & G & 0 \\ 0 & 0 & G \end{bmatrix} \begin{Bmatrix} \epsilon_{xx} \\ \gamma_{xy} \\ \gamma_{xz} \end{Bmatrix}. \tag{3.6}$$

Energy equations

The vibrations of the drill-string are closely related to what is expected from rotor-like structure. In this case, potential energy is mainly a consequence of the strain, while kinetic energy is divided in it's translational and rotational components:

$$U = \frac{1}{2}\int_{\forall} \boldsymbol{\epsilon}^T \boldsymbol{\sigma}\, d\forall, \tag{3.7}$$

$$T = \frac{1}{2}\int_L (\rho A \boldsymbol{v}^T \boldsymbol{v} + \boldsymbol{\omega}^T \mathbf{I} \boldsymbol{\omega}) dx, \tag{3.8}$$

where $\forall$ is the volume, ρ the volumetric density, $\boldsymbol{\omega} = \begin{Bmatrix} \omega_x & \omega_y & \omega_z \end{Bmatrix}$ the rotation speed in each respective direction in the inertial frame of reference, $\boldsymbol{v}$ the speed of the gravity center, A the cross-section's area and $\boldsymbol{I}$ is the inertia matrix. In general, the work in the system is expressed by:

$$W = \int \boldsymbol{f} \cdot d\boldsymbol{x}, \tag{3.9}$$

where $\boldsymbol{f}$ is the vector containing acting forces. Those are treated as external forces and are presented further on.

The potential energy is estimated based on the kinematic assumptions. By the definition provided in Eq. 3.7 and the constitutive relations previously mentioned in Eq. 3.6, it is rewritten as:

$$U = \frac{1}{2}\int_{\forall} (E\epsilon_{xx}^2 + 4G(\gamma_{xy}^2 + \gamma_{xz}^2)) d\forall. \tag{3.10}$$

Where, according to Eqs. 3.2 and 3.3:

$$\begin{aligned} \epsilon_{xx}^2 = (z^2 w''^2 - 2zyv''w'' + y^2 v''^2) + \\ u_x'(z^2 w''^2 - 2zyv''w'' + y^2 v''^2) + \\ u_x'\phi'^2(y^2 + z^2) + u_x'(v'^2 + w'^2) + \\ 2u_x'\phi'(w'(y\cos(\phi) - z\sin(\phi)) - v'(z\cos(\phi) + y\sin(\phi))), \end{aligned} \tag{3.11}$$

where terms in the order of $\frac{\partial\{\}}{\partial x}^4$ were considered small (e.g.: $\frac{\partial x}{\partial x}^4 \approx 0$). In sequence, as E is constant through the area and due to the tubular cross section:

$$\int_A y^2 dA = \int_A z^2 dA = I_{xx}$$

$$\int_A yz dA = \int_A z^3 dA = \int_A y^3 dA = \int_A yz^2 dA = \int_A y^2 z dA = 0 \tag{3.12}$$

and

$$\int_A u_x' dA = \frac{f_a(x)}{E}, \tag{3.13}$$

where $f_a(x)$ is the axial force in an arbitrary section [39], shown in Appendix A. The relations presented in Eq.3.11, when integrated in the area, can be presented as:

$$\int_A \epsilon_{xx}^2 dA = I_{xx}(v''^2 + w''^2) + f_a(x)(v'^2 + w'^2) +$$

$$+2I_{xx}\phi'(v''w' - w''v')\cos(\phi)$$
$$-2I_{xx}\phi'(v''v' + w''w')\sin(\phi). \tag{3.14}$$

The same procedure is applied to $\gamma_{xy}^2 + \gamma_{xz}^2$:

$$4\int_A(\gamma_{xy}^2 + \gamma_{xz}^2)dA = I_p\phi'^2 + 2I_{xx}\phi'(\varphi_z\varphi_y' - \varphi_y\varphi_z'), \tag{3.15}$$

where, once more, terms of the order of $\frac{\partial\{\}}{\partial x}^4$ were considered irrelevant.

Finally, relations presented in Eqs. 3.14 and 3.15 are applied to the potential energy equation (Eq. 3.10) and divided in two parts:

$$U = U_L + U_{NL}, \tag{3.16}$$

where:

$$U_L = \frac{1}{2}\int_L(I_{xx}E(v''^2 + w''^2) + f_a(x)(v'^2 + w'^2) + GI_p\phi'^2)dx \tag{3.17}$$

and

$$U_{NL} = \int_L I_{xx}\phi'(E(v''w' - w''v')\cos(\phi) - E(v''v' + w''w')\sin(\phi))dx.$$

In order to calculate the kinetic energy, it is necessary to rewrite the system of equations in the inertial frame of reference. To accomplish it, both translation and rotation speeds are modeled. In Fig. 3.2, a schematic of a section of the drill-string is presented, where the geometric center is defined (g.c.) and the distance between the gravity center and geometric center is defined by $\mathbf{e}(\mathbf{x}, t)$. The overall distance between the frame of reference and gravity center can be expressed as:

$$\mathbf{d}(x, 0, 0, t) = \begin{Bmatrix} 0 \\ v(x,t) \\ w(x,t) \end{Bmatrix} + \begin{Bmatrix} 0 \\ e_y(x,t) \\ e_z(x,t) \end{Bmatrix}, \tag{3.18}$$

where $e_y = e\sin(\phi + \alpha_0)$ and $e_z = e\cos(\phi + \alpha_0)$ are the distances of the gravity center from the geometric center where $e = |\mathbf{e}|$, and α_0 is the angle in an initial moment.

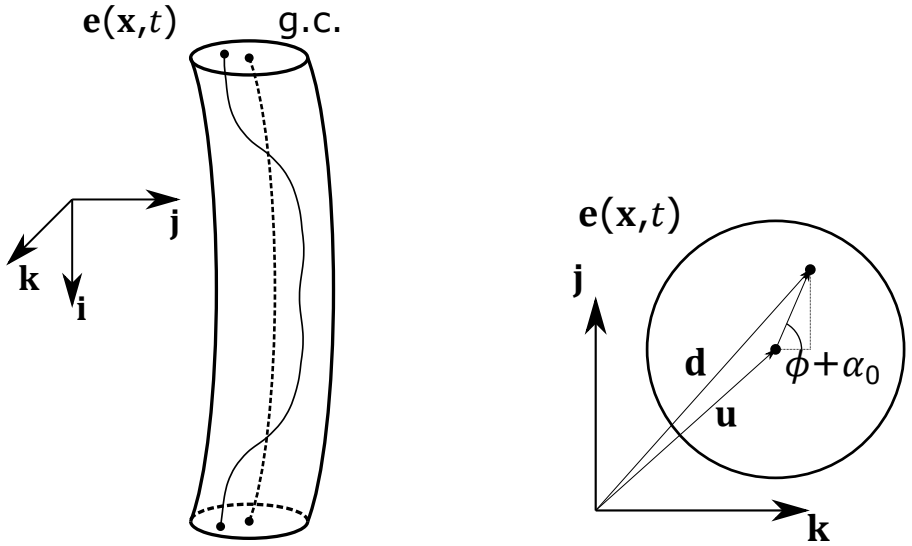

(a) (b)

Figure 3.2: A schematic of the drill-string where in (a) the geometric center (g.c.) and the distance between the g.c. and the actual gravity center is defined by the vector $\mathbf{e}(\mathbf{x}, t)$ and in (b) an upper view of a section of the drill-string.

The translation speed can be calculated by:

$$\mathbf{v} = \dot{\mathbf{d}} = \begin{Bmatrix} 0 \\ \dot{v} + e\dot{\phi}\cos(\phi + \alpha_0) \\ \dot{w} - e\dot{\phi}\sin(\phi + \alpha_0) \end{Bmatrix} \tag{3.19}$$

As previously, the rotations must be set to a frame of reference. The rotation around the $\boldsymbol{x}$ axis the $\boldsymbol{y}$ axis are defined by the transformations:

$$\boldsymbol{\Theta}_x = \begin{bmatrix} 1 & 0 & 0 \\ 0 & \cos(\varphi_x) & -\sin(\varphi_x) \\ 0 & \sin(\varphi_x) & \cos(\varphi_x) \end{bmatrix}, \quad \boldsymbol{\Theta}_y = \begin{bmatrix} \cos(\varphi_y) & 0 & \sin(\varphi_y) \\ 0 & 1 & 0 \\ -\sin(\varphi_y) & 0 & \cos(\varphi_y) \end{bmatrix}, \tag{3.20}$$

respectively, where φ_x is the rotation angle around the $\boldsymbol{x}$ axis and φ_y is the rotation angle around the $\boldsymbol{y}$ axis.

Considering a generic rotation speed:

$$\boldsymbol{\omega} = \begin{Bmatrix} \omega_x \\ \omega_y \\ \omega_z \end{Bmatrix}, \tag{3.21}$$

the rotating speed around the inertial frame of reference can be calculated by accounting the rotation of each axis around a reference. In this case, the reference considered is the $\boldsymbol{x}$ axis, which leads to:

$$\begin{Bmatrix}\omega_x\\ \omega_y\\ \omega_z\end{Bmatrix} = \begin{Bmatrix}\dot{\phi}\\ 0\\ 0\end{Bmatrix} + \boldsymbol{\Theta_x}\begin{Bmatrix}0\\ \dot{\varphi}_y\\ 0\end{Bmatrix} + \boldsymbol{\Theta_x\Theta_y}\begin{Bmatrix}0\\ 0\\ \dot{\varphi}_z\end{Bmatrix}. \tag{3.22}$$

As rotations due to bending are considered small, the rotation vector becomes:

$$\begin{Bmatrix}\omega_x\\ \omega_y\\ \omega_z\end{Bmatrix} = \begin{Bmatrix}\dot{\phi} + \dot{\varphi}_z\varphi_y\\ \dot{\varphi}_y\cos(\phi) - \dot{\varphi}_z\sin(\phi)\\ \dot{\varphi}_z\cos(\phi) + \dot{\varphi}_y\sin(\phi)\end{Bmatrix}. \tag{3.23}$$

When Eq. 3.23 is applied to the kinetic energy equation, it becomes:

$$\begin{aligned} T = \int_L (\rho A(\dot{v}^2 + 2\dot{v}\dot{e}_y + \dot{e}_y^2 + \dot{w}^2 + 2\dot{v}\dot{e}_z + \dot{e}_z^2) \\ + \rho I_{xx}(\dot{\varphi}_y^2 + \dot{\varphi}_z^2) + \rho I_p(\dot{\phi}^2 + 2\dot{\phi}\dot{\varphi}_z\varphi_y + (\dot{\varphi}_z\varphi_y)^2))dx \end{aligned} \tag{3.24}$$

where I_p is the rotating inertia of the drill-string and A is the cross-section area. Once more the small bending angles simplification gives that $(\dot{\varphi}_z\varphi_y)^2 \approx 0$. Moreover, the sum $\dot{e}_y^2 + \dot{e}_z^2$ in Eq. 3.24 can be reduced to:

$$\dot{e}_y^2 + \dot{e}_z^2 = e^2\dot{\phi}^2\cos^2(\phi + \alpha_0) + e^2\dot{\phi}^2\sin^2(\phi + \alpha_0) = e^2\dot{\phi}^2. \tag{3.25}$$

3.2 Weak form and finite element formulation

From the energy equations provided, the extended Hamilton's Principle is applied to achieve a weak form of the equations of motion. In a general form, the principle is defined by:

$$\delta\mathcal{H} = \int_{t_1}^{t_2}(\delta U - \delta T - \delta W)dt = 0, \tag{3.26}$$

where δU, δT and δW are the varitions of the energies previously defined, t_1 and t_2 are an initial and final time. The variational of the problem's potential energy is:

$$\int_{t_1}^{t_2}\delta U dt = \int_{t_1}^{t_2}(\delta U_L + \delta U_{NL})dt, \tag{3.27}$$

where

$$\int_{t_1}^{t_2}\delta U_L dt =$$

$$\int_{t_1}^{t_2}\int_L [EI_{xx}(\delta v''v'' + \delta w''w'') + f_a(x)(\delta v'v' + \delta w'w') + GI_p\delta\phi'\phi']dxdt \tag{3.28}$$

and

$$\int_{t_1}^{t_2} \delta U_{NL} dt =$$

$$\int_{t_1}^{t_2} \int_L [I_{xx}\delta\phi'(E(v''w' - w''v')\cos(\phi) - E(v''v' + w''w')\sin(\phi) + G(\varphi_z\varphi_y' - \varphi_y\varphi_z'))$$
$$+I_{xx}\phi'(E(\delta v''w'+\delta w'v''-\delta w''v'-\delta v'w'')\cos(\phi)-E(\delta v''v'+\delta v'v''+\delta w''w'+\delta w'w'')\sin(\phi)$$
$$-E(v''w' - w''v')\delta\phi\sin(\phi) - E(v''v' + w''w')\delta\phi\cos(\phi)$$
$$+ GI_{xx}(\phi'(\delta\varphi_z\varphi_y' + \delta\varphi_y'\varphi_z - \delta\varphi_y\varphi_z' - \delta\varphi_z'\varphi_y) + \delta\phi'(\varphi_z\varphi_y' - \varphi_y\varphi_z'))]dxdt \quad (3.29)$$

The same is done to kinetic energy, which provides:

$$\int_{t_1}^{t_2} \delta T dt = \frac{1}{2}\int_{t_1}^{t_2}\int_L 2\rho[A(\delta\dot{v}\dot{v} + \delta\dot{w}\dot{w} + e^2\delta\dot{\phi}\dot{\phi}+$$
$$\delta\dot{e}_y\dot{v} + \delta\dot{e}_z\dot{w} + \delta\dot{v}\dot{e}_y + \delta\dot{w}\dot{e}_z)+$$
$$I_{xx}(\delta\dot{\varphi}_y\dot{\varphi}_y + \delta\dot{\varphi}_z\dot{\varphi}_z) + I_p(\delta\dot{\phi}\dot{\phi})+$$
$$+ I_p(\delta\dot{\phi}\dot{\varphi}_z\varphi_y + \delta\dot{\varphi}_z\dot{\phi}\varphi_y + \delta\varphi_y\dot{\phi}\dot{\varphi}_z)]dx \quad (3.30)$$

As the order of the integrals does not affect the calculation, it is integrated by parts in the time domain:

$$\int_{t_1}^{t_2} \delta T dt = -\frac{1}{2}\int_{t_1}^{t_2}\int_L 2\rho[A(\delta v\ddot{v} + \delta w\ddot{w} + \delta\phi e^2\ddot{\phi}+$$
$$\delta e_y\ddot{v} + \delta e_z\ddot{w} + \delta v\ddot{e}_y + \delta w\ddot{e}_z)+$$
$$I_{xx}(\delta\varphi_y\ddot{\varphi}_y + \delta\varphi_z\ddot{\varphi}_z) + I_p(\delta\phi\ddot{\phi})+$$
$$- I_p(\delta\phi(\ddot{\varphi}_z\varphi_y + \dot{\varphi}_z\dot{\varphi}_y) + \delta\varphi_z(\ddot{\phi}\varphi_y + \dot{\phi}\dot{\varphi}_y) - \delta\varphi_y\dot{\phi}\dot{\varphi}_z)]dx, \quad (3.31)$$

, for a generic variable q, $\delta q(t_1) = \delta q(t_2) = 0$. Also:

$$\delta e_y = \delta\phi e\cos(\phi + \alpha_0) \qquad \delta e_z = -\delta\phi e\sin(\phi + \alpha_0) \quad (3.32)$$

and

$$\ddot{e}_y = e\ddot{\phi}\cos(\phi + \alpha_0) - e\dot{\phi}^2\sin(\phi + \alpha_0) \quad (3.33)$$

$$\ddot{e}_z = -e\ddot{\phi}\sin(\phi + \alpha_0) - e\dot{\phi}^2\cos(\phi + \alpha_0). \quad (3.34)$$

In order to solve this variational problem, the virtual displacement is treated as a weight function. In the finite element method, the interpolation function for the weights and the displacements are alike. For the displacements:

$$v(x,t) = \boldsymbol{N}_v(x)\boldsymbol{q}^{(e)}(t), \;\; w(x,t) = \boldsymbol{N}_w(x)\boldsymbol{q}^{(e)}(t),$$

$$\varphi_y(x,t) = \boldsymbol{N}_{\varphi_y}(x)\boldsymbol{q}^{(e)}(t), \;\; \varphi_z(x,t) = \boldsymbol{N}_{\varphi_z}(x)\boldsymbol{q}^{(e)}(t), \tag{3.35}$$

$$\phi(x,t) = \boldsymbol{N}_{\phi}(x)\boldsymbol{q}^{(e)}(t) \tag{3.36}$$

where $\boldsymbol{q}^{(e)}$ is the element's generalized displacement and $\boldsymbol{N}_v$, $\boldsymbol{N}_w$, $\boldsymbol{N}_{\varphi_y}$, $\boldsymbol{N}_{\varphi_z}$ and $\boldsymbol{N}_\phi$ the element's shape functions, which are further detailed in Appendix B. As the virtual displacements are interpolated by the same shape functions, the variational problem leads to:

$$\boldsymbol{M}^{(e)}\ddot{\boldsymbol{q}}^{(e)} + \boldsymbol{K}^{(e)}\boldsymbol{q}^{(e)} = \boldsymbol{f}_{ec}^{(e)} + \boldsymbol{f}_G^{(e)} + \boldsymbol{f}_K^{(e)} + \boldsymbol{f}_M^{(e)} + \boldsymbol{f}_{Mec}^{(e)}, \tag{3.37}$$

where:

$$\boldsymbol{M}^{(e)} = \int_L (\rho A(\boldsymbol{N}_v^T\boldsymbol{N}_v + \boldsymbol{N}_w^T\boldsymbol{N}_w) + \rho I_{xx}(\boldsymbol{N}_{\varphi_y}^T\boldsymbol{N}_{\varphi_y} + \boldsymbol{N}_{\varphi_z}^T\boldsymbol{N}_{\varphi_z}) + \rho(I_p + \rho A e^2)\boldsymbol{N}_\phi^T\boldsymbol{N}_\phi)dx \tag{3.38}$$

$$\boldsymbol{K}^{(e)} = \int_L [EI_{xx}(\boldsymbol{N}_v''^T\boldsymbol{N}_v'' + \boldsymbol{N}_w''^T\boldsymbol{N}_w'') + F_a(x)(\boldsymbol{N}_v'^T\boldsymbol{N}_v' + \boldsymbol{N}_w'^T\boldsymbol{N}_w') + GI_p\boldsymbol{N}_\phi^T\boldsymbol{N}_\phi]dx \tag{3.39}$$

and the set of nonlinear generalized forces are defined on the right side of the equation. The first is:

$$\boldsymbol{f}_{ec}^{(e)} = \int_L \rho A[\boldsymbol{N}_v^T\boldsymbol{N}_\phi\boldsymbol{q}^{(e)}\boldsymbol{N}_\phi \sin(\phi+\alpha_0) + \boldsymbol{N}_w^T\boldsymbol{N}_\phi\boldsymbol{q}^{(e)}\boldsymbol{N}_\phi\cos(\phi+\alpha_0)]\boldsymbol{q}^{(e)}dx \tag{3.40}$$

as the nonlinear force due to eccentricity. As the BHA is usually heavier and with different equipment and of less regular geometry than the drill-pipes, in this work, the eccentricity is considered to be solely in this region and, as it is stiffer to torsion, ϕ and $\dot{\phi}$ are assumed constant within the BHA element. With this condition and some trigonometric properties, the force can be rewritten as:

$$\begin{aligned}\boldsymbol{f}_{ec}^{(e)} = &\int_L \rho A(e_{z_0}(x)\boldsymbol{N}_v^T - e_{y_0}(x)\boldsymbol{N}_w^T)dx\ \dot{\phi}^{(e)^2}\sin(\phi^{(e)}) \\ &+ \int_L \rho A(e_{y_0}(x)\boldsymbol{N}_v^T + e_{yz0}(x)\boldsymbol{N}_w^T)dx\ \dot{\phi}^{(e)^2}\cos(\phi^{(e)}),\end{aligned} \tag{3.41}$$

where $\phi^{(e)}$ is the torsion angle of the element and $e_{y_0}(x) = e(x)\sin(\theta_0)$ and $e_{z_0}(x) = e(x)\cos(\theta_0)$. Naturally, this force will depend on the eccentricity profile of the drill-string. In this case, the distribution along the element was considered linear in both directions, as provided in [54]. The force related to gyroscopic effects is:

$$\boldsymbol{f}_G^e = \int_L \rho I_p[\boldsymbol{N}_\phi^T\boldsymbol{N}_{\varphi_z}\dot{\boldsymbol{q}}^{(e)}\boldsymbol{N}_{\varphi_y} - \boldsymbol{N}_{\varphi_z}^T\boldsymbol{N}_\phi\dot{\boldsymbol{q}}^{(e)}\boldsymbol{N}_{\varphi_y} + \boldsymbol{N}_{\varphi_y}^T\boldsymbol{N}_\phi\dot{\boldsymbol{q}}^{(e)}\boldsymbol{N}_{\varphi_z}]\dot{\boldsymbol{q}}^{(e)}dx. \tag{3.42}$$

Forces associated with the nonlinear stiffness terms are:

$$\boldsymbol{f}_K^{(e)} =$$

$$-\int_L [EI_{xx}\boldsymbol{N}_\phi'^T(\boldsymbol{N}_v''\boldsymbol{q}^{(e)}\boldsymbol{N}_w' - \boldsymbol{N}_w''\boldsymbol{q}^{(e)}\boldsymbol{N}_v')\cos(\phi) -$$

$$EI_{xx}\boldsymbol{N}_\phi'^T(\boldsymbol{N}_v''\boldsymbol{q}^{(e)}\boldsymbol{N}_v' + \boldsymbol{N}_w''\boldsymbol{q}^{(e)}\boldsymbol{N}_w')\sin(\phi)$$

$$+EI_{xx}(\boldsymbol{N}_v''^T\boldsymbol{N}_w'\boldsymbol{q}^{(e)}\boldsymbol{N}_\phi' + \boldsymbol{N}_w'^T\boldsymbol{N}_v''\boldsymbol{q}^{(e)}\boldsymbol{N}_\phi' - \boldsymbol{N}_w''^T\boldsymbol{N}_v'\boldsymbol{q}^{(e)}\boldsymbol{N}_\phi' - \boldsymbol{N}_v'^T\boldsymbol{N}_w''\boldsymbol{q}^{(e)}\boldsymbol{N}_\phi')\cos(\phi)$$

$$-EI_{xx}(\boldsymbol{N}_v''^T\boldsymbol{N}_v'\boldsymbol{q}^{(e)}\boldsymbol{N}_\phi' + \boldsymbol{N}_v'^T\boldsymbol{N}_v''\boldsymbol{q}^{(e)}\boldsymbol{N}_\phi' + \boldsymbol{N}_w''^T\boldsymbol{N}_w'\boldsymbol{q}^{(e)}\boldsymbol{N}_\phi' + \boldsymbol{N}_w'^T\boldsymbol{N}_w''\boldsymbol{q}^{(e)}\boldsymbol{N}_\phi')\sin(\phi)$$

$$-EI_{xx}\boldsymbol{N}_\phi^T((\boldsymbol{N}_v''\boldsymbol{q}^{(e)}\boldsymbol{N}_w' - \boldsymbol{N}_w''\boldsymbol{q}^{(e)}\boldsymbol{N}_v')\sin(\phi) + (\boldsymbol{N}_v''\boldsymbol{q}^{(e)}\boldsymbol{N}_v' + \boldsymbol{N}_w''\boldsymbol{q}^{(e)]}\boldsymbol{N}_w')\cos(\phi))$$

$$+GI_{xx}\boldsymbol{N}_\phi'^T(\boldsymbol{N}_{\varphi_z}\boldsymbol{q}^{(e)}\boldsymbol{N}_{\varphi_y}' - \boldsymbol{N}_{\varphi_y}\boldsymbol{q}^{(e)}\boldsymbol{N}_{\varphi_z}') + GI_{xx}(\boldsymbol{N}_{\varphi_z}^T\boldsymbol{N}_\phi'\boldsymbol{q}^{(e)}\boldsymbol{N}_{\varphi_y}' + \boldsymbol{N}_{\varphi_y}'^T\boldsymbol{N}_\phi'\boldsymbol{q}^{(e)}\boldsymbol{N}_{\varphi_z}$$

$$-\boldsymbol{N}_{\varphi_y}^T\boldsymbol{N}_\phi'\boldsymbol{q}^{(e)}\boldsymbol{N}_{\varphi_z}' - \boldsymbol{N}_{\varphi_z}'^T\boldsymbol{N}_\phi'\boldsymbol{q}^{(e)}\boldsymbol{N}_{\varphi_y})]\boldsymbol{q}^{(e)}dx \tag{3.43}$$

Nonlinear mass components are divided in two parts, one originated by general nonlinearities:

$$\boldsymbol{f}_M^{(e)} = \int_L \rho A[\boldsymbol{N}_\phi^T\boldsymbol{N}_{\varphi_y}\boldsymbol{q}^{(e)}\boldsymbol{N}_{\varphi_z} - \boldsymbol{N}_{\varphi_z}^T\boldsymbol{N}_{\varphi_y}\boldsymbol{q}^{(e)}\boldsymbol{N}_\phi]\ddot{\boldsymbol{q}}^{(e)}dx,$$

and another closely related to the unbalanced mass:

$$\boldsymbol{f}_{Mec}^{(e)} = \int_L eA\rho[\boldsymbol{N}_\phi^T(\boldsymbol{N}_w e\sin(\phi+\alpha_0) - \boldsymbol{N}_n e\cos(\phi+\alpha_0))$$

$$-\boldsymbol{N}_v^T\boldsymbol{N}_\phi\cos(\phi+\alpha_0) + \boldsymbol{N}_w^T\boldsymbol{N}_\phi\sin(\phi+\alpha_0)]\ddot{\boldsymbol{q}}dx, \tag{3.44}$$

In order to reduce the extension in notations, the right side sum of forces developed in this section is summed as nonlinear internal forces of the element: $\boldsymbol{f}_{in}^{(e)}$. In the sequence, both the external forces and the damping models used for the analysis ought to be detailed.

3.3 Boundary conditions and external forces

In the previous section, the model development is thoroughly detailed for elemental components. In this section, the global model is written in the form:

$$\boldsymbol{M}\ddot{\boldsymbol{q}} + \boldsymbol{K}\boldsymbol{q} = \boldsymbol{f}_{in} + \boldsymbol{f}_{out}. \tag{3.45}$$

where $\boldsymbol{M}$ and $\boldsymbol{K}$ are the global mass and stiffness matrix and $\boldsymbol{f}_{in}$ en-globes nonlinear internal forces previously provided. The focus of this section is in detailing the boundary conditions and global external forces, which are contained in the vector

$\boldsymbol{f}_{out}$.

In Fig. 3.3, a sketch of the modelled drill-string is presented. In it, both lower and upper extremities are considered pinned. In other words, the controller used in the upper end limits lateral displacement - without limiting bending. The same behavior is assumed for the drill bit in the lower end. It is also considered that the speed at the top of the drill-string is constant during the whole process. This leads to another boundary condition, one of known displacement regarding the torsional dynamics. In the finite element approach, a known displacement implies in a known value of the system of differential equations. Normally, it can be treated as an external force, e.g.:

$$\begin{bmatrix} k_{11} & \cdots & k_{1n} \\ \vdots & \ddots & \vdots \\ k_{n1} & \cdots & k_{nn} \end{bmatrix} \begin{Bmatrix} q_1 \\ \vdots \\ q_n \end{Bmatrix} = \begin{Bmatrix} f_1 \\ \vdots \\ f_n \end{Bmatrix}, \tag{3.46}$$

where q_1 is known:

$$\begin{bmatrix} k_{22} & \cdots & k_{2n} \\ \vdots & \ddots & \vdots \\ k_{n2} & \cdots & k_{nn} \end{bmatrix} \begin{Bmatrix} q_2 \\ \vdots \\ q_n \end{Bmatrix} = \begin{Bmatrix} f_2 \\ \vdots \\ f_n \end{Bmatrix} - q_1 \begin{Bmatrix} f_{21} \\ \vdots \\ f_{n1} \end{Bmatrix}. \tag{3.47}$$

In the particular case of a fixed boundary, the displacement is treated as zero. From the set of equations above, it can be observed that, in practice, it is equivalent to erasing the lines and columns associated with the fixed degree of freedom.

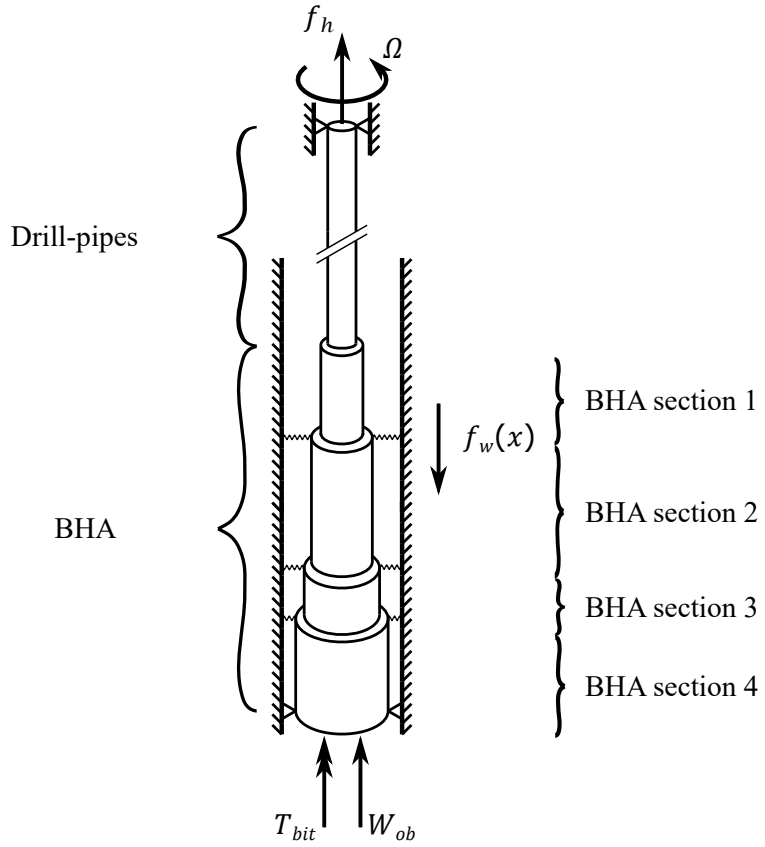

Figure 3.3: A sketch of the drill-string with constant speed at the top Ω, the hook load f_h, the weight $f_w(x)$, the weight on bit W_{ob}, torque on bit T_{bit}, springs modeling stabilizers and pinned regions.

Similarly, the force due to the constant rotation at the top is modeled as:

$$\boldsymbol{f}_\Omega = -\boldsymbol{K}_{\phi_1}\Omega t, \tag{3.48}$$

where $\boldsymbol{K}_{\phi_1}$ is the first column associated with the torsional degree of freedom of the stiffness matrix. Naturally, in the presence of a damping matrix, this force is modeled as:

$$\boldsymbol{f}_\Omega = -\boldsymbol{K}_{\phi_1}\Omega t - \boldsymbol{C}_{\phi_1}\Omega, \tag{3.49}$$

where $\boldsymbol{C}_{\phi_1}$ is a the respective column of a generic damping matrix.

Three axial forces are also depicted in Fig.3.3. The former is the weight $f_w(x)$ and the second is the hook load responsible for hoisting the system, f_h, and the last is a consequence of the contact between the drill-bit and the rock formation and, in this work, is addressed as 'weight on bit' (W_{ob}). While the weight on bit is assumed constant, the weight varies linearly within a BHA section. As axial dynamics are disregarded, it is easy to observe that:

$$f_h = W_{ob} - f_w(L), \tag{3.50}$$

where $f_w(L)$ is the weight at the end of the drill-string. In an arbitrary section, the axial force is:

$$f_a(x) = W_{ob} - f_w(x). \tag{3.51}$$

The force $f_a(x)$ is used to calculate the stiffness matrix defined in Eq. 3.39 and is a coupling term between axial and lateral dynamics. In this particular case, axial dynamics is disregarded, which leads to a linear coupling. Further development on the axial force modelling is presented in Appendix A.

Figure 3.3 also presents a torque due to the bit-rock interaction, T_{bit}. Although this torque has been extensive modelled in literature, in this work, it is based on the smooth model provided in [56, 75]:

$$T_{bit} = W_{ob} a_0 \left(\tanh(a_1 \dot{\phi}_n) + \frac{a_2 \dot{\phi}_n}{1 + a_3 \dot{\phi}_n} \right), \tag{3.52}$$

where n addresses the last node and a_0, a_1, a_2 and a_3 are model constants. In Fig. 3.4 a sample behavior of the bit rock interaction can be observed for $W_{ob} = 220$ kN. It can noticed that there is a symmetry in respect to the origin. The system, however, is not expected to achieve negative rotating speeds.

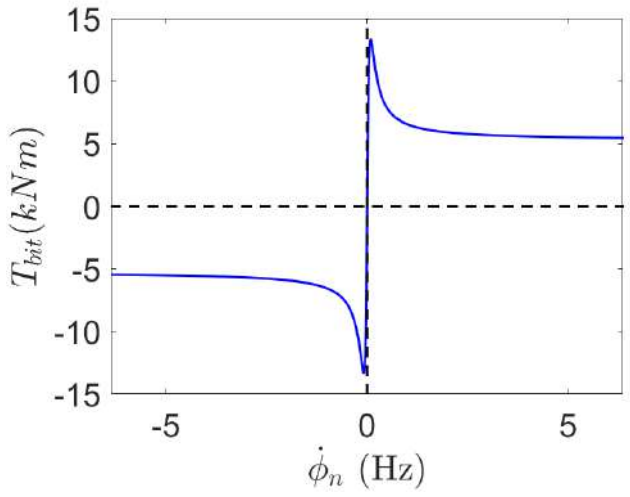

Figure 3.4: Torque on bit relation from the smooth bit-rock interaction model with a W_{ob} of 220 kN.

Stabilizers are modeled as linear springs between some points of the BHA and the borehole wall (as presented in Fig. 3.3). Briefly, this force is modeled as:

$$\boldsymbol{f}_s = -\boldsymbol{K}_s \boldsymbol{q}, \tag{3.53}$$

where $\boldsymbol{K}_s$ is a matrix containing the wall stiffness (k_{bw}) at the degrees of freedom associated with lateral displacements for the nodes with stabilizers – i.e. degrees of freedom associated with v or w. Naturally, an intuitive approach is to add a

stabilizer stiffness matrix to the global stiffness matrix:

$$\boldsymbol{K}_{eq} = \boldsymbol{K} + \boldsymbol{K}_s. \tag{3.54}$$

Finally, the model considers two contact forces, one due to the the impact with the borehole wall and another due to the rubbing between the drill-string and borehole wall. The impact force is considered as elastic during contact and, once more, acts solely in the v and w displacements degrees of freedom. In the i_{th} node, the impact force is:

$$\boldsymbol{f}_{bw_i} = \begin{Bmatrix} 0 \\ H_i(r)k_s(r_{c_i} - r_i)\sin(\theta_i) \\ H_i(r)k_s(r_{c_i} - r_i)\cos(\theta_i) \end{Bmatrix}, \tag{3.55}$$

where k_s is the borehole wall stiffness, $H(r)$ is the Heaviside function:

$$H_i(r) = \begin{cases} 1 \text{ if } r_i > r_{c_i} \\ 0 \text{ if } r_i < r_{c_i} \end{cases}, \tag{3.56}$$

r_i is the radial displacement:

$$r_i = \sqrt{v_i^2 + w_i^2} \tag{3.57}$$

and r_{c_i} is the clearance between the drill-string and the borehole wall:

$$r_{c_i} = \frac{D_{bw} - D_{o_i}}{2}, \tag{3.58}$$

where D_{bw} is the borehole wall diameter and D_{o_i} the drill-string outer diameter in the i^{th} node. In any other degree of freedom, $f_{bw_i} = 0$. Finally, θ_i is the whirl angle, where:

$$\sin(\theta_i) = \frac{v_i}{r_i} \quad \text{and} \quad \cos(\theta_i) = \frac{w_i}{r_i}. \tag{3.59}$$

The rubbing force is modelled as a smooth Coulomb friction force:

$$\boldsymbol{f}_{bw_i} = \tanh\left[V_r(D_{o_i}\dot{\phi}_i + 2r_i\dot{\theta}_i)\right] \begin{Bmatrix} 0 \\ -\mu H_i(r)k_s(r_{c_i} - r_i)\cos(\theta_i) \\ \mu H_i(r)k_s(r_{c_i} - r_i)\sin(\theta_i) \end{Bmatrix}, \tag{3.60}$$

where the first part extracts the direction of the movement and V_r as a model constant. Figure 3.5 shows the behavior of this approximation. In this case, two distinct values for the model constant are presented and, it possible to observe how the overall behavior approaches the $sign\{\}$ function as V_r is increased.

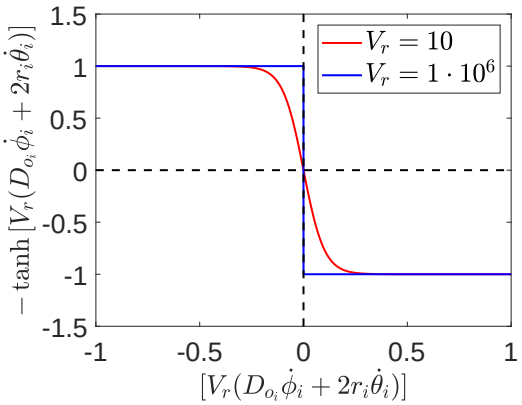

Figure 3.5: Example of the approximation of the function tanh{}.

Finally, contact forces also generate torques capable of affecting torsional dynamics. In Fig. 3.6 presents the impact forces in Cartesian coordinates through an upper view in the i^{th} node.

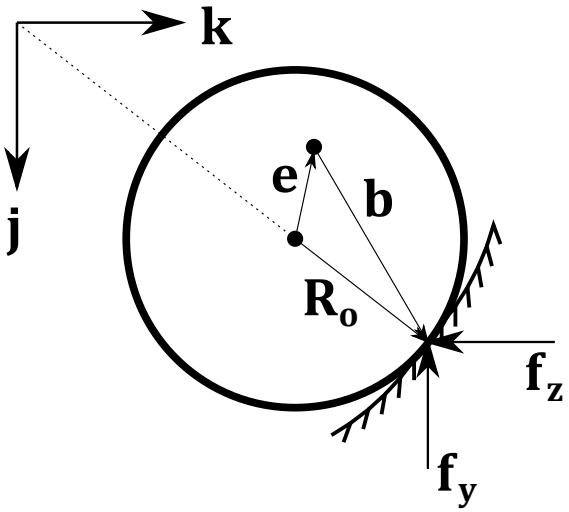

Figure 3.6: A sketch of the upper view of a drill-string section where $\boldsymbol{b}$ is the distance between the gravity center and the contact point. $\boldsymbol{f}_z$ and $\boldsymbol{f}_y$ are contact forces in their respective directions.

The distance between the impact point and the gravitational center is defined as:

$$\boldsymbol{b} = \boldsymbol{R}_0 - \boldsymbol{e}, \tag{3.61}$$

where:

$$\boldsymbol{R}_0 = \frac{1}{2}\begin{Bmatrix} 0 \\ D_{o_i}\sin(\theta_i) \\ D_{o_i}\cos(\theta_i) \end{Bmatrix}. \tag{3.62}$$

Components of impact forces are easily extracted from previous equations. The

torque due to impact can then by defined as:

$$\boldsymbol{T}_{bw_i} = \boldsymbol{b} \times \boldsymbol{f}_z + \boldsymbol{b} \times \boldsymbol{f}_y. \tag{3.63}$$

Expanding this relation, there is a resulting torque of:

$$\boldsymbol{T}_{bw_i} = H_i(r) k_s (r_{c_i} - r_i).$$

$$[(\tanh[V_r(D_{o_i}\dot{\phi}_i + 2r_i\dot{\theta}_i)]\mu \sin(\theta_i) + \cos(\theta_i))(R_{o_i}\sin(\theta_i) - e\sin(\phi_i - \alpha_0))$$
$$-(\tanh[V_r(D_{o_i}\dot{\phi}_i + 2r_i\dot{\theta}_i)]\mu \cos(\theta_i) + \sin(\theta_i))(R_{o_i}\cos(\theta_i) - e\cos(\phi_i - \alpha_0))]. \tag{3.64}$$

3.4 Reduced order model

In this section, a reduced order model is discussed. While there are several types of reduction [7], this order reduction technique is solely based on the modal reduction, which uses the modes of vibration from the linear undamped model. Those are obtained from the traditional eigenvalue problem, where $\boldsymbol{\Phi}$ and $\boldsymbol{\lambda}$ are the matrix containing the eigenvectors, or modes, and the eigenvalues, respectively. Eigenfrequencies are obtained from the square root of each eigenvalue $\omega_{n_i} = \sqrt{\lambda_i}$.

The matrix containing modal information is normalized as:

$$\boldsymbol{\Phi}^T \boldsymbol{M} \boldsymbol{\Phi} = \mathbb{I}. \tag{3.65}$$

Matrix $\boldsymbol{\Phi}$ is reduced by disregarding high order modes, i.e., by removing eigenvectors associated with frequencies outside a desired range. For example, given a matrix $\boldsymbol{\Phi}$ of size $m \times m$ and the first n relevant modes, the reduction matrix is $\boldsymbol{\Phi}_r$ of size $m \times n$. The relation between original nodal displacements and the reduced order nodal displacements is:

$$\boldsymbol{q} = \boldsymbol{\Phi}_r \boldsymbol{q}_r. \tag{3.66}$$

When the transformation is applied and the the equation is multiplied by $\boldsymbol{\Phi}_r^T$ by the left side:

$$\boldsymbol{\Phi}_r^T \boldsymbol{M} \boldsymbol{\Phi}_r \ddot{\boldsymbol{q}}_r + \boldsymbol{\Phi}_r^T \boldsymbol{C} \boldsymbol{\Phi}_r \dot{\boldsymbol{q}}_r + \boldsymbol{\Phi}_r^T \boldsymbol{K} \boldsymbol{\Phi}_r \boldsymbol{q}_r = \boldsymbol{\Phi}_r^T \boldsymbol{F}, \tag{3.67}$$

or

$$\boldsymbol{M}_r \ddot{\boldsymbol{q}}_r + \boldsymbol{C}_r \dot{\boldsymbol{q}}_r + \boldsymbol{K}_r \boldsymbol{q}_r = \boldsymbol{F}_r. \tag{3.68}$$

Yet, the first step is defining the range of modes used in the reduction. This procedure is explained on the Appendix D, based on the response of the non-reduced model.

Chapter 4

Damping models

4.1 Deterministic damping models

In order to model the damping of the structure, different strategies were adopted. While torsional stick-slip vibrations are often classified as a low-frequency phenomenon, it is a source of excitation in the lateral degrees of freedom of a coupled model. Although its frequency is low, some parts of the drill-string goes from near – or complete – stagnation to high rotating speeds. In other words, this low frequency torsional vibration actually provides a wide spectrum of excitation frequencies for coupled lateral vibrations. In addition, during a backward whirl regime, the whirl frequency can be seen as a function of the gap between the drill-string and the borehole wall and the excitation frequency. Both phenomena can be concomitant and thus, a combination of stick-slip and backward whirl can present a broad spectrum of excitation frequencies. Simultaneously, some fluid models, such as presented in [31], consider higher damping when higher frequencies are applied – which only adds to the system's complexity. The main objective of this section is not only to provide distinct models, with different characteristics –to capture and simplify effects, such as fluid interaction – but also to help understand the consequences of those characteristics in a complex coupled dynamic.

In every approach presented in this work, the damping matrix is divided in two distinct parts:

$$\boldsymbol{C} = \boldsymbol{C}_T + \boldsymbol{C}_L, \tag{4.1}$$

where $\boldsymbol{C}_T$ is the damping solely in torsional vibrations and $\boldsymbol{C}_L$ is the damping mainly in lateral vibrations. The former is considered to be:

$$\boldsymbol{C}_T = b_1 \boldsymbol{M}_T + b_2 \boldsymbol{K}_T, \tag{4.2}$$

where $\boldsymbol{M}_T$ and $\boldsymbol{K}_T$ are the linear inertia and stiffness matrices associated with

torsional degrees of freedom and $b_1 \in \mathbb{R}^+$ and $b_2 \in \mathbb{R}^+$ are model constants.

The latter, will be modeled through three distinct approaches: (1) Rayleigh proportional damping, (2) arbitrary fitted function and (3) polynomial fitted damping ratio – or the extended Rayleigh damping [12]. For cases (2) and (3), the approach used is in accordance with the methodology presented in [1].

For this, curves adjusted from the information provided in [16] were used. Those values are from experimental analysis in a simply supported beam. Even though different from the work at hand, it was used as a base to model the damping. The values provided in said work are presented in Tab. 4.1.

Table 4.1: Table with damping coefficient provided in [16].

ξ (%)	ω (Hz)	ω^*
0.40	6.78	1.00
0.20	26.93	3.97
0.27	60.46	8.92
0.38	106.59	15.72
0.40	166.46	24.55
0.44	242.49	35.77

For every model, the first step is used with an dimensionless notation. For it, the first natural frequency was used for the dimensionless frequency:

$$\omega^{(*)} = \frac{\omega}{\omega_1} \tag{4.3}$$

1. When the Rayleigh proportional damping is used, the relation between damping ratio and frequency is given by [84]:

$$\xi(\omega^{(*)}) = \frac{1}{2}\left(\frac{b_1^{(*)}}{\omega^*} + b_2^{(*)}\omega^{(*)}\right). \tag{4.4}$$

   Parameters $b_1^{(*)}$ and $b_2^{(*)}$ are calculated from the experimental data. In sequence, dimensional parameters are calculated by:

$$b_{L_1} = b_1^{(*)}\omega_1 \qquad \text{and} \qquad b_{L_2} = \frac{b_2^{(*)}}{\omega_1} \tag{4.5}$$

   which leads to a damping defined as:

$$\boldsymbol{C}_{L_1} = b_{L_1}\boldsymbol{M}_L + b_{L_2}\boldsymbol{K}_L, \tag{4.6}$$

   where both the models constants b_{L_1} and $b_{L_2} \in \mathbb{R}_+$.

2. One consequence of the Rayleigh proportional damping model is that it leads

to high damping ratios in higher frequencies. In order to better adjust the damping ratio experimental data, a new curve is proposed as:

$$\xi = \frac{1}{2}\left(\frac{\beta_1}{\omega} + \beta_2\sqrt{\omega}\right). \tag{4.7}$$

Although the first term of the equation coincides with the Rayleigh proportional damping, the second term was chosen in order to minimize overdamping the system.

Constants β_1 and β_2 were calculated by adjusting the dimensionless curve with the least square method:

$$\xi = \frac{1}{2}\left(\frac{\beta_1^{(*)}}{\omega^*} + \beta_2^*\sqrt{\omega^*}\right). \tag{4.8}$$

Next, the relations:

$$\beta_1 = \beta_1^*\omega_1 \qquad \text{and} \qquad \beta_2 = \frac{\beta_2^{(*)}}{\sqrt{\omega_1}} \tag{4.9}$$

were used to finally calculate the model's constants, once more, those can only assume positive values: β_1 and $\beta_2 \in \mathbb{R}_+$.

Applying the procedure detailed in [1], the damping matrix can be obtained by:

$$\boldsymbol{C}_{L_2} = \beta_1\boldsymbol{M}_L + \beta_2\boldsymbol{M}_L(\boldsymbol{M}_L^{-1}\boldsymbol{K}_L)^{3/4}, \tag{4.10}$$

where the operation $\sqrt{A} = B$ where $B^TB = A$. Further details regarding how matrix $\boldsymbol{C}_{L_2}$ are provided in Appendix C.

3. This last model is originated from the same set of data, where the curve was interpolated through a polynomial relation – an extended Rayleigh proportional damping approach [12]. In order to simplify the operation and avoid higher order matricial roots, exponents of the polynomial were chosen in a fashion where:

$$\xi = \sum_{n=0}^{k} c_n\omega^{2n-1}. \tag{4.11}$$

The dimensionless equation can be written as:

$$\xi = \sum_{n=0}^{k} c_n^{(*)}\omega^{(*)^{2n-1}}, \tag{4.12}$$

and the coefficients are calculated as:

$$\gamma_k = \frac{c_n^{(*)}}{\omega_1^{2n-1}} \tag{4.13}$$

Once more, the procedure leads to:

$$\boldsymbol{C}_{L_3} = 2\boldsymbol{M}_L^{-1} \sum_{n=0}^{k} c_n (\boldsymbol{M}_L^{-1}\boldsymbol{K}_L)^n. \tag{4.14}$$

However, matrix operations often leads to numerical error. In this case, even though the inversion o the matrix $\boldsymbol{M}_L$ leads to small errors, the operation $\boldsymbol{M}_L^{-k}$ may be problematic for high values of k. Hence, in order to obtain smaller values, the second and the third experimental points were not used. While it can be possible that $c_n \in \mathbb{R}$ – assuming a finite range of damped frequencies – having $c_n \in \mathbb{R}_+$ guarantees that $\xi(\omega) \in \mathbb{R}_+$. This relation can be verified in Eq. 4.11.

In Fig. 4.1 presents the dimensionless curves and the dimensionless experimental data. As expected, the second curve provides smaller damping ratios in higher frequencies – and slightly greater ratios for lower frequencies. For the polynomial fitting, it can be seen that ignoring the second and the third points did not present discrepancies in the curves fitting.

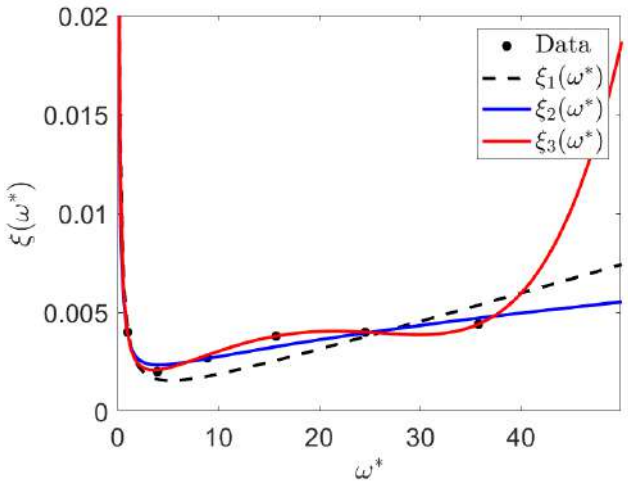

Figure 4.1: Dimensionless curves proposed when compared with dimensionless experimental data provided in [16].

4.2 Stochastic non-proportional damping model

The damping models previously developed are different structures of proportional damping. This, however, is not necessarily true: a structure may present non-

proportional damping, specially considering the nonlinear nature of the problem and the fluid-structure interaction. Hence, in this section, stochastic damping models are developed to account for uncertainties in the deterministic models, including errors in the proportionality assumption. There are two main objectives to this approach. The former is, as aforementioned, to model errors in the deterministic modeling strategy, as the damping coefficients achieved with those models can vary from the obtained - specially considering that only the first six natural frequencies are available. The latter, is to add off-diagonal terms, acknowledging that a nonlinear structure with fluid interaction might not be proportionally undamped.

The random damping matrix follows the procedure developed in [71], where a random positive semi-definite matrix is generated. The choice of a positive-definite damping guarantees the stability of the final system. As detailed in [64], a random matrix ensemble can be achieved by:

$$\hat{\boldsymbol{C}} = \boldsymbol{L}^T \hat{\boldsymbol{G}} \boldsymbol{L}, \tag{4.15}$$

where $\hat{\boldsymbol{C}}$ is a random damping in the modal base, $\boldsymbol{L}$ is an upper triangular matrix where $\boldsymbol{L}^T\boldsymbol{L} = \boldsymbol{\Phi}^T\boldsymbol{C}\boldsymbol{\Phi}$ and $\hat{\boldsymbol{G}}$ is a random germ matrix of mean value equal the identity matrix.

To generate the germ matrix, consider an upper triangular matrix $\hat{\boldsymbol{U}}_G$, where $\hat{\boldsymbol{U}}_{G_{ij}}$ follows a normal distribution of zero mean and variance of $\sigma_{var} = \delta(m+1)^{-1/2}$ if $i < j$ and, if $i = j$, $\hat{\boldsymbol{U}}_{G_{ij}} = \delta[2(m+1)\hat{V}_i]^{-1/2}$, where $\hat{V}_i$ follows a gamma distribution with unitary scale parameter and shape parameter as $(m+1)/2\delta + (1 - i/2)$. The constant m is the system's dimension, i and j refers to the matrix element in the i^{th} line and j^{th} column, and δ the dispersion parameter given by:

$$\delta = \frac{1}{m}\mathrm{E}\{||\boldsymbol{G} - \mathbb{I}||^2\}^{1/2}. \tag{4.16}$$

With the $\boldsymbol{U}_G$ matrix, the germ matrix is expressed as $\hat{\boldsymbol{G}} = \hat{\boldsymbol{U}}_G^T\hat{\boldsymbol{U}}_G$. Even though the stochastic damping model was considered only in lateral directions, each was assumed uncoupled from the other. For that, a reduced system considering only lateral degrees of freedom was obtained by excluding torsional degrees of freedom. In sequence, each direction was separated in two distinct – however equivalent – unforced system of equations:

$$\boldsymbol{M}_y\ddot{\boldsymbol{q}}_y + \boldsymbol{C}_y\dot{\boldsymbol{q}}_y + \boldsymbol{K}_y\boldsymbol{q}_y = \boldsymbol{0} \tag{4.17}$$

and

$$\boldsymbol{M}_z\ddot{\boldsymbol{q}}_z + \boldsymbol{C}_z\dot{\boldsymbol{q}}_z + \boldsymbol{K}_z\boldsymbol{q}_z = \boldsymbol{0}, \tag{4.18}$$

where $\boldsymbol{M}_y$, $\boldsymbol{C}_y$, $\boldsymbol{K}_y$ and $\boldsymbol{q}_y$ are the mass, damping, stiffness and nodal degrees of freedom in the **j** direction and $\boldsymbol{M}_z$, $\boldsymbol{C}_z$, $\boldsymbol{K}_z$ and $\boldsymbol{q}_z$ are the mass, damping, stiffness and nodal degrees of freedom in the **k** direction. This lateral damping matrix can be any of those models previously presented. Considering the eigenvalue problem of undamped system, the lateral eigenfrequencies $\boldsymbol{\Omega}_y$ and $\boldsymbol{\Omega}_z$ are obtained from the Eqs. 4.17 and 4.18. The eigenmodes obtained – and normalized – are presented as $\boldsymbol{\Phi}_y$ and $\boldsymbol{\Phi}_z$ for the same respective equations. Due to the symmetry, the eigenfrequencies calculated are the same: $\boldsymbol{\Omega}_L = \boldsymbol{\Omega}_y = \boldsymbol{\Omega}_z$. In the modal base, the matrices can be rewritten as:

$$\begin{aligned}
\boldsymbol{\Phi}_y^T \boldsymbol{M}_y \boldsymbol{\Phi}_y &= \boldsymbol{\Phi}_z^T \boldsymbol{M}_z \boldsymbol{\Phi}_z = \mathbb{I} \\
\boldsymbol{\Phi}_y^T \boldsymbol{K}_y \boldsymbol{\Phi}_y &= \boldsymbol{\Phi}_z^T \boldsymbol{K}_z \boldsymbol{\Phi}_z = \boldsymbol{\Omega}_L^2 \\
\boldsymbol{\Phi}_y^T \boldsymbol{C}_y \boldsymbol{\Phi}_y &= \boldsymbol{\Phi}_z^T \boldsymbol{C}_z \boldsymbol{\Phi}_z = \boldsymbol{C}_L^{(m)}.
\end{aligned} \tag{4.19}$$

The random lateral damping matrix was then generated by:

$$\hat{\boldsymbol{C}}_L = \boldsymbol{L}_L^T \hat{\boldsymbol{G}} \boldsymbol{L}_L, \tag{4.20}$$

where $\boldsymbol{C}_L^{(m)} = \boldsymbol{L}_L^T \boldsymbol{L}_L$. Hence, in the modal base, the damping matrices for both directions are the same, preserving the symmetry of the system. As an example, consider a three degrees of freedom proportional damping matrix in the modal base:

$$\boldsymbol{C}^{(m)} = \begin{bmatrix} 2\xi_1\omega_{n_1} & 0 & 0 \\ 0 & 2\xi_2\omega_{n_2} & 0 \\ 0 & 0 & 2\xi_3\omega_{n_3} \end{bmatrix}, \tag{4.21}$$

where $\xi_i = \xi(\omega_{n_i})$ is always positive. The Cholesky decomposition is:

$$\boldsymbol{L}_L = \begin{bmatrix} \sqrt{2\xi_1\omega_{n_1}} & 0 & 0 \\ 0 & \sqrt{2\xi_2\omega_{n_2}} & 0 \\ 0 & 0 & \sqrt{2\xi_3\omega_{n_3}} \end{bmatrix} \tag{4.22}$$

and $\boldsymbol{L}_L = \boldsymbol{L}_L^T$. In accordance with this random matrix ensemble, a viable value for $\hat{\boldsymbol{G}}$ is of the form:

$$\hat{\boldsymbol{G}} = \begin{bmatrix} 1.0983 & 0.0164 & -0.0453 \\ 0.0164 & 0.9889 & -0.0022 \\ -0.0453 & -0.0022 & 1.0179 \end{bmatrix}. \tag{4.23}$$

The stochastic damping can be calculated as:

$$\hat{\boldsymbol{C}}^{(m)} = \boldsymbol{L}_L^T \hat{\boldsymbol{G}} \boldsymbol{L}_L : \tag{4.24}$$

$$\hat{\boldsymbol{C}}^{(m)} = \begin{bmatrix} 2.190\ \xi_1\omega_{n_1} & 0.032\sqrt{\xi_1\omega_{n_1}\xi_2\omega_{n_2}} & 0.091\sqrt{\xi_1\omega_{n_1}\xi_3\omega_{n_3}} \\ 0.032\sqrt{\xi_1\omega_{n_1}\xi_2\omega_{n_2}} & 1.978\ \xi_2\omega_{n_2} & -0.004\sqrt{\xi_2\omega_{n_2}\xi_3\omega_{n_3}} \\ 0.091\sqrt{\xi_1\omega_{n_1}\xi_3\omega_{n_3}} & -0.004\sqrt{\xi_2\omega_{n_2}\xi_3\omega_{n_3}} & 2.036\ \xi_3\omega_{n_3} \end{bmatrix}. \quad (4.25)$$

From the example above, it is possible to see that the damping is non proportional yet, it is still symmetric and positive definite.

Chapter 5

Results

In this section, the results obtained from the model are presented. Initially, the properties of the model are shown followed shortly by a convergence analysis. In the sequence, comparisons between the model and its respective simplification are presented with time-domain simulations.

For all the simulations provided, the same eccentricity profile was adopted. As stated previously in Chapter 3.2, the eccentricity chosen behaves linearly. In order to simplify the analysis, it was assumed that the modulus of the eccentricity $e = |\boldsymbol{e}|$ is constant and that $e = 0.05D_o$ of the respective section. The phase angle θ_0 was assumed to vary from π in each BHA section. As it can be seen in Fig. 5.1, two consecutive BHA sections will present eccentricity in opposite directions.

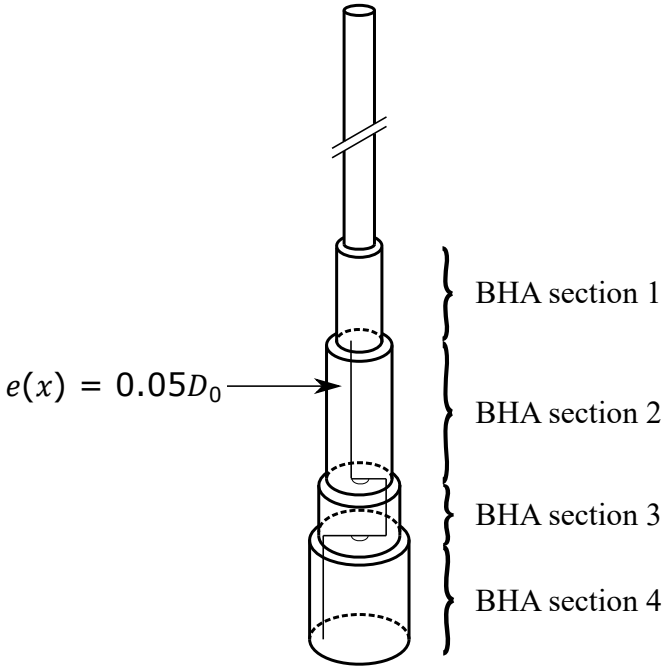

Figure 5.1: A sketch of the eccentricity profile used.

In Tab. 5.1, overall information regarding the drill-string properties are pre-

sented, including the dimensions of each BHA section.

Table 5.1: Summary of drill-string properties.

Parameter	Symbol	Values	Units	Parameter	Symbol	Values	Units
Young's Modulus	E	210	GPa	Inner diameter of Drill-pipes	D_{pi}	0.1281	m
Poisson ratio	G	0.30	-	Length of BHA section 1	L_{BHA1}	273.11	m
Drill-pipe density	ρ	7800	kg/m^3	Outer diameter of BHA section 1	D_{BHA1_o}	0.1692	m
Torsional proportional damping coeff.	b_1	0.35	s^{-1}	Inner diameter of BHA section 1	D_{BHA1_i}	0.1016	m
Torsional proportional damping coeff.	b_2	0.06	s	Length of BHA section 2	L_{BHA2}	115.55	m
Contact stiffness	k_s	$1 \cdot 10^6$	N/m	Outer diameter of BHA section 2	D_{BHA2_o}	0.2023	m
Wall friction coeff.	μ	0.30	-	Inner diameter of BHA section 2	D_{BHA2_i}	0.0768	m
Gravity	g	9.81	m/s^2	Length of BHA section 3	L_{BHA3}	163.63	m
T_{bit} model constant	a_0	0.024	m	Outer diameter of BHA section 3	D_{BHA3_o}	0.2413	m
T_{bit} model constant	a_1	1.910	s	Inner diameter of BHA section 3	D_{BHA3_o}	0.0768	m
T_{bit} model constant	a_2	8.500	s	Length of BHA section 4	L_{BHA4}	29.30	m
T_{bit} model constant	a_3	5.470	s^2	Outer diameter of BHA section 4	D_{BHA4_o}	0.2420	m
Length of Drill-pipe	L_p	2000	m	Inner diameter of BHA section 4	D_{BHA4_o}	0.0759	m
Outer diameter of Drill-pipe	D_{po}	0.1492	m	Borehole wall diameter	D_{bit}	0.416	m

In order to conduct the numerical simulations, the MATLAB environment was used. In it, symbolical mathematics was used to create the elemental matrices – both linear and nonlinear–, next, a code for the system's global assembly was implemented for every model, including reduced order models, and the central difference method was applied for time-domain integrations. In accordance to [85], explicit methods such as this is well-suited for impact dynamics due to the need of reduced time steps. As the system of equations may reach high dimensions, methods that require a state-space formulation are, although popular, prohibitively time-consuming. Hence, the central difference method was chosen for each time-domain integration. For the complete order model, the time-step converged when $\Delta t = 2.5 \cdot 10^{-4}$ s. The reduced-order model with the first five hundred modes converged with a time-step of $\Delta t = 1 \cdot 10^{-2}$ s. Further comparison between full-order and reduced-order models are presented in Appendix D.

5.1 Mesh convergence analysis

The mesh convergence analysis considers, as a reference, the model without nonlinearities and is divided in two steps. The former, evaluates the natural frequencies obtained through the model with different meshes. If all the frequencies converge to the same values within a established frequency threshold, it is considered as converged. The latter, consists in a Modal Assurance Criterion [57], that is used to evaluate the correlation of modes when the number of elements is increased. If all the modes in the threshold present a high correlation ($\mathcal{M} > 0.99$) with a mesh of higher density, it is considered as converged. Finally, the mesh where both these conditions are met is used for subsequent simulations. In Tab. 5.2, the number of elements used in analysis are presented. In this section, the converge results shown are for $W_{ob} = 220$ kN.

Table 5.2: Element distribution.

Region	n	$2n$	$3n$	$4n$	$5n$
Drill-pipes	48	96	144	192	240
BHA 1	24	48	72	96	120
BHA 2	12	24	36	48	60
BHA 3	12	24	36	48	60
BHA 4	4	8	12	16	20
Total d.o.f.	500	1000	1500	2000	2500

In Fig. 5.2, natural frequencies obtained for the meshes are depicted. Figure 5.2a presents solely torsional frequencies while Fig. 5.2b lateral frequencies in one of the directions i.e., redundant frequencies due to the symmetry around the x-axis are

not presented. A traced line points the maximum expected frequency for the drill-string modelled. Even though the rotation applied in the top will seldom be close to the threshold provided, some of the nonlinear phenomena might implicate in higher frequencies. From Fig. 5.2a, frequency convergence is achieved with the first mesh for torsional degrees of freedom. However, from Fig. 5.2b, lateral eigenfrequencies converge only on the second mesh. It can also be observed that, whereas only some torsional natural frequencies are contained in the established threshold, more than a hundred and fifty lateral eigenfrequencies are found in the same interval.

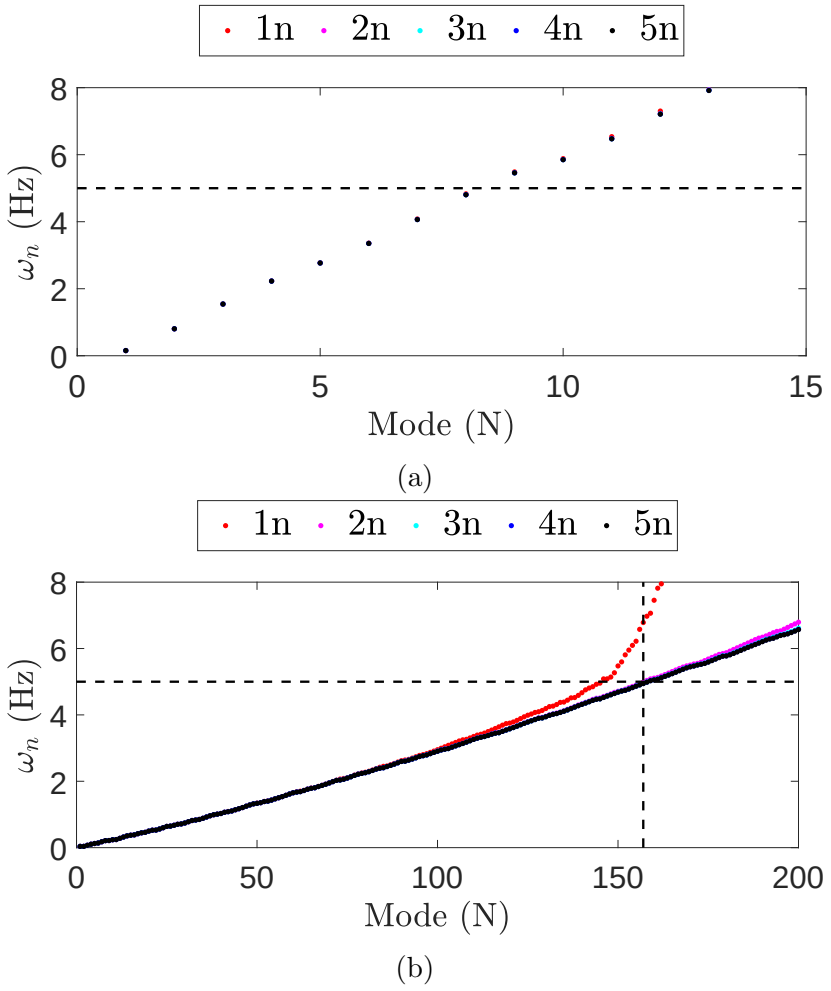

Figure 5.2: Natural frequencies obtained through the model with different meshes. In (a) are depicted torsional frequencies for each mode and in (b) lateral frequencies.

The MAC analysis consists in the correlation between two modes. In this case, it can be represented as:

$$\mathcal{M}_{ij} = \frac{|\Phi_i^T \Phi_j|}{(\Phi_i^T \Phi_i)(\Phi_j^T \Phi_j)}, \tag{5.1}$$

where Φ_m is the eigenvector of the m^{th} mode. This provides a matrix $\mathcal{M}_{ij} \in [0, 1]$ that contains the correlation between every lateral mode. When $i = j$, it is expected that $\mathcal{M}_{ii} \approx 1$, which would correspond to similar modes. For this analysis, only the

correlation between correspondent modes is studied, and hence, only the values of $\mathcal{M}_{ii}$ are presented.

In Fig. 5.4, lateral modal correlation are presented for each mesh. Each color depicts $\mathcal{M}$ between two meshes for the first two hundred modes. The modes obtained by the last mesh ($5n$) were used as reference for the comparison. As before, the first mesh clearly diverges. In this case, however, the divergence of the second mesh was also observed. At first glace, the third mesh seems to diverge only after the threshold. However, under close inspection, it can be observed that it starts to diverge close to the 140^{th} mode. Hence, a safe mesh choice is the fourth mesh, where the first signs of divergence are close to the second hundred of modes.

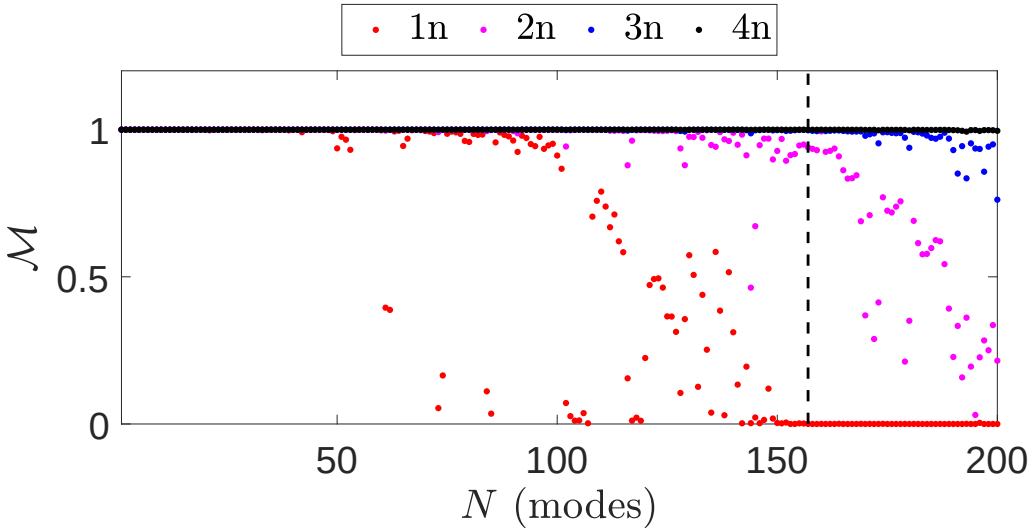

Figure 5.3

Figure 5.4: Modal Assurance Criterion applied to different meshes. In this case, each mesh was compared with the one with more elements.

5.2 Complete and simplified models

In this section, the effects of nonlinearities presented in the forces $\boldsymbol{f}_K$, $\boldsymbol{f}_M$ and $\boldsymbol{f}_G$ are studied (Eqs. 3.42 through 3.44 in global coordinates). In other words, nonlinear forces due to the unbalance were kept. This is achieved through comparison between simulations with and without said forces. The former model is referred as the 'complete model', while the latter as the 'simplified model'.

In this section, three distinct cases are presented. The first with severe torsional vibrations and forward whirl, the second without severe torsional vibration and with forward whirl and the third with severe torsional vibrations and backward whirl. Case 1 is presented in Fig. 5.5, with $W_{ob} = 220$kN and $\Omega = 0.67$ Hz. In Fig. 5.5a, radial displacement is shown for the middle node in the last BHA section

and an arbitrary time interval is zoomed. In Fig. 5.5b, the bit rotational speed development through time is depicted. For this case, it is clear that the nonlinear forces did not present a sensible impact in the dynamic.

The second case is depicted in Fig. 5.6. For this simulation considered $W_{ob} =$ 100kN and $\Omega = 1.33$ Hz. In summary, the same conclusion can be drawn from Case 1: that the nonlinearities had no major effect in the dynamics.

Figure 5.7 shows the third case, $W_{ob} = 220$kN and $\Omega = 1$ Hz. It can be noticed that the results diverge after a few seconds. This is observed because a region in the drill-string impacts the borehole wall and its effects are propagated to the observed node. This phenomenon leads to different quantitative results when the simplification is applied. Although the physical accuracy of the simplified model might quantitatively diverge from the complete model, the former can accurately qualitatively represent the dynamic. In other words, the simplified model successfully identifies the impact point, the severe torsional vibration and the whirl regimen.

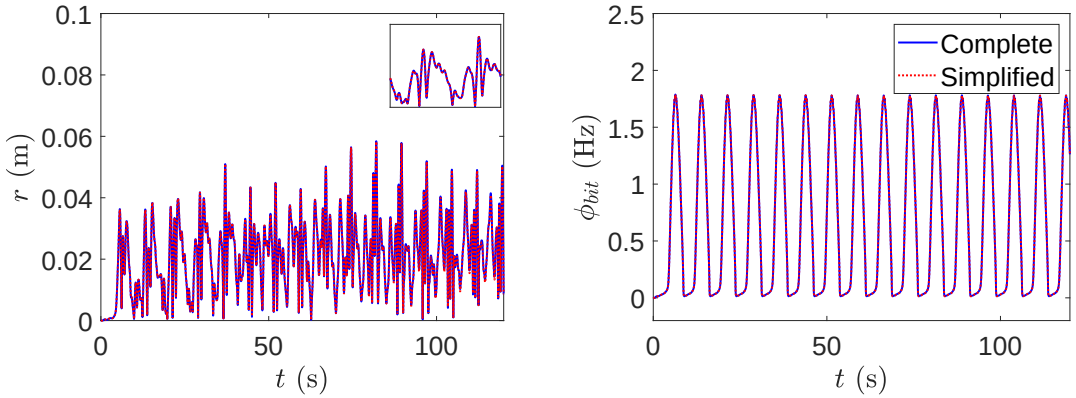

(a) (b)

Figure 5.5: Numerical simulations for the complete and simplified models for $\Omega =$ 0.67 Hz (40 rpm) and $W_{ob} = 220$ kN.

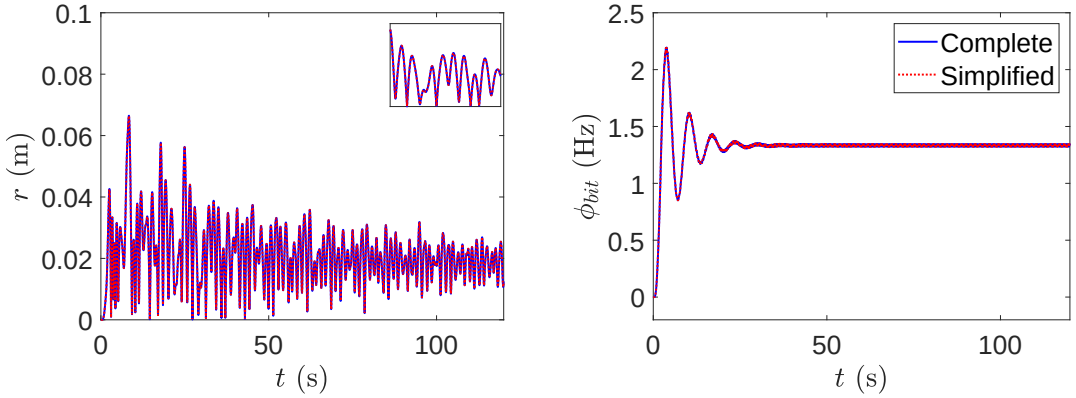

(a) (b)

Figure 5.6: Numerical simulations for the complete and simplified models for $\Omega =$ 1.67 Hz (80 rpm) and $W_{ob} = 100$ kN.

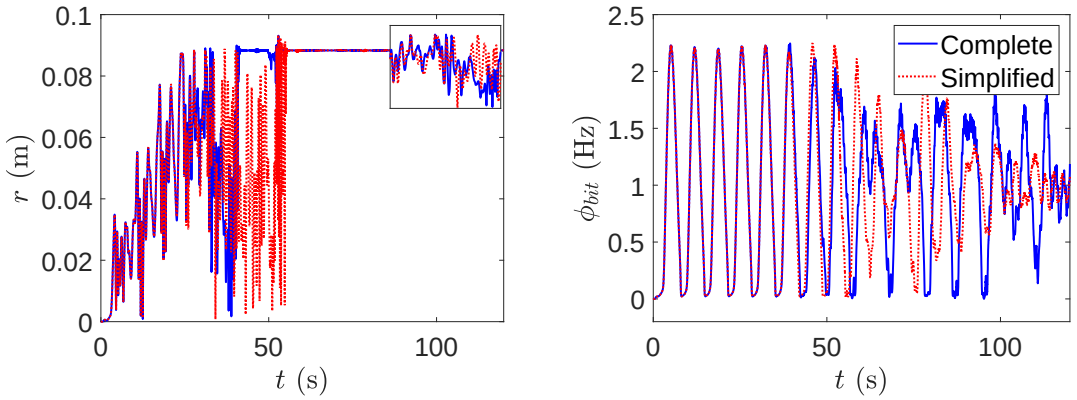

(a) (b)

Figure 5.7: Numerical simulations for the complete and simplified models for $\Omega = 1.00$ Hz (60 rpm) and $W_{ob} = 220$ kN.

Finally, it can be seen that, without impact, the simplified model presents similar results when compared with the complete model and, while the impact may lead to different dynamics, the result is, in general, qualitatively equivalent. As the numerical integration of nonlinear matrices are computationally expensive, the simplified model presents faster performance. Hence, from this point onward this simplification is adopted for most of the numerical simulations in this work.

5.3 Deterministic response

This section is divided in three parts: (i) phenomena identification analysis, (ii) damping effects and (iii) dynamics maps. In order to evaluate the response in time domain, some criteria is defined. Those are used to identify possible phenomena as severe torsional vibrations, forward whirl and backward whirl.

Severe torsional vibrations are evaluated by the measure of a normalized amplitude coefficient, known as the torsional vibration severity index. This index considers the minimum and maximum bit speeds in the steady state:

$$S = \frac{\dot{\phi}^{st}_{max} - \dot{\phi}^{st}_{min}}{2\Omega}, \tag{5.2}$$

where ϕ^{st}_{max} and ϕ^{st}_{min} are the maximum and minimum bit speed in the steady state. A severe torsional vibration is assumed if $S > 0.8$.

The type of whirl is analysed from a fast Fourier transform (FFT) on the simulated data. For that, information is rewritten in polar complex coordinates as:

$$z_i = v_i + jw_i, \tag{5.3}$$

where v_i and w_i are, as previously described, the displacements in the i^{th} node

and z_i is the radius in complex coordinates. Finally, the complex unit is defined as: $j = \sqrt{-1}$. In sequence, the transform is applied to z_i. Frequencies provided by this analysis are the whirl frequency whereas the sign indicates the direction of the movement. In other words, negative frequencies indicates backward whirl. The structure may present both forward and backward whirls due to its flexible behavior. Hence, the dominating frequency is tracked. In order to identify it, the frequency of highest amplitude is analyzed and, if it is a negative frequency, the drill-string is considered to be in a backward whirl regime.

Both of these criteria are applied in a final fraction of the data, considering only the last 20% of the simulation in order extract a steady state response. As the system presents nonlinearities, a time interval for the integration was chosen to capture any possible impact and its aftermath.

5.3.1 Phenomena identification

At this part, different phenomena is detailed. With the previous definition, four distinct events are assumed possible: (i) no torsional vibration, (ii) severe torsional vibration, (iii) forward whirl and (vi) backward whirl. However, lateral and torsional vibrations are not mutually exclusive, i.e.: it is possible to have severe torsional vibrations with a backward whirl. Hence, the objective of this section is to present, separately, each phenomena to exemplify and characterize the evaluation criteria previously presented.

In Fig. 5.8, torsional speed at the bit is presented for three different cases. The first case, there is a drilling configuration of $W_{ob} = 100$ kN and a rotation applied of $\Omega = 1.33$ Hz, the second a $W_{ob} = 220$ kN and a rotation applied of $\Omega = 0.67$ Hz and the third of $W_{ob} = 160$ kN and a rotation applied of $\Omega = 1.75$ Hz. For the first case, when the amplitude coefficient $\mathcal{S}$ is calculated, it can be seen that it is close to zero ($\mathcal{S}_{100,1.33} \approx 0$). For the second case, a high amplitude coefficient can be seen ($\mathcal{S}_{220,0.67} > 0.80$), and thus, it is classified as severe. The last case, it can be observed that, whereas no severe torsional vibration is seen, some torsional vibration is presented ($\mathcal{S}_{160,1.75} < 0.80$). The main difference is that the former case, the severe torsional vibration is a consequence of the bit-rock interaction, while the latter is induced by the lateral impact between the drill-string and the borehole wall.

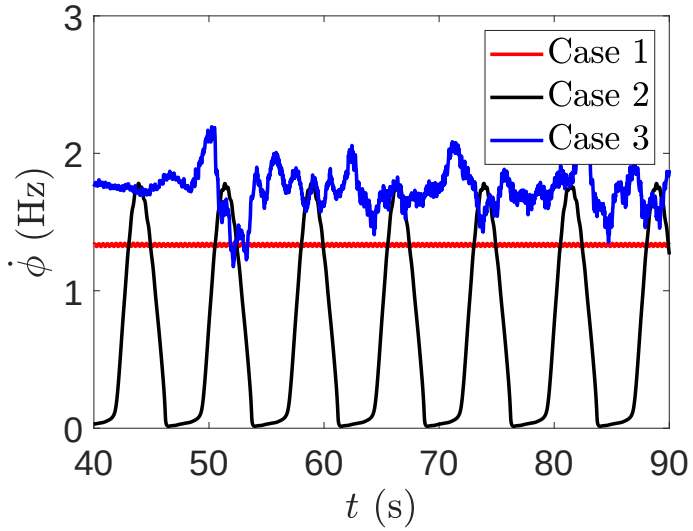

Figure 5.8: Torsional speed at the bit for numerical simulations in different drilling configurations: Case 1 presents $\Omega = 1.33$ Hz (80 rpm) and $W_{ob} = 100$ kN with $\mathcal{S}_{100,1.33} > 0.008$; Case 2 presents $\Omega = 0.67$ Hz (40 rpm) and $W_{ob} = 220$ kN with $\mathcal{S}_{220,0.67} = 1.328$; Case 3 presents $\Omega = 1.75$ Hz (105 rpm) and $W_{ob} = 160$ kN with $\mathcal{S}_{160,1.75} = 0.634$

In Figs. 5.9b and 5.9a presents the dominant whirl frequencies and the radial displacements, respectively. Now, two distinct cases are shown: case 1, with $W_{ob} = 100$ kN and a rotation applied of $\Omega = 1.33$ and case 2, with $W_{ob} = 160$ kN and a rotation applied of $\Omega = 1.75$. In the first case, it can be seen that the whirl frequency of greatest amplitude is positive, indicating a forward whirl. The second case, a negative whirl frequency dominates the dynamics. When the radial displacement is observed, it can be seen that the forward whirl case is far from the clearance allowed for that node, while the second case, the displacement is higher than the clearance available – the drill-string slightly penetrates the borehole wall in permanent contact.

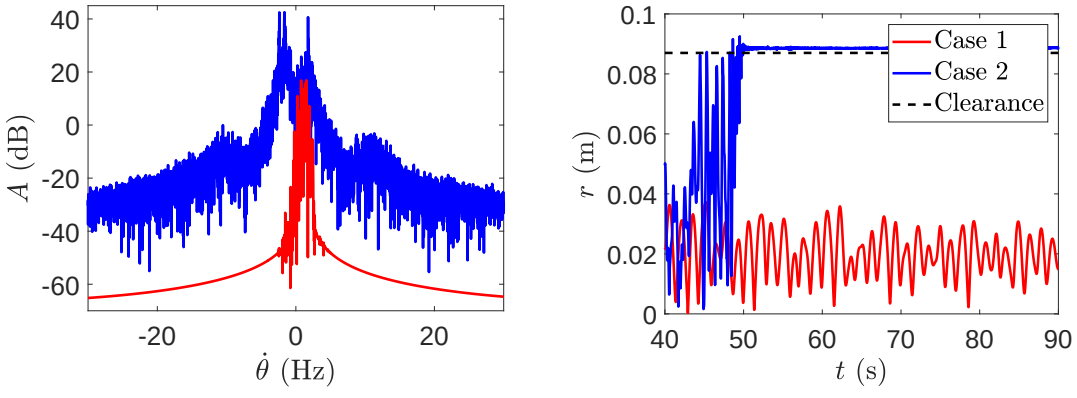

(a) (b)

Figure 5.9: Lateral data for numerical simulations in different drilling configurations: Case 1 presents $\Omega = 1.33$ Hz (80 rpm) and $W_{ob} = 100$ kN; Case 2 presents $\Omega = 1.75$ Hz (105 rpm) and $W_{ob} = 160$ kN. In (a) the highest whirl frequency of greater amplitude and in (b) the radial displacement is presented.

The simulation with contact and backward whirl is the same of the data that presented torsional vibrations of lower intensity (Case 3), which reinforces the argument that contact torques can lead to torsional vibrations.

5.3.2 Damping models dynamics

At this point, the results of deterministic damping models are presented. As an reference, Fig. 5.10 presents the damping ratios for each model provided in different frequencies.

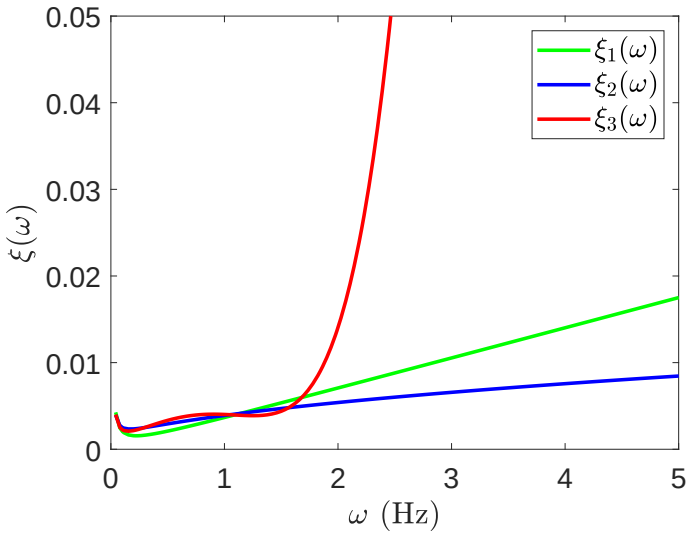

Figure 5.10: Damping ratios inside the frequency threshold established.

In Fig. 5.11 the dynamics in the three different damping models can be seen with $W_{ob} = 100$ kN and $\Omega = 1.33$ Hz. In a continuous blue line, the Rayleigh proportional damping is presented (C_{L_1}), in the red traced line the second proposed curve (C_{L_2}) and in the black dotted line the polynomial damping model (C_{L_3}). Figure 5.11b depicts the rotating speed at the bit and, through it, it can be clearly seen that it rapidly converges to the applied speed, i.e.: no severe torsional vibration is observed. In Fig.5.11a the radial displacement in the last BHA section is shown through time. It can be noticed that whereas an overall behavior is maintained, minor effects can be seen in this case. The last model presents a secondary low frequency in its response and, at the same time, the lowest amplitude.

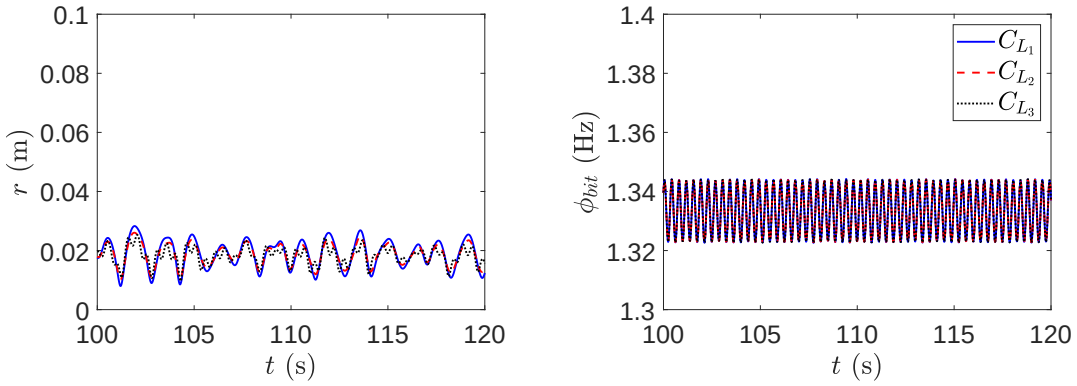

(a) (b)

Figure 5.11: Numerical simulations for the different damping models for $\Omega = 1.33$ Hz (80 rpm) and $W_{ob} = 100$ kN. In (a) the is the radial displacement of the geometric center in the middle of the last BHA section and in (b) the rotating speed at the bit.

In Fig. 5.12 a different drilling configuration is explored. In it, a W_{ob} of 220 kN is used and a rotation of 0.67 Hz is applied at the top. This simulation is presented in Fig. 5.12 in a diminished interval of time, which enables thorough observation. In Fig.5.12b, it can be seen that the rotational speed oscillates with high amplitudes. It goes to near stagnation to peaks of speed, configuring a severe case of torsional vibration. In Fig.5.12a the radial displacement in the same node as before is depicted. Even though the applied frequency is lower than the previous case, some difference can be observed in the dynamics. This is a consequence of the coupling between torsional and lateral dynamics, whereas the low frequency is applied at the top, lateral frequencies acting in the BHA are strictly dependent on the respective region rotating speed. In a similar fashion as before, the third damping model captured low-frequency vibrations.

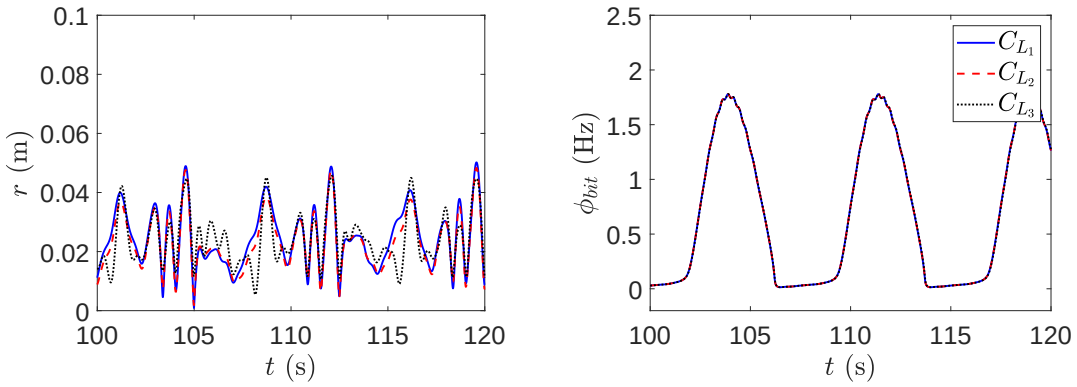

(a) (b)

Figure 5.12: Numerical simulations for the different damping models models for $\Omega = 0.67$ Hz (40 rpm) and $W_{ob} = 220$ kN.

In Fig. 5.13 a drilling configuration of $W_{ob} = 220$ kN and $\Omega = 1$ Hz (60 rpm) is

used. The radial displacement is shown in 5.13a. It can be noticed that, although qualitatively alike, each model presents its properties. Lateral displacements are mostly alike in the steady state. Figure 5.13b presents the torsional speed at the bit. It is possible to observe the effects of the lateral dynamics in the torsion of the drill-string and, even though the radial the displacements presented similar results, torsional speed is extremely different. Before the impact, this configuration presented a severe torsional vibration due to the bit-rock interaction and, after the impact, the dynamics changed considerably. The third model, that presents the overdamping of higher frequencies, seems to have a slight increase in the penetration of the borehole wall. Severe torsional vibrations lead to a high-frequency input in lateral dynamics which may ultimately lead to the impact and the backward whirl – another phenomena of higher frequency. At last, 5.13c presents the whirl frequency. This analysis confirms the backward whirl dynamics. From this frequency domain result, some of the damping properties can be observed. Whereas lower frequencies – both positive and negative – show similar amplitudes, the behavior of higher frequencies are strictly associated with the damping model. The third model is strictly contained within a low frequency range ($|\dot{\theta}| < 2$). The second model captures the widest range ($|\dot{\theta}| < 7.5$). Finally, the first model presents a in-between result ($|\dot{\theta}| < 4.5$).

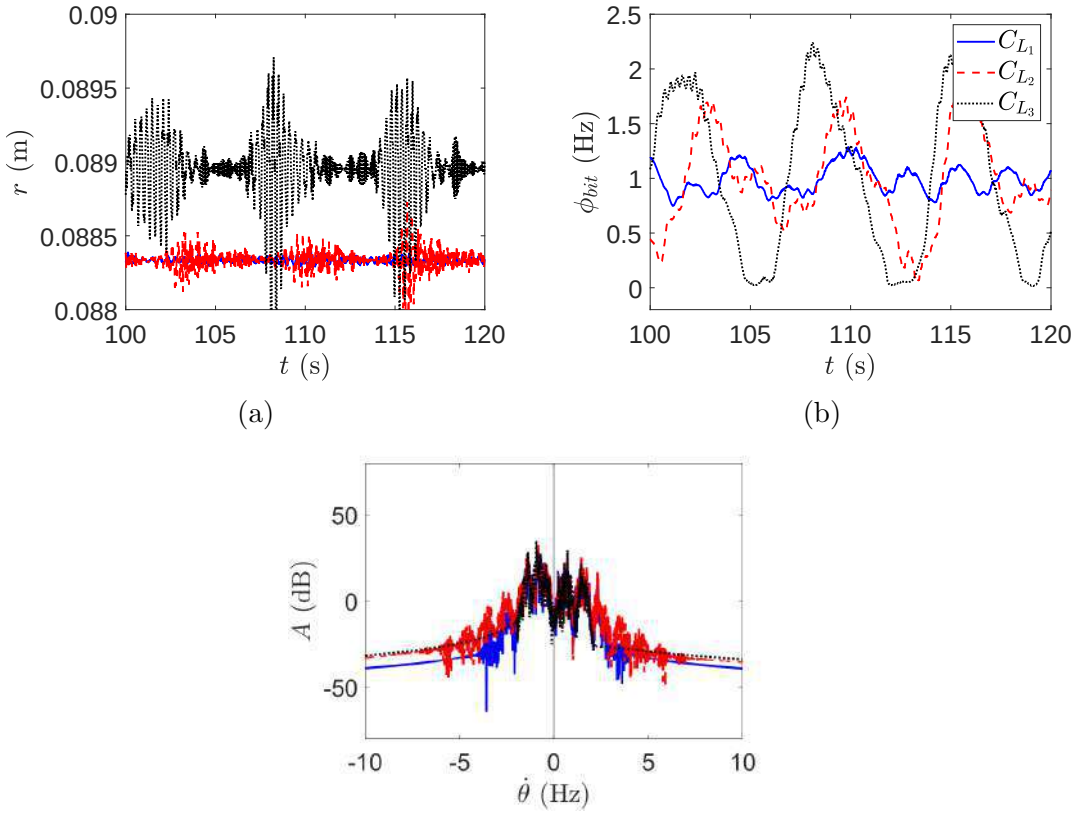

Figure 5.13: Numerical simulations for the different damping models for $\Omega = 1$ Hz (60 rpm) and $W_{ob} = 220$ kN. In: (a) the torsional speed at the top; (b) the radial displacement and in (c) the frequency analysis of a backward whirl configuration.

In summary, in the simulation with forward whirl, the damping model does not greatly affects the overall dynamics. When higher frequency excitation is introduced in the system by torsional vibrations, some difference can be observed, as higher frequencies are made more or less present depending on the model. When impact is present, the qualitative result might be equivalent, but its quantitative value diverges. As the nonlinear phenomena are made present in the dynamics, a wider range of frequencies are observed. Hence, the damping models effects are highlighted.

5.3.3 Dynamic maps

As each phenomena was successfully observed, the idea is to evaluate the existence of critical vibrations in different drilling configurations. For that, several simulations were executed in a wide range of both weight on bit (W_{ob}) and rotation applied at the top (Ω). For each damping model, two maps regarding the dynamics were generated: the former containing the torsional vibration severity index and the latter with the whirl frequency. Each point in the map corresponds to a simulation with the same initial conditions, i.e.: the initial conditions were reset in every run. In order to minimize the integration time, the modal reduction was applied. It made use of

the first five hundred modes, including the symmetrical lateral modes that were considered independently and the rigid body mode. More information regarding the modal reduction is provided in Appendix D.

In Fig. 5.14, the dynamic maps are presented, the former for torsional severity index (Fig. 5.14a) and the latter for whirl frequencies (Fig. 5.14b) with the first damping model. When analyzing Fig. 5.14a, it can be noticed a severe vibration zone that increases as higher weight on bits and lower rotating speeds are used – as it is usually seen in the literature. Outside that region, it is clear that most of the indices calculated are small, configuring a low vibration zone. However, some points of the map present torsional vibrations – severe or not. Those are mainly due to lateral impact between the drill-string and the borehole wall. These impact torques lead to torsional vibrations, some even of high intensity. Next, the whirl frequencies are analyzed. When there are severe torsional vibrations due to the bit-rock interaction, there might be impact, i.e.: torsional vibrations may lead to impact and backward whirl. Most of the impact regions are associated with some resonance frequency. Near those frequencies, the drill-string collides with the borehole wall. As the weight on bit changes, the static coupling leads to changes in the lateral eigenfrequencies and hence, these 'resonance lines' show a slight slope. Different backward whirl frequencies can be seen when the same rotation is applied at the top. This can be a consequence of the region where is either impact or a sliding motion are present. When there is pure rolling, the backward whirl frequency is given by a geometric relation:

$$\dot{\theta}_{bw} = -\Omega \frac{R_o}{r_c}. \tag{5.4}$$

Hence, it can be seen that when there is pure rolling, the whirl frequency depends on the applied rotation and ratio between the section's radius and the clearance. Then, even if the applied rotation is the same, impact in different regions leads to distinct backward whirl frequencies. When the forward whirl is regarded, the whirl frequency is the same as the frequency of the rotation applied, commonly seen in rotordynamics as synchronous whirl.

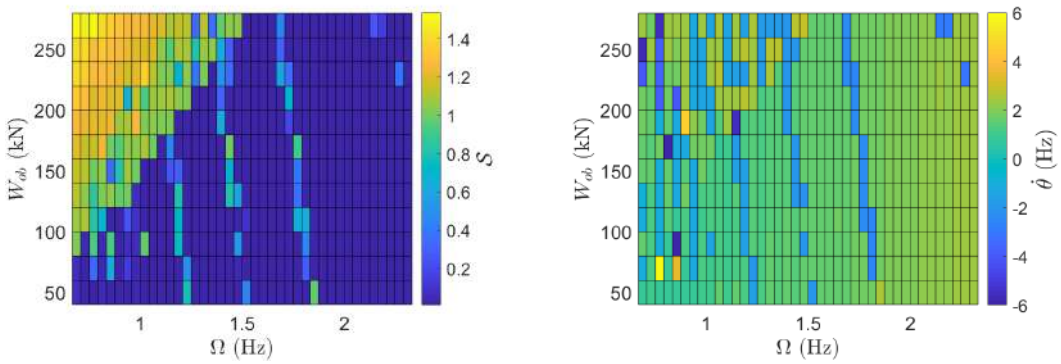

(a) (b)

Figure 5.14: Dynamic maps for the deterministic reduced order model with the first five hundred modes with the first damping model (Rayleigh proportional model). In (a), the torsional severity index and in (b) the whirl frequency.

The same analyses is conducted with the second damping model and is presented in Fig. 5.15. As expected, there is a an increase in the occurrence of severe lateral vibrations in higher frequencies. As seen before, the presence of both torsional and lateral vibrations are closely related and the effects of a lower damping can be seen clearly in both dynamic maps.

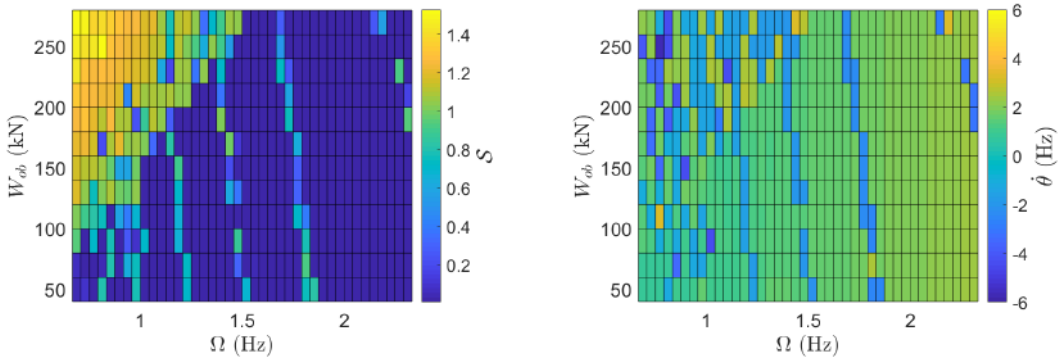

(a) (b)

Figure 5.15: Dynamic maps for the deterministic reduced order model with the first five hundred modes with the second damping model (adapted Rayleigh proportional model). In (a), the torsional severity index and in (b) the whirl frequency.

From Fig. 5.16, it can be seen that the third damping model shows severe vibrations restricted to a low frequency range. This is mainly due to the fact that whereas this model considered exact values to the known points, values outside of the defined ones are not as well defined and, in this case, lead to the overdamping of higher frequencies. Hence, while the severe torsional vibration zone is still well defined, there are few regions with torsional vibrations due to impact.

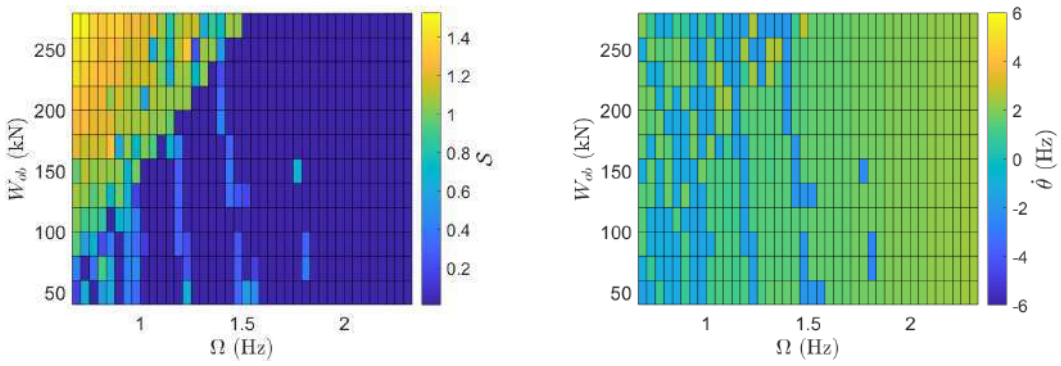

(a) (b)

Figure 5.16: Dynamic maps for the deterministic reduced order model with the first five hundred modes with the third damping model (generalized Rayleigh proportional model). In (a), the torsional severity index and in (b) the whirl frequency.

Finally, while the overall behavior was seen in every dynamic map, the effects of different damping models are clear. High damping in higher frequencies reduces the region of backward whirl significantly.

5.4 Stochastic response

In this section, the stochastic response is presented. It starts with a dispersion analysis in the main diagonal of the damping matrix in the modal base, followed by frequency domain results and, finally, stochastic maps, where the probability of occurrence of a critical phenomena is determined. For every analysis shown here, the Monte Carlo Method was used in addition to the quadratic mean convergence criteria with the radial displacement. Each stochastic analysis is originated by globally disturbing one of the three deterministic (proportional) damping matrices in the reduced order model (see Appendix D for details regarding the reduced order model).

5.4.1 Dispersion analysis

As previously presented in Chapter 3 Section 4.2, the random matrix model depends on two main constants, the system's size and the dispersion parameter. While the former is defined by either the mesh or the reduction applied, the latter, in this work, is defined by analyzing its effects on the main diagonal of the stochastic damping matrix on the modal base. With this, it is possible to observe how it is affecting the physics of the model.

From the deterministic model, the random damping model is originated from the damping matrix in the modal base. For the stochastic damping matrix, an approximation of the damping ratio was extracted from the main diagonal of the

matrix in the modal base:

$$\xi_i = \frac{\boldsymbol{C}_{ii}^{(m)}}{2\omega_{n_i}}, \tag{5.5}$$

where $\boldsymbol{C}_{ii}^{(m)}$ is the value of the damping for the i_{th} mode, ω_{n_i} is the i_{th} natural frequency and ξ_i the respective damping ratio. Naturally, these values are expected to follow any relations of $\xi(\omega)$ defined.

To evaluate the dispersion, the terms of the main diagonal of the stochastic matrix were compared with the expected value with distinct values of δ. In the sequence, the maximum relative error for each damping ration is calculated:

$$\xi_{err_{ik}} = \frac{|\xi_{det_i} - \xi_{rnd_{ik}}|}{\xi_{det_i}}, \tag{5.6}$$

where $\xi_{err_{ik}}$ is the error in the damping ratio of the i^{th} mode for the k^{th} Monte Carlo simulation. ξ_{det_i} is the deterministic damping ratio and $\xi_{rnd_{ik}}$ the stochastic damping ratio approximation (of the e k^{th} Monte Carlo simulation). Finally, the greatest value of $\xi_{err_{ik}}$ for each mode was extracted and used as reference.

In Fig. 5.17, the relative error for each one of the damping models is presented for a $W_{ob} = 220$ kN and dispersion parameters of $\delta = 0.1$,$\delta = 0.3$ and $\delta = 0.5$. From Fig. 5.17a to 5.17c, it can be observed that the relative error for a particular dispersion parameter is confined in-between well defined regions. In other words, for a dispersion of $\delta = 0.1$, the absolute error is lesser then 5%, for $\delta = 0.3$, it is roughly defined from $5 - 10\%$, and for for $\delta = 0.5$, from $10 - 20\%$.

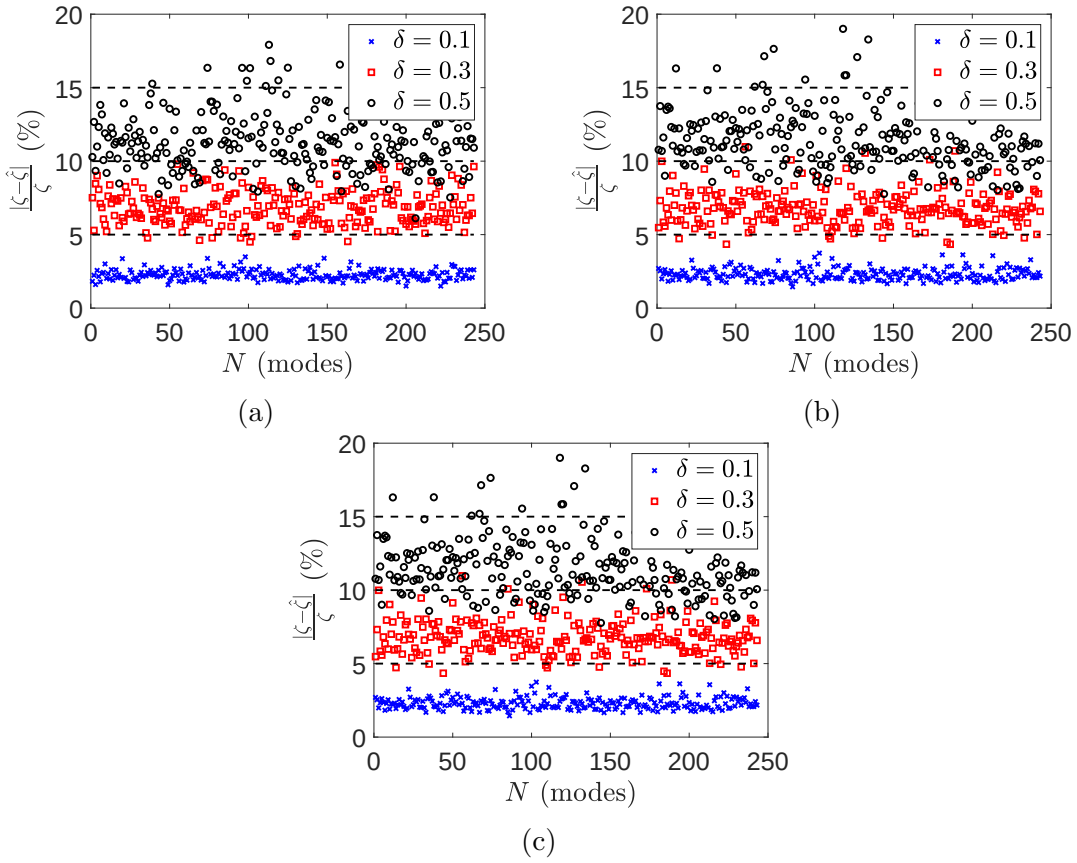

Figure 5.17: Maximum relative errors in the damping ratio for each used mode for a $W_{ob} = 220$ kN and different dispersion parameters. In (a), the error is calculated using the first damping model; in (b) the second damping model and in (c) the third damping model.

To facilitate the comprehension of the previous analysis, Fig. 5.18 presents the values of $\xi_{rnd_{ij}}$ obtained though 50 Monte Carlo simulations for a $W_{ob} = 220$ kN. It can observed how the increase of the dispersion values impact the damping ratios without disrupting the tendency provided by the damping ratio relations.

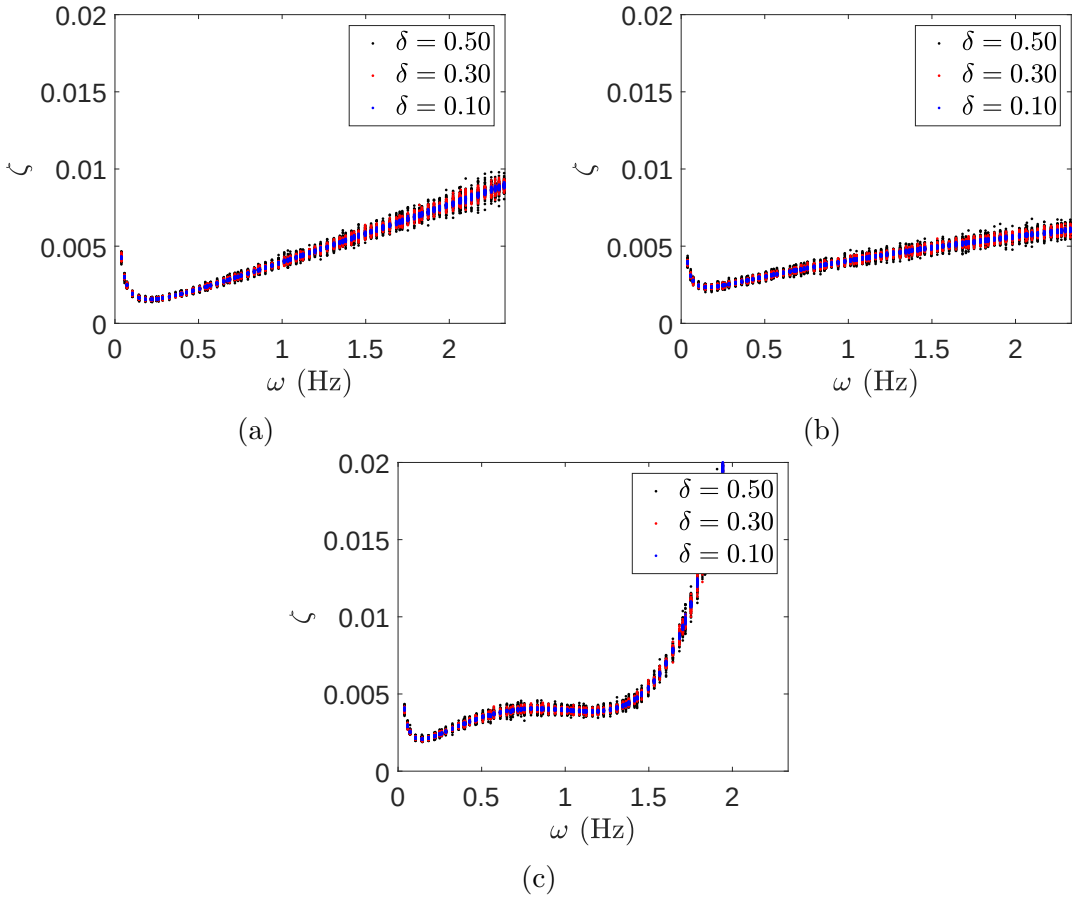

Figure 5.18: Damping ratio calculated from the main diagonal of the random damping matrices with a $W_{ob} = 220$ kN. In (a), the error is calculated using the first damping model; in (b) the second damping model and in (c) the third damping model.

When comparing both Fig. 5.17 and 5.18, it can be seen that, while the latter is intuitive, the former contains relevant information regarding the disruption of the deterministic models provided.

5.4.2 Frequency domain analysis

In this section, the stochastic model is explored in the frequency domain. At first, it is studied considering only the main diagonal of the stochastic damping matrix. In the sequence, a decoupling technique presented in [6] is applied for this analysis. The objective is to observe the impact of off-diagonal terms in the frequency response function.

For this analysis, only the lateral degrees of freedom were observed. Due to the system's symmetry, this procedure is reduced to one single plane, either XY or XZ. Also, as no torsion was regarded, the unbalance force at a constant rotating speed becomes linear (Eq. 3.41). Finally, as the main objective is to understand the effects of off-diagonal terms, no impact was considered.

To obtain a decoupled model, the strategy developed in [6] is adopted. Given a generic linear system in the modal base, it can be expressed as:

$$\ddot{\boldsymbol{\eta}} + \mathcal{C}\dot{\boldsymbol{\eta}} + \boldsymbol{\Lambda}\boldsymbol{\eta} = \boldsymbol{\mathcal{F}}, \tag{5.7}$$

where η are the system's coordinates in the modal base, $\mathcal{C}$ the damping matrix in the modal base, $\boldsymbol{\Lambda}$ a diagonal matrix containing the square of the eigenfrequencies and $\boldsymbol{\mathcal{F}}$ a force vector. It can also be expressed as:

$$\ddot{\eta}_i + \sum_{j=1}^{m} \mathcal{C}_{ij}\dot{\eta}_j + \omega_{n_i}^2 \eta = \mathcal{F}_i, \;\; i = 1, 2, ..., m. \tag{5.8}$$

When the Fourier transform is applied, the system becomes:

$$-\omega^2\tilde{\eta}_i + \omega j \sum_{j=1}^{m} \mathcal{C}_{ij}\tilde{\eta}_j + \omega_{n_i}^2 \tilde{\eta} = \tilde{\mathcal{F}}_i, \tag{5.9}$$

the diagonal damping term can be separated:

$$-\omega^2\tilde{\eta}_i + \omega j(\mathcal{C}_{ii}\tilde{\eta}_i + \sum_{j\neq i}^{m} \mathcal{C}_{ij}\tilde{\eta}_j) + \omega_{n_i}^2 \tilde{\eta} = \tilde{\mathcal{F}}_i, \tag{5.10}$$

in sequence:

$$(-\omega^2 + \omega j\mathcal{C}_{ii} + \omega j \sum_{j\neq i}^{m} \mathcal{C}_{ij}\frac{\tilde{\eta}_j}{\tilde{\eta}_i} + \omega_{n_i}^2)\tilde{\eta}_i = \tilde{\mathcal{F}}_i. \tag{5.11}$$

The main hypothesis in this technique is that [6]:

$$\frac{\tilde{\eta}_j}{\tilde{\eta}_i} \approx \frac{h_i(\omega)}{h_j(\omega)}, \tag{5.12}$$

where $h_i(\omega)$ is the transfer function that corresponds to the i^{th} eigenfrequency when off-diagonal terms in the damping matrix in the modal base are disregarded. With this methodology, there is no need to solve the eigenvalue problem for an expanded system in the state-space for each random matrix, which grants efficiency to the process.

In Fig. 5.19, the threshold of the stochastic frequency response is presented for the first damping model in the middle of the last BHA section. In black there are the maximum and minimum values for the damping with only the main diagonal ('Prop'), in blue there are the maximum and minimum for the damping with off-diagonal terms ('Non-prop'). Each figure is a result for a different dispersion parameter – $\delta = 0.10$,$\delta = 0.30$ and $\delta = 0.50$. In general, none of the three values for δ affected significantly the dynamics, even though the maximum damping ratio error

reached expressive values for the $\delta = 0.50$. A small gap is only seen for the higher dispersion and when the frequency is close to 2 Hz.

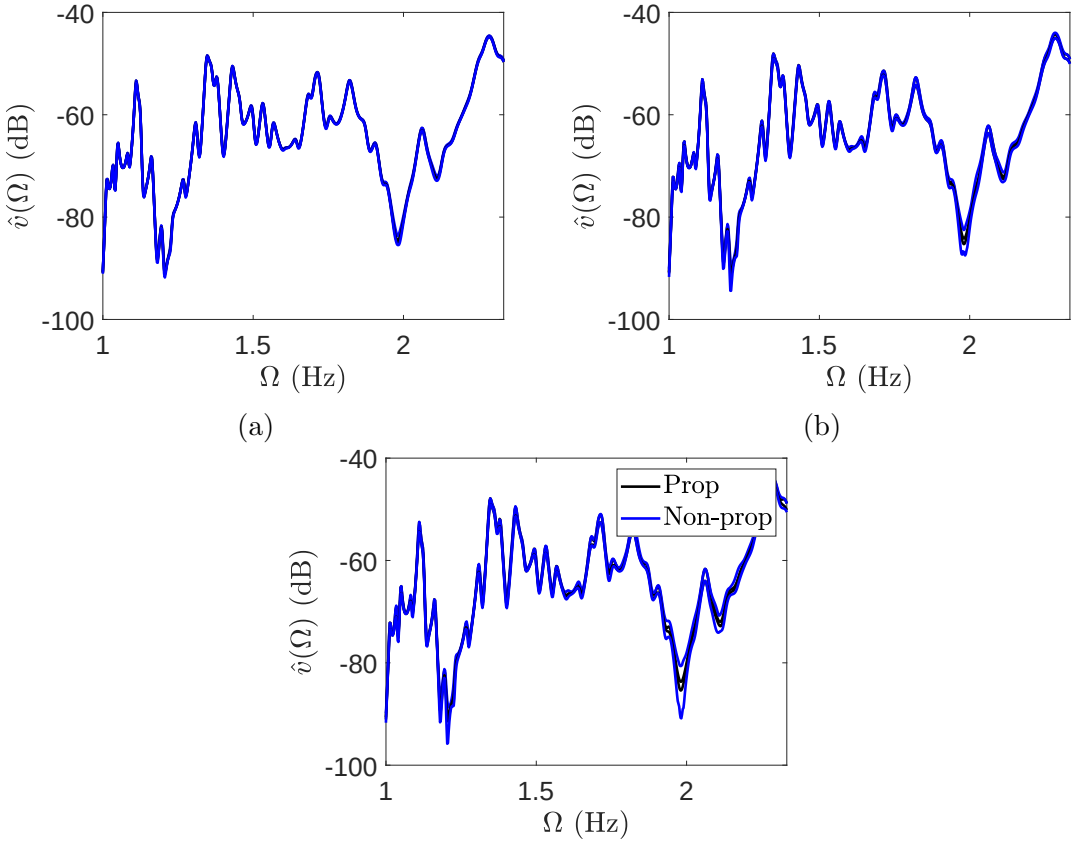

Figure 5.19: Frequency domain response for the first stochastic damping model with three different values for dispersion: (a) $\delta = 0.10$, (b) $\delta = 0.30$ and (c) $\delta = 0.50$.

In Fig. 5.20, the behavior previously observed is repeated. It can be seen that neither the increase in the dispersion nor the off-diagonal terms affected the overall frequency response for frequency interval analyzed.

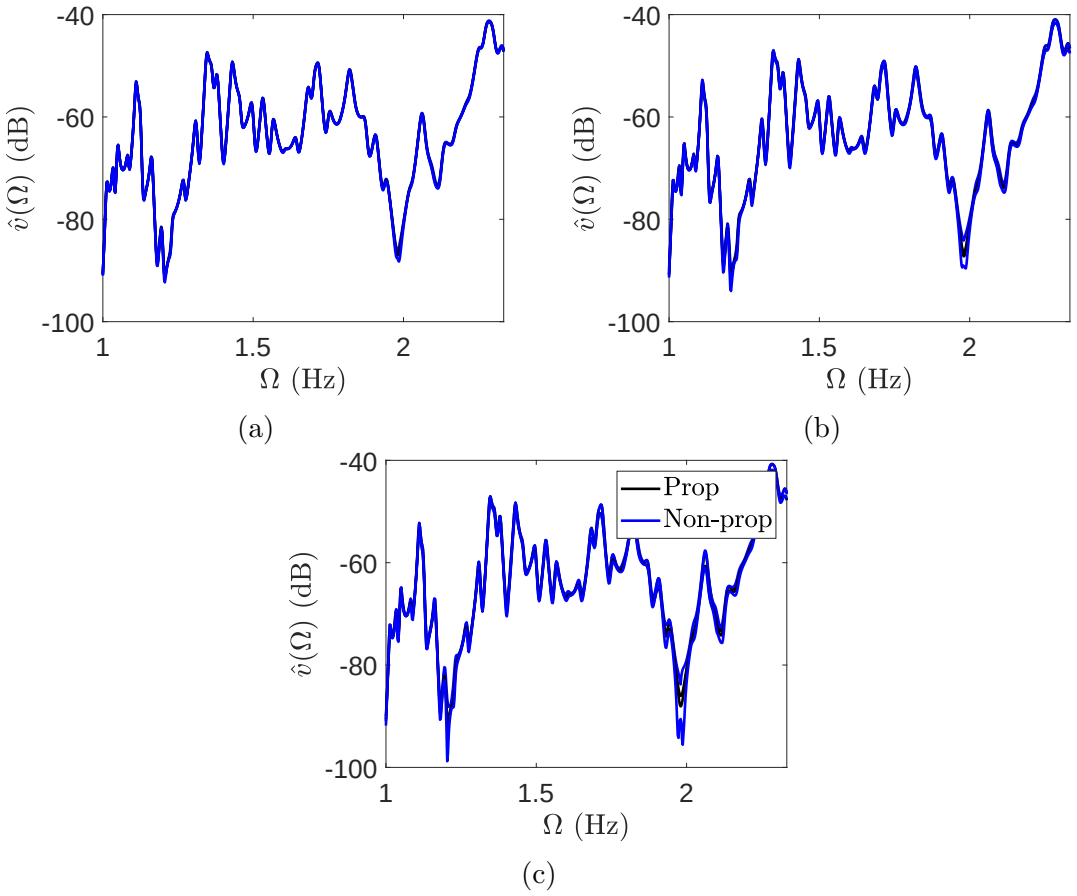

Figure 5.20: Frequency domain response for the second stochastic damping model with three different values for dispersion: (a) $\delta = 0.10$, (b) $\delta = 0.30$ and (c) $\delta = 0.50$.

Finally, in Fig. 5.21, the last damping model is presented. In it, it can be observed that near the end of the frequency interval depicted, there is a region sensible to the uncertainties of the model. While this effect can be seen in the frequency response with only the damping main diagonal, the off-diagonal terms present a visible increase in the band width. This behavior is a consequence of the the amplitude in magnitude of the terms contained in the damping matrix.

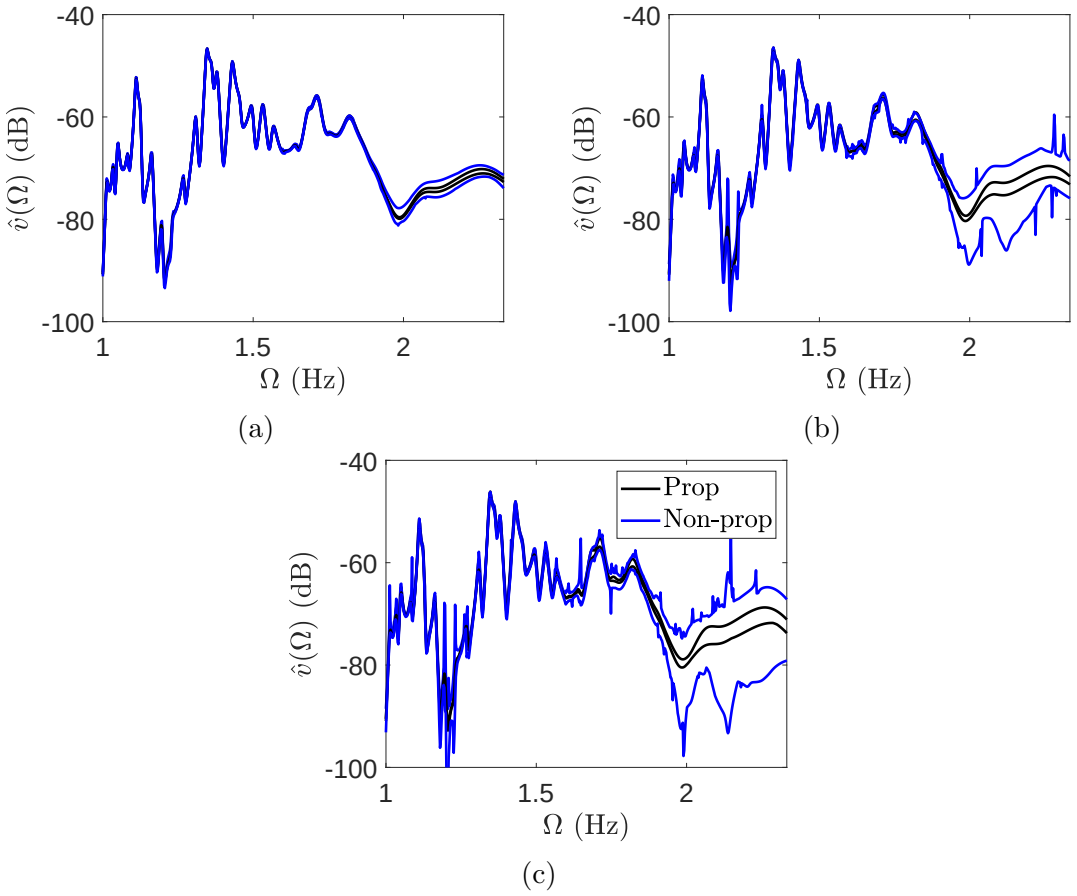

Figure 5.21: Frequency domain response for the second stochastic damping model with three different values for dispersion: (a) $\delta = 0.10$, (b) $\delta = 0.30$ and (c) $\delta = 0.50$.

5.4.3 Probability maps

In this section, the stochastic model is used to generate several probability maps. Similar to the deterministic dynamic map, it explores different values for both Ω and W_{ob} and, for each simulation, the initial conditions are reset. In this case, however, a point in the map is obtained through severe simulations and, in each case, the occurrence of severe torsional vibration and backward whirl is registered. With it, the probability of each phenomena is calculated. As previously stated, these maps are achieved from the reduced order model with the first five hundred modes. Based on the errors values calculated from the damping ratios, $\delta = 0.30$ was used for each map simulation.

In Fig. 5.22, the probability maps for first stochastic damping model is presented. Figure 5.22a shows the probability of several torsional vibrations ($\mathcal{S} > 0.8$). It can be noticed two well defined zones, the former always with severe torsional vibrations and other always without. Yet, the impact of a stochastic damping model is clear. Regions close to lateral natural frequencies presented a small chance of severe torsional vibrations. As lower frequencies are used, the greater is the proba-

bility of torsional vibrations due to lateral impact. However, as higher W_{ob} are used, it can be seen that lateral impact can reduce the probability of torsional vibrations. In Fig. 5.22b, it can be seen that close to a resonance frequency, there is backward whirl. As a lower rotation is applied – and the drilling configuration nears a severe torsional vibration region – the probability of backward whirl decreases.

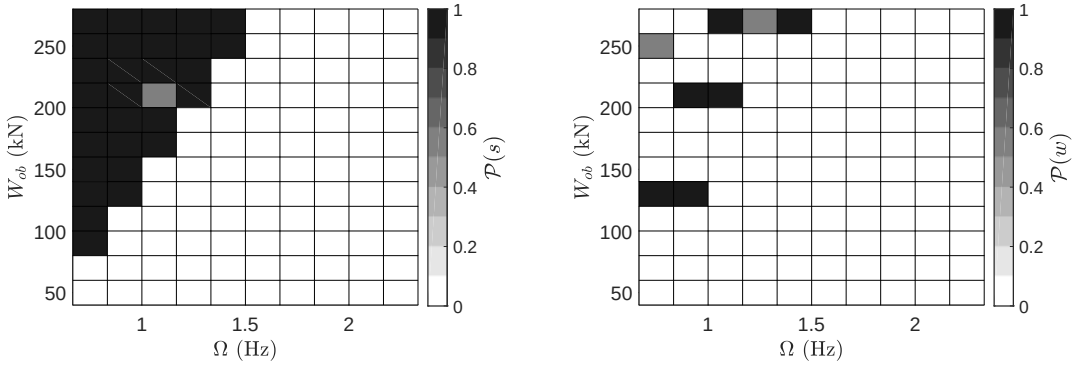

(a) (b)

Figure 5.22: Probability maps for the stochastic model with the first stochastic damping model (generalized Rayleigh proportional model). In (a), the torsional vibration probability and in (b) the backward whirl probability.

In Fig. 5.23, the probability maps for the second stochastic damping model is presented. Every effect seen in the first map is observed in a larger scale in these maps. As observed in Chapter 3 Section 4.1, the second deterministic model presents a slightly greater damping for lower frequencies and lower damping for higher ones (when compared to the Rayleigh proportional damping). However, close to the lower frequencies, the stochastic model presented a higher probability of severe torsional vibrations due to contact. This is a consequence of both severe torsional vibrations (due to the bit-rock interaction) and backward whirl, which enables high excitation frequencies for the lateral model.

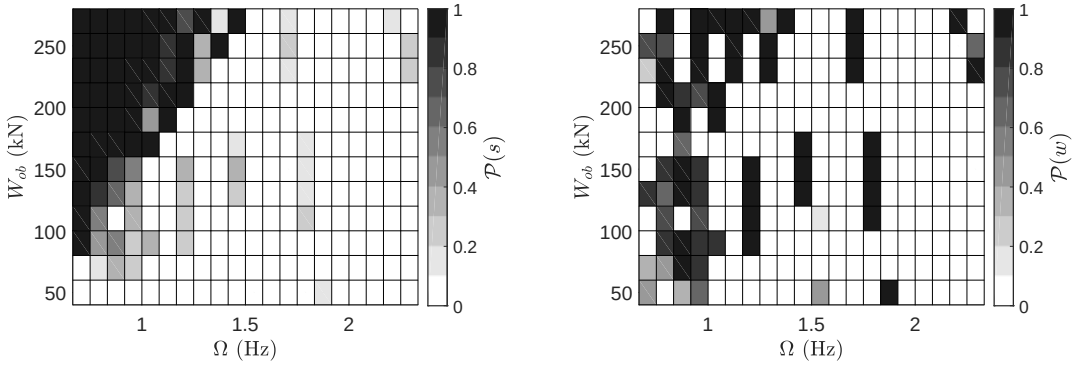

(a) (b)

Figure 5.23: Probability maps for the stochastic model with the second damping model (adapted Rayleigh proportional model). In (a), the torsional severity index and in (b) the whirl frequency.

Finally, the last damping model is observed in Fig. 5.24. As previously, it presents a high-probability zone for severe torsional vibrations that is closely related with the incidence of backward whirl. In Fig. 5.24a, in contrast with the previous ones, shows small incidence of severe torsional vibrations due to contact – even though there is a great probability of backward whirl, as those high frequencies are less prominent in the overall dynamics. When the backward whirl probability map is observed in Fig. 5.24b, it is clear that the incidence of this phenomena is not as present in higher frequencies, just as expected by the deterministic analysis. However, the probability seems slightly higher for lower frequencies.

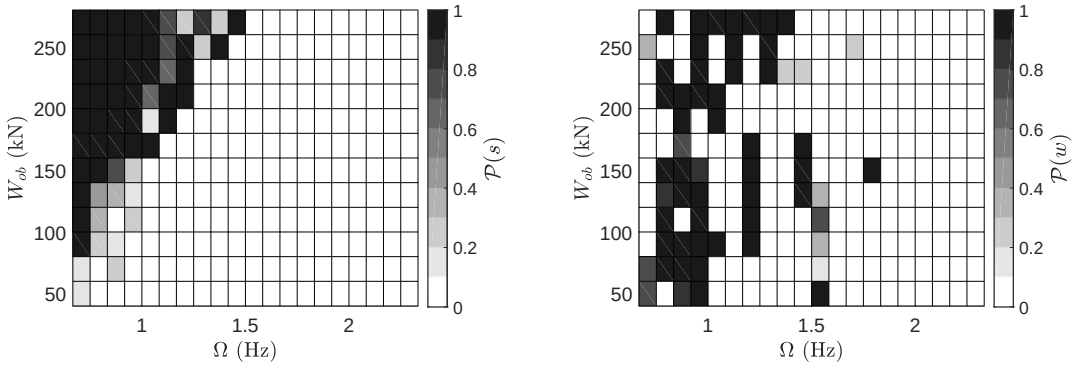

(a) (b)

Figure 5.24: Probability maps for the stochastic model with the third damping model (generalized Rayleigh proportional model). In (a), the torsional severity index and in (b) the whirl frequency.

From these maps, it is made clear how the damping model affects severe lateral vibrations, specially considering when higher frequencies are overdamped. Another conclusion, is that the presence of higher frequencies in lateral vibrations is likely to increase the occurrence of severe torsional vibrations in lower speeds, due to the coupling between lateral-torsional dynamics and the existence of a high-frequency phenomenon (the backward whirl).

Chapter 6

Summary and concluding remarks

This work started with a brief introduction which presented the drill-string and the harmful types of vibrations, highlighting those that are explored here. In the sequence, a literature review is conducted with several works, where different models and approaches were explored for distinct purposes. Even though this literature review focused on drill-strings torsional and lateral vibrations, literature regarding rotordynamics, the Finite Element Method, stochastic modelling and damping strategies were of utmost relevance for this work.

The literature review was followed by the model's development. At this point, the main hypotheses of the model were presented and fundamental equations of kinematics, constitutive and energy relations were explored, which enabled the Hamilton's principle to be applied, leading to a set of differential equations in their variational form. This formulation was solved in the space using the Finite Element Method, providing a discretization of the geometry in the form of a system of nonlinear differential equations in time. Boundary conditions and external forces were presented, the former considered that no lateral displacements were possible at both extremities in the drill-strings and that a constant rotation is applied at the top. The latter took into account a smooth bit-rock interaction model, a discontinuous linear-elastic impact force, a smooth Coulomb friction force, a resulting torque from impact dynamics and linear-elastic stabilizers.

The next step was the development of deterministic damping models. Three distinct models for lateral proportional damping were provided and calibrated from experimental data found in the literature regarding a beam pinned in both ends [16]. The first model consisted in the Rayleigh proportional damping. The second was developed through the methodology developed in [1] and had the objective of minimizing the overdamping in higher frequencies of the system. The third, even though achieved by the methodology provided in [1], follows a generalization of the Rayleigh proportional damping developed in [12]. This last model presented higher damping ratios for higher frequencies which might be justified by the fluid

interaction. This approach, however, proved to be problematic. Not only positive damping ratios throughout the whole spectrum of frequencies were needed to obtain a positive definite damping matrix, but also numerical errors were often associated when high values of exponents for the inverse of the mass matrix were used.

With the deterministic damping models, other three stochastic damping models were provided. These aimed to account for the uncertainties of the modeling itself and for the effects of non-proportional terms, such as fluid interaction. Each model was based on one of the deterministic, where the deterministic damping matrix in modal base would be globally disturbed by a random germ, providing a random non-diagonal matrix.

The last step in the modelling development, was to provide a reduced order model based on the modal truncating method. This not only considered the modes obtained by the eigenvalue/eigenvector problem but also the rigid body mode for the torsional degrees of freedom.

With the model developed and presented, the results section started with the drill-string's mechanical properties and a mesh convergence analysis. In the sequence, a model simplification is studied where some geometric nonlinearities were disregarded. It was observed that the main difference was in the quantitative results during impact. However, for qualitative analysis, both models could be equivalent. With the simplified model, a set of analyses was conducted. At first, different tools for evaluating the dynamics were provided and exemplified. With these tools, the different damping models were studied in different configuration and explored, culminating in dynamic maps, where the occurrence of both severe torsional and lateral vibrations were identified. Most of the backward whirl occurred near a resonance frequency, which is in accordance with the expected ([79]). This also provided lateral-induced torsional vibration, as well as torsional-induced backward whirl.

The last set of results concerned the stochastic models. Through them, several analyses were conducted to evaluate how different dispersions could affect the system. Finally, probability maps were created with the Monte Carlo Method and the reduced order model to evaluate the chance of occurrence of severe vibrations. As seen before, severe lateral vibrations often occurred near resonance. It is also observed that, not only lateral impact may cause severe torsional vibrations, as it can reduce its probability. Another important relation, is that the effects of higher frequencies were made clear – specially when low rotations are applied to the drill-string. The presence of high lateral frequencies was a source of severe torsional vibrations.

Bibliography

[1] Adhikari, S. (2000). *Damping Models for Structural Vibration*. PhD thesis, Cambridge University.

[2] Adhikari, S. (2004). Optimal complex modes and an index of damping non-proportionality. *Mechanical Systems and Signal Processing*, 18(1):1–27.

[3] Al-Hiddabi, SA e Samanta, B. e. S. A. (2003). Non-linear control of torsional and bending vibrations of oilwell drillstrings. *Journal of sound and vibration*, 265(2):401–415.

[4] Allen, M. B. (1987). BHA lateral vibrations: Case studies and evaluation of important parameters. *SPE/IADC Drilling Conference, Proceedings*, 1987-March:531–535.

[5] Ambrus, A., Skadsem, H. J., and Mihai, R. G. (2018). Similarity analysis for downscaling a full size drill string to a laboratory scale test drilling rig. In *ASME 2018 37th International Conference on Ocean, Offshore and Arctic Engineering*, pages V008T11A005–V008T11A005. American Society of Mechanical Engineers.

[6] Bellos, J. and Inman, D. J. (1990). Frequency response of nonproportionally damped, lumped parameter, linear dynamic systems. *Journal of Vibration and Acoustics, Transactions of the ASME*, 112(2):194–201.

[7] Besselink, B., Tabak, U., Lutowska, A., Van De Wouw, N., Nijmeijer, H., Rixen, D. J., Hochstenbach, M. E., and Schilders, W. H. (2013). A comparison of model reduction techniques from structural dynamics, numerical mathematics and systems and control. *Journal of Sound and Vibration*, 332(19):4403–4422.

[8] Besselink, B., Van De Wouw, N., and Nijmeijer, H. (2011). A semi-analytical study of stick-slip oscillations in drilling systems. *Journal of Computational and Nonlinear Dynamics*, 6(2):1–9.

[9] Bogdanoff, J. L. and Goldberg, J. E. (1961). A New Analytical Approach to Drill Pipe Breakage II. *ASME. J. Eng. Ind.*, 83(2):101–106.

[10] Burgess, T. M., McDaniel, G. L., and Das, P. K. (1987). Improving BHA tool reliability with drillstring vibration models: Field experience and limitations. *SPE/IADC Drilling Conference, Proceedings*, 1987-March:517–530.

[11] Canor, T., Blaise, N., and Denoël, V. (2012). Efficient uncoupled stochastic analysis with non-proportional damping. *Journal of Sound and Vibration*, 331(24):5283–5291.

[12] Caughey, T. and O'Kelly, M. E. (1965). Classical normal modes in damped linear dynamic systems.

[13] Christoforou, AP e Yigit, A. (2003). Fully coupled vibrations of actively controlled drillstrings. *Journal of sound and vibration*, 267(5):1029–1045.

[14] Christoforou, A. P. and Yigit, A. S. (1997). Dynamic Modelling of Rotating Drillstrings With Borehole Interactions. *Journal of Sound and Vibration*, 206(2):243–260.

[15] Christoforou, A. P. and Yigit, A. S. (2003). Fully coupled vibrations of actively controlled drillstrings. *Journal of Sound and Vibration*, 267(5):1029–1045.

[16] de Souza, M. L. M. (2017). *Ajuste de modelo computacional na dinâmica de estruturas*. PhD thesis, Federal University of Rio de Janeiro.

[17] Deily, F., Dareing, D., Paff, G., Ortloff, J., and Lynn, R. (1968). Downhole Measurements of Drill String Forces and Motions. *ASME. J. Eng. Ind.*, 90(2):217–225.

[18] Denoël, V. and Degée, H. (2009). Asymptotic expansion of slightly coupled modal dynamic transfer functions. *Journal of Sound and Vibration*, 328(1-2):1–8.

[19] Detournay, E. and Defourny, P. (1992). A phenomenological model for the drilling action of drag bits. In *International journal of rock mechanics and mining sciences & geomechanics abstracts*, volume 29, pages 13–23. Elsevier.

[20] Dufeyte, M.-P. and Henneuse, H. (1991). Detection and Monitoring of the Slip-Stick Motion: Field Experiments. *Proceedings of SPE/IADC Drilling Conference*, pages 429–438.

[21] Dykstra, M. W., Chen, D. C.-K., Warren, T. M., and Zannoni, S. A. (1994). Experimental Evaluations of Drill Bit and Drill String Dynamics. *Annual Technical Conference and Exhibition of the Society of Petroleum Engineers*, (SPE 28323):319–334.

[22] Finnie, I. and Bailey, J. (1960). An Experimental Study of Drill-String Vibration. *ASME. J. Eng. Ind.*, 82(2):129–135.

[23] Fritz, R. J. (1970). The Effects of an Annular Fluid on the Vibrations of a Long Rotor, Part 1 -Theory. *Journal of Basic Engineering*, 92(4):923–929.

[24] Genta, G. and Amati, N. (2010). Hysteretic damping in rotordynamics: An equivalent formulation. *Journal of Sound and Vibration*, 329(22):4772–4784.

[25] Germay, C., Denoël, V., and Detournay, E. (2009). Multiple mode analysis of the self-excited vibrations of rotary drilling systems. *Journal of Sound and Vibration*, 325(1-2):362–381.

[26] Gulyaev, V. I., Lugovoi, P. Z., Belova, M. A., and Solov'Ev, I. L. (2006). Stability of the equilibrium of rotating drillstrings. *International Applied Mechanics*, 42(6):692–698.

[27] Halsey, G., Kyllingstad, A., Aarrestad, T. V., and Lysne, D. (1986). Drillstring Vibrations: Comparison Between Theory and Experiments on a Full-Scale Research Drilling Rig. *IADC/SPE Drilling Conference*, (IADC/SPE 14760):311–321.

[28] Halsey, G., Kyllingstad, A., and Kylling, A. (1988). Torque Feedback Used to Cure Slip-Stick Motion. In *SPE Drilling Conference*. Society of Petroleum Engineers - SPE 18049.

[29] Hong, L., Girsang, I. P., and Dhupia, J. S. Identification and control of stick-slip vibrations using Kalman estimator in oil-well drill strings. *Journal of Petroleum Science and Engineering*, pages 119–127.

[30] Ibrahimbegovic, A. and Wilson, E. L. (1989). Simple numerical algorithms for the mode superposition analysis of linear structural systems with non-proportional damping. *Computers and Structures*, 33(2):523–531.

[31] Jansen, J. (1991). Non-linear rotor dynamics as applied to oilwell drillstring vibrations. *Journal of sound and vibration*, 147(1):115–135.

[32] Jansen, J. D. and van den Steen, L. (1995). Active damping of self-excited torsional vibrations in oil well drillstrings. *Journal of Sound and Vibration*, 179(4):647–668.

[33] Kapitaniak, M., Vaziri, V., Páez Chávez, J., and Wiercigroch, M. Experimental studies of forward and backward whirls of drill-string. *Mechanical Systems and Signal Processing*, pages 454–465.

[34] Kapitaniak, M., Vaziri, V., Paéz Chávez, J., and Wiercigroch, M. (2017). Numerical Study of Forward and Backward Whirling of Drill-String. *Journal of Computational and Nonlinear Dynamics*, 12(6):1–7.

[35] Kapitaniak, M., Vaziri Hamaneh, V., Chávez, J. P., Nandakumar, K., and Wiercigroch, M. (2015). Unveiling complexity of drill-string vibrations: Experiments and modelling. *International Journal of Mechanical Sciences*, 101-102:324–337.

[36] Karnopp, D. (1985). Computer simulation of stick-slip friction in mechanical dynamic systems. *Journal of dynamic systems, measurement, and control*, 107(1):100–103.

[37] Khulief, Y. A. and Al-Naser, H. (2005). Finite element dynamic analysis of drillstrings. *Finite Elements in Analysis and Design*, 41(13):1270–1288.

[38] Khulief, Y. A. and Al-Sulaiman, F. A. (2009). Laboratory investigation of drill-string vibrations. *Proceedings of the Institution of Mechanical Engineers, Part C: Journal of Mechanical Engineering Science*, 223(10):2249–2262.

[39] Khulief, Y. A., Al-Sulaiman, F. A., and Bashmal, S. (2007). Vibration analysis of drillstrings with self-excited stick-slip oscillations. *Journal of Sound and Vibration*, 299(3):540–558.

[40] Kyllingstad, Å. and Halsey, G. W. (1988). A Study of Slip/Stick Motion of the Bit. *SPE Drilling Engineering*, 3(4):369–373.

[41] Leine, R. I. and Van Campen, D. H. (2002). Stick-slip whirl interaction in drillstring dynamics. *Journal of Vibration and Acoustics*, 122(April):287–296.

[42] Liao, C.-m., Balachandran, B., Karkoub, M., and Abdel-Magid, Y. L. (2011). Drill-String Dynamics: Reduced-Order Models and Experimental Studies. *Journal of Vibration and Acoustics*, 133(4):041008.

[43] Lin, Y. K. (1964). Classical normal modes in damped linear dynamic systems. *Journal of Applied Mechanics, Transactions ASME*, 33(2):471–472.

[44] Lin, Y.-Q. and Wang, Y.-H. (1991). Stick-Slip Vibrations of Drill Strings. *ASME J. Eng. for Industry*, 38(December 1989):38–43.

[45] Liu, X., Vlajic, N., Long, X., Meng, G., and Balachandran, B. (2013). Nonlinear motions of a flexible rotor with a drill bit: stick-slip and delay effects. *Nonlinear Dynamics*, 72(1-2):61–77.

[46] Liu, Y. and Gao, D. (2017). A nonlinear dynamic model for characterizing downhole motions of drill-string in a deviated well. *Journal of Natural Gas Science and Engineering*, 38:466–474.

[47] Lobo, D. M., Ritto, T. G., and Castello, D. A. (2017). Stochastic analysis of torsional drill-string vibrations considering the passage from a soft to a harder rock layer. *Journal of the Brazilian Society of Mechanical Sciences and Engineering*, 39(6):2341–2349.

[48] Melakhessou, H., Berlioz, A., and Ferraris, G. (2003). A Nonlinear Well-Drillstring Interaction Model. *Journal of Vibration and Acoustics*, 125(1):46.

[49] Minas, C. and Inman, D. J. (1991). Identification of a nonproportional damping matrix from incomplete modal information. *Journal of Vibration and Acoustics, Transactions of the ASME*, 113(2):219–224.

[50] Nandakumar, K. and Wiercigroch, M. (2013). Stability analysis of a state dependent delayed, coupled two DOF model of drill-stringvibration. *Journal of Sound and Vibration*, 332(10):2575–2592.

[51] Navarro-López, E. M. and Cortés, D. (2007). Sliding-mode control of a multi-DOF oilwell drillstring with stick-slip oscillations. *Proceedings of the American Control Conference*, pages 3837–3842.

[52] Navarro-López, E. M. and Suárez, R. (2004). Practical approach to modelling and controlling stick-slip oscillations in oilwell drillstrings. *Proceedings of the IEEE International Conference on Control Applications*, 2:1454–1460.

[53] Nelson, H. (1980). A finite rotating shaft element using timoshenko beam theory.

[54] Nelson, H. and McVaugh, J. (1976). The dynamics of rotor-bearing systems using finite elements. *Journal of Engineering for Industry*, 98(2):593–600.

[55] Neubauer, M., Ilja, G., and Jorg, W. (2015). Model and Method for a Time-Efficient Analysis of Lateral Drillstring Dynamics. In ASME GT2015,

editor, *ASME Turbo Expo 2015: Turbine Technical Conference and Exposition GT2015*, pages 1–13, Montréal.

[56] Nogueira, B. F. (2012). Robust Rotational Stability Analysis of a Vertical Drill-String. In ABCM, editor, *23rd International Congress of Mechanical Engineering*, number 1985, Rio de Janeiro. ABCM.

[57] Pastor, M., Binda, M., and Harčarik, T. (2012). Modal assurance criterion. *Procedia Engineering*, 48:543–548.

[58] Richard, T., Germay, C., and Detournay, E. (2004). Self-excited stick–slip oscillations of drill bits. *Comptes rendus MECANIQUE*, 332(8):619–626.

[59] Richard, T., Germay, C., and Detournay, E. (2007). A simplified model to explore the root cause of stick-slip vibrations in drilling systems with drag bits. *Journal of Sound and Vibration*, 305(3):432–456.

[60] Ritto, T., Soize, C., and Sampaio, R. (2010). Robust optimization of the rate of penetration of a drill-string using a stochastic nonlinear dynamical model. *Computational Mechanics*, 45(5).

[61] Ritto, T. G. (2010). *Numerical analysis of the nonlinear dynamics of a drill-string with uncertainty modeling.* Doctoral thesis, Université Paris-Est.

[62] Ritto, T. G. (2015). Bayesian approach to identify the bit–rock interaction parameters of a drill-string dynamical model. *Journal of the Brazilian Society of Mechanical Sciences and Engineering*, 37(4):1173–1182.

[63] Ritto, T. G., Aguiar, R. R., and Hbaieb, S. (2017). Validation of a drill string dynamical model and torsional stability. *Meccanica*, pages 1–9.

[64] Ritto, T. G. and Fabro, A. T. (2019). Investigation of random matrix applications on structural dynamics using a tensor decomposition. *Journal of the Brazilian Society of Mechanical Sciences and Engineering*, 41(8):1–11.

[65] Ritto, T. G. and Sampaio, R. (2013). Measuring the efficiency of vertical drill-strings: A vibration perspective. *Mechanics Research Communications*, 52:32–39.

[66] Ritto, T. G., Sampaio, R., and Soize, C. (2009). Drill-string nonlinear dynamics accounting for the drilling fluid. In *30o CILAMCE-Iberian-Latin-American Congress on Computational Methods in Engineering*, pages 1–25, Armação de Búzios, RJ, Brazil.

[67] Ritto, T. G., Soize, C., and Sampaio, R. Non-linear dynamics of a drill-string with uncertain model of the bit-rock interaction. *International Journal of Non-Linear Mechanics*, (8):865–876.

[68] Ruhl, R. L. and Booker, J. (1972). A finite element model for distributed parameter turborotor systems.

[69] Sampaio, R., Piovan, M. T., and Venero Lozano, G. (2007). Coupled axial/torsional vibrations of drill-strings by means of non-linear model. *Mechanics Research Communications*, 34(5-6):497–502.

[70] Shyu, R.-J. (1989). Bending Vibration of Rotating Drill Strings. pages 1–145.

[71] Soize, C. (2000). A Nonparametric Model of Random Uncertainties in Linear Structural Dynamics. *Probabilistic Engineering Mechanics*, 15:1–28.

[72] Spanos, P. and Payne, M. (1992). Advances in dynamic bottomhole assembly modeling and dynamic response determination. *SPE/IADC drilling conference*.

[73] Spanos, P. D., Chevallier, A. M., and Politis, N. P. (2002). Nonlinear Stochastic Drill-String. 124(October).

[74] Stroud, D. and Lines, L. (2011). Analytical and Experimental Backward Whirl Simulations for Rotary Steerable Bottom Hole Assemblies. *SPE/IADC*, pages 1–19.

[75] Tucker, R. W. and Wang, C. (1997). The Excitation and Control of Torsional Slip-Stick In the Presence of Axial-Vibrations. pages 1–5.

[76] Tucker, R. W. and Wang, C. H.-T. (2003). Torsional Vibration Control and Cosserat Dynamics of a Drill-Rig Assembly. *Meccanica*, 38(1):145–161.

[77] Tucker, W. and Wang, C. (1999a). An Integrated Model for Drill-String Dynamics. *Journal of Sound and Vibration*, 224(1):123–165.

[78] Tucker, W. and Wang, C. (1999b). On the effective control of torsional vibrations in drilling systems. *Journal of Sound and Vibration*, 224(1):101 – 122.

[79] Vijayan, K., Vlajic, N., and Friswell, M. I. (2017). Drillstring-borehole interaction: backward whirl instabilities and axial loading. *Meccanica*, 52(11-12):2945–2957.

[80] Volpi, L., Lobo, D. d. M., and Ritto, T. (2019). the Effects of Lateral-Torsional Coupling in Drill-String Dynamics. In *25th ABCM International Congress of Mechanical Engineering*, Uberlandia. ABCM.

[81] Volpi, L. P., Lobo, D. M., and Ritto, T. G. (2020). Coupled Lateral-Torsional Drill-String With Uncertainties. In *5th International Symposium on Unvertainty Quantification and Stochastic Modelling (Uncertainties 2020)*, St-Etienne Rouvray. Springer.

[82] Wagner, N. and Adhikari, S. (2003). Symmetric state-space method for a class of nonviscously damped systems. *AIAA Journal*, 41(5):951–956.

[83] Wiercigroch, M. (2000). Modelling of dynamical systems with motion dependent discontinuities. *Chaos, Solitons and Fractals*, 11(15):2429–2442.

[84] Wilson, E. L. (2004). Static and dynamic analysis of structures. *A Physical Approach with Emphasis on Earthquake Enginering, Fourth Edition, CSI.*

[85] Wriggers, P. (2008). *Nonlinear finite element methods.* Springer Science & Business Media.

[86] Yigit, A.S. e Christoforou, A. (1998). Coupled torsional and bending vibrations of drillstrings subject to impact with friction. *Journal of Sound and Vibration*, 215(1):167–181.

[87] Yigit, AS e Christoforou, A. (2000). Coupled torsional and bending vibrations of actively controlled drillstrings. *Journal of sound and vibration*, 234(1):67–83.

[88] Zamanian, M., Khadem, S. E., and Ghazavi, M. R. (2007). Stick-slip oscillations of drag bits by considering damping of drilling mud and active damping system. *Journal of Petroleum Science and Engineering*, 59(3-4):289–299.

[89] Zorzi, E. and Nelson, H. (1980). The dynamics of rotor-bearing systems with axial torque—a finite element approach.

Appendix A

Axial force

The axial force is considered linear within a section of the drill-string ($f_a(x) = \alpha x + \beta$). As the section changes, the values of α and β are updated. In Fig. A.1 a schematic of a drill-string with four sections is presented. When $x = 0$, $f_a(0) = f_h$, where $f_h = (\sum_{k=1}^{s} \rho A_k L_k) - W_{ob}$, where s is the total number of sections, L_k and A_k are the k^{th} section's length and area respectively.

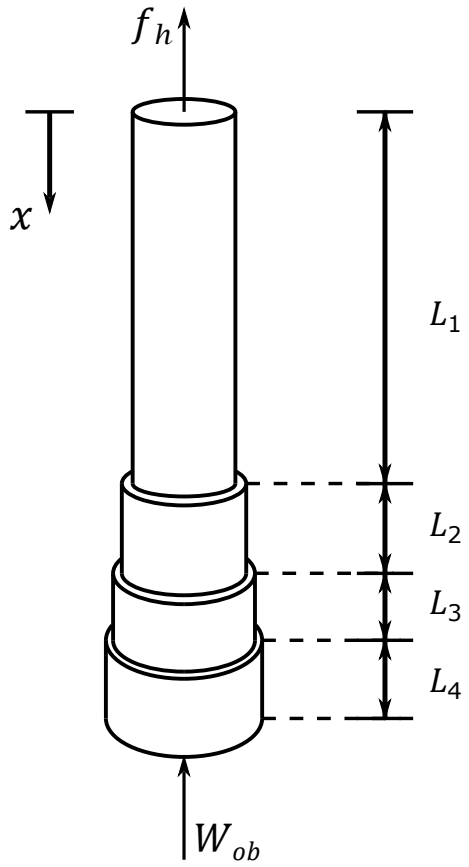

Figure A.1: Sketch of the drill-string's sections.

In an arbitrary cross-section the axial force is modeled as $f_a(x) = f_w(x) - W_{ob}$, where $f_L(x)$ os the sustained weight in a depth of value x. The weight sustained in

the an arbitrary depth in the k^{th} section is:

$$f_{w_k}(x) = \rho A_k \left[\left(\sum_{l=1}^{k} L_k \right) - x \right] + \sum_{p=k+1}^{s} \rho A_p L_p, \tag{A.1}$$

where $\rho A_k \left[\left(\sum_{l=1}^{k} L_k \right) - x \right]$ is the weight of the remaining section in a depth of x and $\sum_{p=k+1}^{s} \rho A_p L_p$ the weight of the sections that subsequent sections. Hence, the axial force in the k^{th} section is:

$$f_{a_k}(x) = \rho A_k \left[\left(\sum_{l=1}^{k} L_k \right) - x \right] + \left(\sum_{p=k+1}^{s} \rho A_p L_p \right) - W_{ob}. \tag{A.2}$$

In Fig. A.2, a sample distribution used in the model is depicted. It considers the geometry presented in Tab.5.1 and that $W_{ob} = 220$kN. In this figure, the values of the ordinate axis are inverted to maintain the direction's agreement with the referential presented in Fig. A.1. Each section is divided by horizontal traced lines and the vertical traced line separates the sections under tension from those under compression. It can be observed that the whole extension of the drill-pipes (the first section) is under tension – which leads to an increase in the lateral stiffness. This behavior changes in the last BHA sections.

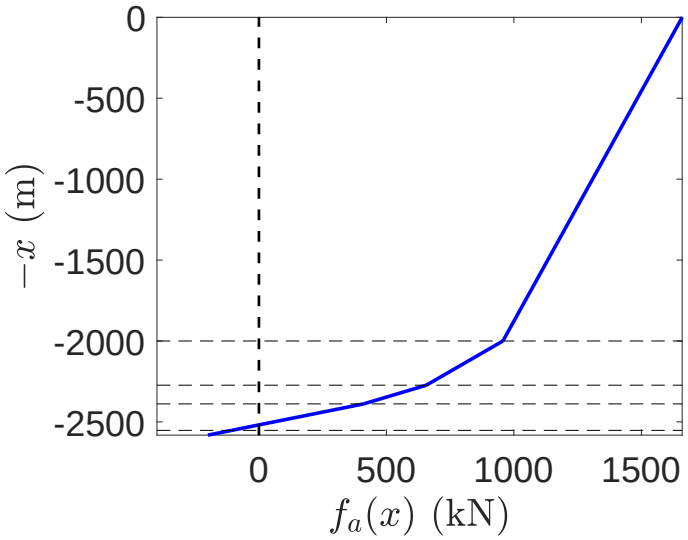

Figure A.2: Sample axial force distribution with $W_{ob} = 220$ kN.

Appendix B

Shape functions

The shape functions for lateral degrees of freedom are formed by Hermitian polynomials, from N_1 to N_4. As for torsional degrees of freedom, a linear polynomial was used (N_5 and N_6):

$$N_1 = 1 - 3\eta^2 + 2\eta^3 \tag{B.1}$$

$$N_2 = L_e(\eta - 2\eta^2 + \eta^3) \tag{B.2}$$

$$N_3 = 3\eta^2 - 2\eta^3 \tag{B.3}$$

$$N_4 = L_e(-2\eta^2 + \eta^3) \tag{B.4}$$

$$N_5 = 1 - \eta \tag{B.5}$$

$$N_6 = \eta \tag{B.6}$$

where L_e is the element's length and $\eta = \frac{x - L_i}{L_e}$ is a normalization. Once again, L_i is the depth of the first node of the i_{th} element:

$$L_i = \sum_{n=1}^{i} L_{e_i}. \tag{B.7}$$

Finally, the shape functions are defined as:

$$\boldsymbol{N}_v = \begin{Bmatrix} N_1 & 0 & 0 & N_2 & 0 & N_3 & 0 & 0 & N_4 & 0 \end{Bmatrix}, \tag{B.8}$$

$$\boldsymbol{N}_w = \begin{Bmatrix} 0 & N_1 & 0 & 0 & -N_2 & 0 & N_3 & 0 & 0 & -N_4 \end{Bmatrix}, \tag{B.9}$$

$$\boldsymbol{N}_\phi = \begin{Bmatrix} 0 & 0 & N_5 & 0 & 0 & 0 & 0 & N_6 & 0 & 0 \end{Bmatrix}, \tag{B.10}$$

$$\boldsymbol{N}_{\varphi_y} = \frac{d\boldsymbol{N_w}}{dx} = \frac{d\boldsymbol{N_w}}{d\eta}\frac{d\eta}{dx} = \frac{1}{L_2}\frac{d\boldsymbol{N_w}}{d\eta} \tag{B.11}$$

and:

$$\boldsymbol{N}_{\varphi_z} = \frac{1}{L_e}\frac{d\boldsymbol{N_v}}{d\eta}. \tag{B.12}$$

It should be noticed that the Eqs. 3.38 to 3.44 are written as a function of x for continuity purposes and, during calculations, the integrals are normalized accordingly.

Appendix C

Damping models

In the literature, there is a variety of approaches for damping models. This Appendix presents some of these modelling techniques with examples. These examples consider linear lateral vibrations restricted to one of the planes under harmonic excitations. In other words, the drill-string is considered rigid to torsion and *a priori* no gyroscopic effects are taken into account. Even though the cases treated here consider a multiple degree of freedom system, they can be applied to single degree of freedom systems.

C.0.1 Viscously damped systems

Viscously damped systems are usually written as:

$$\boldsymbol{M}\ddot{\boldsymbol{q}} + \boldsymbol{C}\dot{\boldsymbol{q}} + \boldsymbol{K}\boldsymbol{q} = \boldsymbol{F}, \tag{C.1}$$

where $\boldsymbol{M}$, $\boldsymbol{C}$ and $\boldsymbol{K}$ are the inertia, damping and stiffness matrices respectively. Vector $\boldsymbol{F}$ is a generalized force vector and $\boldsymbol{q}$ a generalized coordinate vector. Considering properly normalized modes of the undamped system as $\boldsymbol{\Phi}$, in the modal base, the system becomes:

$$\ddot{\boldsymbol{\eta}} + \mathcal{C}\dot{\boldsymbol{\eta}} + \boldsymbol{\Lambda}\boldsymbol{\eta} = \boldsymbol{\mathcal{F}}, \tag{C.2}$$

where $\boldsymbol{\eta}$ is the modal coordinates, $\mathcal{C}$ the modal damping, $\boldsymbol{\Lambda}$ a diagonal matrix containing the square of the eigengrequencies and $\boldsymbol{\mathcal{F}}$ a force vector in the modal base. Until now, the matrix $\mathcal{C}$ is not necessarily diagonal. In other words, there is no assumption regarding classical normal modes. In order to guarantee this condition [12] proved that it is necessary to have:

$$\boldsymbol{K}\boldsymbol{M}^{-1}\boldsymbol{C} = \boldsymbol{C}\boldsymbol{M}^{-1}\boldsymbol{K}, \tag{C.3}$$

In [1], a modified version is stated, where, if $\boldsymbol{M}$, $\boldsymbol{C}$ and $\boldsymbol{K}$ and there exists a base transformation matrix where $\boldsymbol{M}$, $\boldsymbol{C}$ and $\boldsymbol{K}$ are real diagonal matrices, then:

$$\boldsymbol{K}\boldsymbol{M}^{-1}\boldsymbol{C} = \boldsymbol{C}\boldsymbol{M}^{-1}\boldsymbol{K}, \quad \boldsymbol{M}\boldsymbol{K}^{-1}\boldsymbol{C} = \boldsymbol{C}\boldsymbol{K}^{-1}\boldsymbol{M}, \quad \boldsymbol{M}\boldsymbol{C}^{-1}\boldsymbol{K} = \boldsymbol{K}\boldsymbol{C}^{-1}\boldsymbol{M}. \tag{C.4}$$

Previously, [12] proposed a sufficient condition that if:

$$\boldsymbol{M}^{-1}\boldsymbol{C} = \sum_{j=0}^{N-1} a_j (\boldsymbol{M}^{-1}\boldsymbol{K})^j, \tag{C.5}$$

then classical normal modes would exist. It is easy to see that, if $N = 2$, this equation becomes the Rayleigh damping:

$$\boldsymbol{M}^{-1}\boldsymbol{C} = a_1\mathbb{I} + a_2\boldsymbol{M}^{-1}\boldsymbol{K} \leftrightarrow \boldsymbol{C} = a_1\boldsymbol{M} + a_2\boldsymbol{K}, \tag{C.6}$$

and hence, it can be considered a generalization of the Rayleigh damping.

In [1] is proposed that, if the system is positive definite, the damping matrix can be written in the form of:

$$\boldsymbol{C} = \boldsymbol{M} f_1(\boldsymbol{M}^{-1}\boldsymbol{K}, \boldsymbol{K}^{-1}\boldsymbol{M}) + \boldsymbol{K} f_2(\boldsymbol{M}^{-1}\boldsymbol{K}, \boldsymbol{K}^{-1}\boldsymbol{M}), \tag{C.7}$$

where f_1 and f_2 are known functions. If f_1 and f_2 can be written in terms of Taylor series, it falls under the generalized Rayleigh damping case. However, rewriting in a series of polynomials might lead to truncation errors and even numerical errors, thus, this format might be convenient depending on the functions f_1 and f_2. Also in [1], the author provides a step-by-step approach to this generalized damping given a known frequency dependent damping ratio function $\xi(\omega)$. For example:

$$\xi(\omega) = \frac{1}{2}\left(\frac{\beta_1}{\omega} + \beta_2\sqrt{\omega}\right), \tag{C.8}$$

the set of operations are conducted: $2\omega\xi$ is substituted by $\boldsymbol{M}^{-1}\boldsymbol{C}$, ω by $\sqrt{\boldsymbol{M}^{-1}\boldsymbol{K}}$ and any constant a by $a\mathbb{I}$. Hence, Eq. C.8 is rewritten as:

$$2\omega\xi = \beta_1 + \beta_2\omega^{\frac{3}{2}} \tag{C.9}$$

and, in the sequence:

$$\boldsymbol{M}^{-1}\boldsymbol{C} = \beta_1\mathbb{I} + \beta_2\sqrt{(\boldsymbol{M}^{-1}\boldsymbol{K})^{\frac{3}{2}}}, \tag{C.10}$$

and finally as:

$$\boldsymbol{C} = \beta_1\boldsymbol{M} + \beta_2\boldsymbol{M}(\boldsymbol{M}^{-1}\boldsymbol{K})^{\frac{3}{4}}. \tag{C.11}$$

When returning to the modal base in Eq. C.2, the damping matrix recently calculated $\mathcal{C}$ will be a diagonal matrix where its values follow the relation of the damping ratio function used.

To obtain frequency domain response, proportional damping models are somewhat convenient. The system in the modal base is uncoupled, and thus, can be expressed as:

$$\ddot{\eta}_i + 2\xi_i\omega_{n_i}\dot{\eta}_i + \omega_{n_i}^2\eta_i = \mathcal{F}_i. \tag{C.12}$$

Applying the Fourier transform:

$$(-\Omega^2 + 2\xi_i\omega_{n_i}\Omega j + \omega_{n_i}^2)\tilde{\eta}_i(\Omega) = \tilde{\mathcal{F}}_i(\Omega) \tag{C.13}$$

or

$$\tilde{\eta}_i(\Omega) = \frac{\tilde{\mathcal{F}}_i(\Omega)}{-\Omega^2 + 2\xi_i\omega_{n_i}\Omega j + \omega_{n_i}^2} \tag{C.14}$$

back in the original base:

$$\Phi^{-1}\tilde{\boldsymbol{q}}(\Omega) = \text{diag}\left(\frac{1}{-\Omega^2 + 2\xi_i\omega_{n_i}\Omega j + \omega_{n_i}^2}\right)\Phi^T\tilde{\boldsymbol{F}}_i(\Omega) \tag{C.15}$$

and finally:

$$\tilde{\boldsymbol{q}}(\Omega) = \Phi\ \text{diag}\left(\frac{1}{-\Omega^2 + 2\xi_i\omega_{n_i}\Omega j + \omega_{n_i}^2}\right)\Phi^T\tilde{\boldsymbol{F}}_i(\Omega), \tag{C.16}$$

where $\text{diag}(h_i(\Omega))$ indicates a diagonal matrix containing in the i^{th} column/line and is $h_i(\Omega)$ the transfer function.

C.0.2 Non-viscous damped systems

In contrast with the viscous damping – that depend exclusively on the instantaneous speed – non-viscous damping en-globes a broad area of damping strategies, usually adopted to capture the hysteretic behavior of viscoelasticity. Here a set of these models are explored. They are often referred as hysteretic, viscoelastic or, more generally, as non-viscous damping.

One particular approach is to consider a 'complex stiffness' term in the equations [24]:

$$\boldsymbol{M}\ddot{\boldsymbol{q}} + \boldsymbol{C}\dot{\boldsymbol{q}} + (\boldsymbol{K} + j\boldsymbol{K}_D)\boldsymbol{q} = \boldsymbol{F}. \tag{C.17}$$

If $\boldsymbol{K}_D$ and $\boldsymbol{C}$ follows a proportional damping relation, it is diagonal. In the frequency domain, this methodology is straightforward, as another term is included in the result:

$$\tilde{\boldsymbol{q}}(\Omega) = \Phi\ \text{diag}\left(\frac{1}{-\Omega^2 + 2\xi_i\omega_{n_i}\Omega j + \kappa_i j + \omega_{n_i}^2}\right)\Phi^T\tilde{\boldsymbol{F}}_i(\Omega). \tag{C.18}$$

This methodology, however, might not be as simple in the time domain. In [24], a proportional equivalent damping is proposed for small values of K_D. This approach considers the hysteretic damping in the modal base: $\boldsymbol{C}_{eq} = (\Lambda^{-1/2})(\Phi^T \boldsymbol{K}_D \Phi)$. Once again, while its application is direct, it is only valid for small hysteretic damping.

Maybe the most generic form of representation for a non-viscous damping is in the form of a convolution integral of kernels:

$$\boldsymbol{M}\ddot{\boldsymbol{q}} + \int_{-\infty}^{\infty} \boldsymbol{\mathcal{G}}(t-\tau)\dot{\boldsymbol{q}}(\tau)d\Delta\tau + \boldsymbol{K}\boldsymbol{q} = \boldsymbol{f}, \tag{C.19}$$

where $\boldsymbol{\mathcal{G}}(t-\tau)$ is a matrix containing kernel functions. These kernel functions are used to account for a time history in the damping and can be modeled by different procedures. In the particular case of $\boldsymbol{\mathcal{G}}(t-\tau) = \boldsymbol{C}\delta_d(t-\tau)$, where δ_d is the Dirac delta, only the instantaneous speed is considered, falling in the viscous damping category. As presented in [1], the conditions of existence of classical normal modes are similar to the viscous case:

$$\boldsymbol{K}\boldsymbol{M}^{-1}\boldsymbol{\mathcal{G}}(\boldsymbol{t}-\boldsymbol{\tau}) = \boldsymbol{\mathcal{G}}(\boldsymbol{t}-\boldsymbol{\tau})\boldsymbol{M}^{-1}\boldsymbol{K}, \quad \boldsymbol{M}\boldsymbol{K}^{-1}\boldsymbol{\mathcal{G}}(\boldsymbol{t}-\boldsymbol{\tau}) = \boldsymbol{\mathcal{G}}(\boldsymbol{t}-\boldsymbol{\tau})\boldsymbol{K}^{-1}\boldsymbol{M},$$

$$\boldsymbol{M}\boldsymbol{\mathcal{G}}(\boldsymbol{t}-\boldsymbol{\tau})^{-1}\boldsymbol{K} = \boldsymbol{K}\boldsymbol{\mathcal{G}}(\boldsymbol{t}-\boldsymbol{\tau})^{-1}\boldsymbol{M}. \tag{C.20}$$

A important characteristic of the kernel function matrix, is that it must provide a positive rate of energy dissipation [82]. A common approach is to use it as a function of a damping matrix:

$$\boldsymbol{\mathcal{G}}(t) = \sum_{k}^{n} \boldsymbol{C}_k f_k(t). \tag{C.21}$$

In [82], the authors proposed a state-space formulation for exponentially damped systems for time-domain integration. In this particular case, $\boldsymbol{\mathcal{G}}(t) = \sum_k^n p_k \boldsymbol{C}_k e^{p_k t}$. To exemplify the methodology, a simple case where $n = 1$ is used:

$$\boldsymbol{\mathcal{G}}(t) = p\boldsymbol{C}e^{pt}, \tag{C.22}$$

where the constant damping matrix $\boldsymbol{C}$ is known and p is constant. The system is then:

$$\boldsymbol{M}\ddot{\boldsymbol{q}} + \boldsymbol{C}\int_0^t e^{p(t-\tau)}\dot{\boldsymbol{q}}(\tau)d\Delta\tau + \boldsymbol{K}\boldsymbol{q} = \boldsymbol{f}. \tag{C.23}$$

A new variable is introduced in the system:

$$\boldsymbol{q}_d = \int_0^t pe^{p(t-\tau)}\dot{\boldsymbol{q}}(\tau)d\Delta\tau \tag{C.24}$$

and its derivative in time:

$$\dot{\boldsymbol{q}}_d = \int_0^t -p^2 e^{p(t-\tau)} \dot{\boldsymbol{q}}(\tau) d\Delta\tau + p\dot{\boldsymbol{q}} = -p\boldsymbol{q}_d + p\dot{\boldsymbol{q}}. \tag{C.25}$$

The original system is rewritten in the form of:

$$\boldsymbol{M}\ddot{\boldsymbol{q}} + \boldsymbol{C}\boldsymbol{q}_d + \boldsymbol{K}\boldsymbol{q} = \boldsymbol{f} \tag{C.26}$$

and then as:

$$\boldsymbol{M}\ddot{\boldsymbol{q}} + (\boldsymbol{C}\dot{\boldsymbol{q}} - \frac{1}{p}\boldsymbol{C}\dot{\boldsymbol{q}}_d) + \boldsymbol{K}\boldsymbol{q} = \boldsymbol{f}, \tag{C.27}$$

which can be rewritten as:

$$\begin{bmatrix} \boldsymbol{C} & \boldsymbol{M} & -\boldsymbol{C}/p \\ \boldsymbol{M} & \boldsymbol{O} & \boldsymbol{O} \\ -\boldsymbol{C}/p & \boldsymbol{O} & \boldsymbol{C}/p^2 \end{bmatrix} \begin{Bmatrix} \dot{\boldsymbol{q}} \\ \ddot{\boldsymbol{q}} \\ \dot{\boldsymbol{q}}_d \end{Bmatrix} + \begin{bmatrix} \boldsymbol{K} & \boldsymbol{O} & \boldsymbol{O} \\ \boldsymbol{O} & \boldsymbol{M} & \boldsymbol{O} \\ \boldsymbol{O} & \boldsymbol{O} & -\boldsymbol{C}/p \end{bmatrix} \begin{Bmatrix} \boldsymbol{q} \\ \dot{\boldsymbol{q}} \\ \boldsymbol{q}_d \end{Bmatrix} = \begin{Bmatrix} \boldsymbol{f} \\ \boldsymbol{0} \\ \boldsymbol{0} \end{Bmatrix}, \tag{C.28}$$

where $\boldsymbol{O}$ and $\boldsymbol{0}$ are a zero matrix and vector, respectively. The last line of the matrix comes from the relation established in Eq. C.25. In this formulation, time-domain results can be obtained from a symmetric state-space formulation. In this format, it can also be seen that if p is of high magnitude, then the system of equations falls in a viscous damping formulation.

In summary, it is easy to see how the generic damping approach can cover a broad area of damping models, including the viscous damping.

Appendix D

Modal reduction

In this appendix, the modal reduction is discussed. As mentioned in Section 3.3.4, a frequency range was chosen and, in the sequence, the modes used in the reduction are selected in accordance. In order to compare the final result, the modal reduction was applied to the simplified model and compared with the complete model, both in accordance with the defined in Section 5.5.2. The time domain analysis presented uses the Rayleigh proportional damping model presented in Section 3.4.1.

In Fig. D.1, the radial displacement and rotating speed development through time are presented for the complete model, with 2000 degrees of freedom, and the reduced order with $W_{ob} = 100$ kN and $\Omega = 1.33$ Hz. For the reduced order, the first 500 modes of the structure were used. Those modes en-globe torsional, lateral and flexural modes in all directions in space, thus, symmetric modes are taken into account. It is also important to notice that the rigid body mode in torsional direction is present in the reduction. It can be noticed that, in this case, the modal reduction provides coherent results when compared with the complete model.

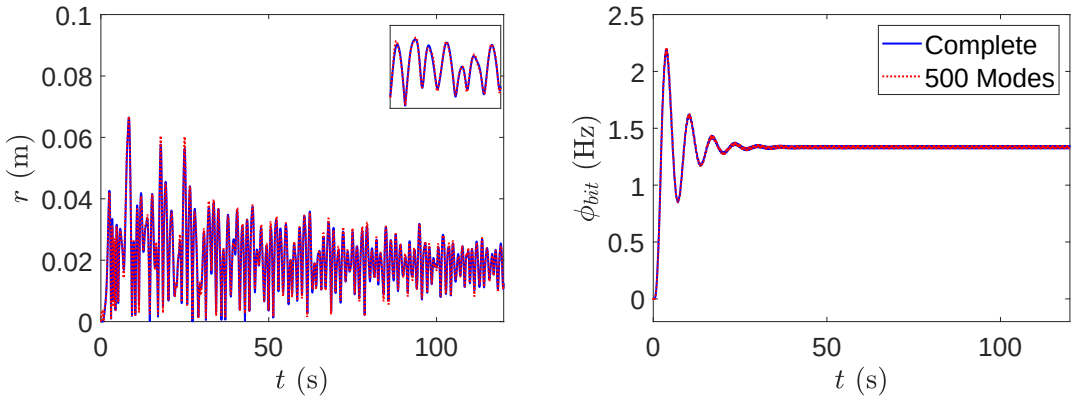

(a) (b)

Figure D.1: Numerical simulations for the complete and reduced models for $\Omega = 1.33$ Hz (80 rpm) and $W_{ob} = 100$ kN. In the zoomed region defined from $t = [50, 60]$ s.

In Fig. D.2, another simulation is shown. This time, the $W_{ob} = 220$ kN and

$\Omega = 0.67$ Hz. It can be seen that while some difference can be seem in the dynamics, the overall behaviour ir similar. Yet, after some time, a small phase angle can be seem in Fig. D.3b. Once again, although this might imply in some information loss, a qualitatively analysis is still accurate.

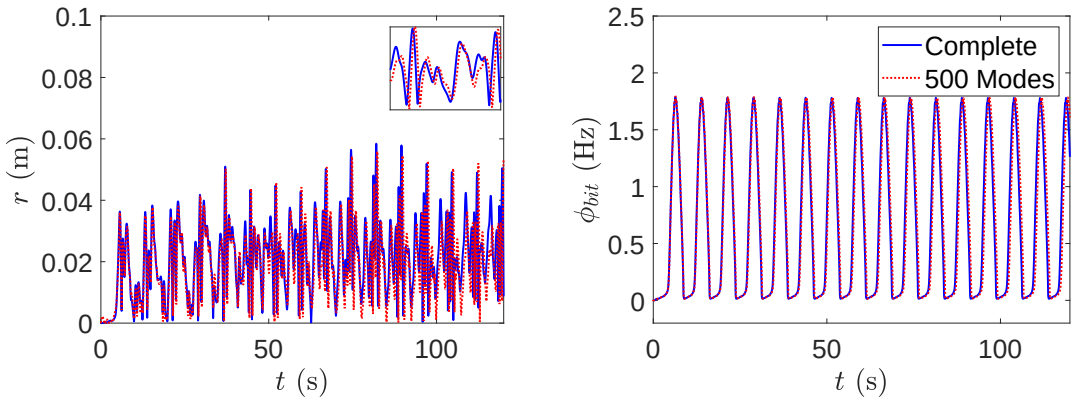

(a) (b)

Figure D.2: Numerical simulations for the complete and reduced models for $\Omega = 0.67$ Hz (40 rpm) and $W_{ob} = 220$ kN. In it, the complete model and with a modal reduction with the first 500 modes.

Finally, Fig. D.3 depicts the simulation with $W_{ob} = 220$ kN and $\Omega = 1$ Hz (60 rpm). As seen before in 5.5.2, the dynamics diverge after the impact moment. However, it can be seen that, although the quantitative analyses are different, both results are qualitatively equivalent. In other words, The reduced order model successfully capture every nonlinear phenomena expected.

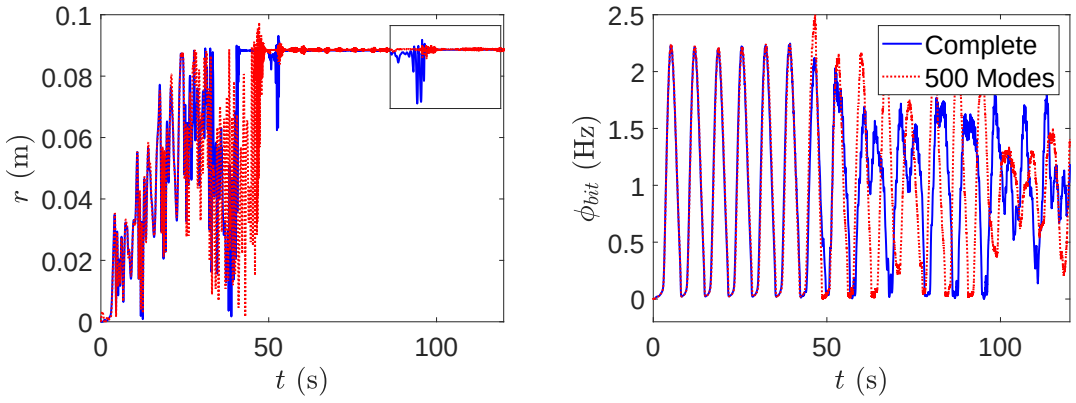

(a) (b)

Figure D.3: Numerical simulations for the complete and reduced models for $\Omega = 1$ Hz (60 rpm) and $W_{ob} = 220$ kN. In it, the complete model and with a modal reduction with the first 500 modes.

While the complete model needed a time-step of $\Delta t = 2.5 \cdot 10^{-4}$ to achieve convergence, the reduced order model with the first five hundred modes converged

with a time-step of $\Delta t = 1 \cdot 10^{-2}$. Whereas some difference is seen in a quantitative evaluation, the overall occurrence of phenomena is well preserved. In this case, a trade-off between accuracy and processing time is done.

Appendix E

Lumped parameter model

The work presented in this dissertation focus solely on a continuous model, discretized by the lumped parameter model. However, the research started with lumped parameter models, which gave major insights in the dynamics. Briefly, the lumped parameter model followed a standard formulations found in the literature [5, 13, 31, 74, 87]:

$$
\begin{aligned}
I_m\ddot{\phi} + c_t(\phi - \Omega) + k_t(\phi - \Omega t) = T_{bit} + T_{lat},\\
(m + m_f)(\ddot{r} - \dot{\theta}^2 r) + c_h(r, \dot{r}, \dot{\theta})\dot{r} + k(T_{bit})r =\\
(m + m_f)[e\dot{\phi}^2 \cos(\phi - \theta) + e\ddot{\phi}\sin(\phi - \theta)] - F_n,\\
(m + m_f)(\ddot{\theta} r + 2\dot{r}\dot{\theta}) + c_h(r, \dot{r}, \dot{\theta})r\dot{\theta} =\\
(m + m_f)[e\dot{\phi}^2 \sin(\phi - \theta) - e\ddot{\phi}\cos(\phi - \theta)] - F_{fat},
\end{aligned}
\tag{E.1}
$$

where there are three degrees of freedom, one regarding drill-pipes torsion (ϕ) and the other two associated with the radial displacement and the whirl angle of a BHA section between stabilizers (r and θ, respectively). In the formulation above, I_m is an equivalent inertia, c_t the torsional damping, k_t the torsional stiffness, T_{bit} the bi-rock interaction torque, T_{lat} the torques due to lateral dynamics. m and m_f are the BHA section's mass and fluid added mass. $c_h(r, \dot{r}, \dot{\theta})$ is a fluid drag damping coefficient, that is proportional to the BHA cross-section's displacement speed: $c_h(r, \dot{r}, \dot{\theta}) = c_l\sqrt{\dot{r}^2 + r^2\dot{\theta}^2}$. Constant e is the eccentricity, F_n and F_{fat} are the elastic force and friction force during impact.

Several works were formerly conducted with this model. Different coupling configurations were analyzed in [80], where it was observed that lateral vibrations could disrupt severe torsional vibrations and that critical lateral vibrations were closely related to torsional vibrations. In the sequence, in [81], the borehole wall friction was modeled as a random variable. With this stochastic model, it was observed that

the incidence of impact and backward whirl is greatly impacted by the borehole wall friction. Other works were conducted regarding random variables: borehole wall, unbalance and bit-rock interaction constants.